

Department of Physics and Astronomy

Heidelberg University

Master thesis

in Physics

submitted by

Matthieu Kecke

born in Magdeburg

September 2014

Time-integrated measurement

of CP violation using

$B_s^0 \rightarrow \phi\phi$ decays

with the LHCb experiment

This Master thesis has been carried out by Matthieu Kecke

at the

Physikalisches Institut Heidelberg

under the supervision of

Prof. Dr. Ulrich Uwer

Abstract

This thesis presents the time-integrated measurement of CP violation in the decay $B_s^0 \rightarrow \phi\phi$. The precise determination of CP-violating triple product asymmetries A_U and A_V tests the existence of new heavy degrees of freedom contributing to the quantum corrections in $B_s^0 - \bar{B}_s^0$ mixing and the loop-suppressed decay $B_s^0 \rightarrow \phi\phi$. They are determined using a simultaneous maximum likelihood fit to the mass distribution of the different triple product ranges. Detector and event reconstruction efficiencies are treated as systematic uncertainties. The used data sample that has been collected during the full LHCb run I during 2011 and 2012 at a center of mass energy of $\sqrt{s} = 7$ and 8 TeV corresponds to an integrated luminosity of $\mathcal{L} = 3.1 \text{ fb}^{-1}$. Approximately 3900 $B_s^0 \rightarrow \phi\phi$ signal candidates are used to determine the triple product asymmetries. They are found to be

$$A_U = -0.003 \pm 0.017(\text{stat}) \pm 0.006(\text{syst}),$$

$$A_V = -0.017 \pm 0.017(\text{stat}) \pm 0.006(\text{syst}).$$

The results are compatible with the Standard Model prediction of $A_U = A_V = 0$ corresponding to a conservation of the CP symmetry.

Kurzfassung

In dieser Arbeit wird die zeitintegrierte Messung von CP Verletzung im Zerfall $B_s^0 \rightarrow \phi\phi$ vorgestellt. Die präzise Bestimmung der CP-verletzenden Spatproduktasymmetrien A_U und A_V testet die Existenz neuer schwerer Freiheitsgrade, welche zu den Quantenkorrekturen in der Mischung von $B_s^0 - \bar{B}_s^0$ und dem Quantenschleifen-unterdrückten Zerfall $B_s^0 \rightarrow \phi\phi$ beitragen. Zu der Bestimmung wird ein simultaner Maximum-Likelihood-Fit verwendet, welcher die Massenverteilung der verschiedene Spatproduktbereiche parametrisiert. Die Akzeptanzen, welche durch den Detektor und den Prozess der Ereignisrekonstruktion auftreten, werden untersucht und als systematische Unsicherheiten berücksichtigt. Die für die Analyse benutzten Daten wurden während des ersten Laufs des LHCb in den Jahren 2011 und 2012 bei Schwerpunktsenergien von $\sqrt{s} = 7$ und 8 TeV gesammelt und entsprechen einer integrierten Luminosität von $\mathcal{L} = 3.1 \text{ fb}^{-1}$. In der hier präsentierte Messung wurden ca. 3900 $B_s^0 \rightarrow \phi\phi$ Signal-Ereignisse gefunden. Die Spatproduktasymmetrien wurden bestimmt zu

$$A_U = -0.003 \pm 0.017(\text{stat}) \pm 0.006(\text{syst}),$$

$$A_V = -0.017 \pm 0.017(\text{stat}) \pm 0.006(\text{syst}).$$

Die Ergebnisse sind im Einklang mit den Vorhersagen des Standardmodells der Teilchenphysik, welches $A_U = A_V = 0$ erwartet. Dies entspricht CP-Erhaltung.

Contents

1	Introduction	4
2	Theory	6
2.1	The Standard Model of Particle Physics	6
2.2	Introduction to flavor physics	7
2.3	CP violation in the Standard Model	9
2.3.1	CP violation in decay	10
2.3.2	CP violation in mixing	10
2.3.3	CP violation in the interference between mixing and decay	10
2.4	Phenomenology of the $B_s^0 \rightarrow \phi\phi$ decay	11
2.5	Triple product asymmetries	13
3	The LHCb experiment	15
3.1	The Large Hadron Collider	15
3.2	Production of beauty hadrons at the LHC	16
3.3	The LHCb Detector	17
3.3.1	Tracking detectors	18
3.3.2	Particle identification	21
3.3.3	The muon system	23
3.3.4	Event reconstruction	23
3.3.5	The LHCb trigger system	24
4	Analysis strategy	26
5	Selection of $B_s^0 \rightarrow \phi\phi$ candidates	27
5.1	Trigger selection	27
5.2	Pre-Selection of the $B_s^0 \rightarrow \phi\phi$ decay	28
5.3	Multivariate selection	30
5.4	Comparison of simulation and data	34
6	Description of fitting procedure	36
7	Backgrounds from other b-hadron decays	38
7.1	$B^+ \rightarrow \phi K^+$	39
7.2	$B^0/B_s^0 \rightarrow \phi\pi^+\pi^-$	40

7.3	$\Lambda_b^0 \rightarrow \phi K^- p$	40
7.4	$B^0/B_s^0 \rightarrow \phi K^*(892)$	42
7.5	Summary and $B_s^0 \rightarrow \phi\phi$ mass fit	44
8	Determination of decay-time acceptance correction	47
8.1	Selection of $B_s^0 \rightarrow D_s^+ \pi^-$ candidates	48
8.2	Comparison of simulated $B_s^0 \rightarrow D_s^+ \pi^-$ and $B_s^0 \rightarrow \phi\phi$ time acceptance . .	49
8.3	Data driven selection of $B_s^0 \rightarrow D_s^+ \pi^-$ signal candidates	51
8.4	Extraction of the decay-time acceptance correction	53
9	Determination of angular acceptance correction	56
10	Determination of the triple product asymmetries	60
10.1	Validation of the fitting procedure	64
11	Estimation of systematic uncertainties	67
11.1	decay-time acceptance	67
11.2	Angular distribution	70
11.3	Peaking background	70
11.4	Mass model	71
11.5	Summary	72
12	Summary and outlook	75
A	Distributions of the multivariate analysis variables	77
	Acknowledgments	81

Introduction

For almost 40 years the current formulation of the Standard Model of Particle Physics has been enormously successful in describing physics at the quantum scale and predicting particle properties that are observed in various experiments all over the world. However, although successfully describing the electromagnetic, strong and weak force, the Standard Model does not include the theory of general relativity that describes the gravitational interaction and fails to describe high energy scales. It also does not explain the existence of dark-matter (that should exist to explain cosmological and astronomical observations) and the excess of matter with respect to anti-matter in our observable universe.

Various new theories expand the Standard Model in order to accommodate these phenomena. Almost all of these expansions introduce additional particles at higher energy scales. The Large Hadron Collider (LHC) near Geneva, the world's largest particle accelerator, is designed to reach high energy limits that have never been observed before. Standard Model predictions can be precisely tested at these energy scales and the search for physics beyond the standard model, directly connected to the search for unknown particles is ongoing. A different approach to explore physics at the highest scales are amplitudes of rare decays and CP-violating observables, which are very sensitive to new heavy degrees of freedom contributing to quantum loops. They present excellent probes of new physics effects. The LHCb experiment, one of the four experiments at the LHC, is designed to study those effects in decays of b- and c-hadrons.

This thesis presents a time-integrated measurement of CP violation in the $B_s^0 \rightarrow \phi\phi$ decay. The decay is mediated by quantum loop corrections with gluon exchange. Heavy unobserved particles could contribute to the loop. Due to the fact that only virtual particles are exchanged in the loop, the mass scale of these contributions can be much higher than the actual energy scale of the decaying mesons. Additionally, the $B_s^0 - \bar{B}_s^0$ mixing amplitude interferes with the $B_s^0 \rightarrow \phi\phi$ decay. For this thesis, the CP-violating triple product asymmetries A_U and A_V are determined. They were first measured by the CDF Collaboration at the Fermilab Tevatron collider in 2011 [1], using 295 $B_s^0 \rightarrow \phi\phi$ signal events. The presented measurement has used approximately 3900 signal candidates, allowing for a greatly enhanced statistical precision.

This thesis is structured as follows. In Chapter 2, the Standard Model of Particle Physics is introduced and the phenomenology of $B_s^0 \rightarrow \phi\phi$ decays is discussed, with emphasis on the triple product asymmetries. Chapter 3 gives an overview of the LHCb

detector and its components. In Chapter 4, the analysis strategy for the presented measurement is summarized. Chapter 5 deals with the selection of $B_s^0 \rightarrow \phi\phi$ candidates from the complete LHCb data set. Chapter 6 introduces the fit techniques used in this analysis to extract the physical parameters. The physical background among selected events is described in Chapter 7. The detector and reconstruction efficiencies are covered in the next two chapters, where Chapter 8 summarizes the decay time efficiency studies and Chapter 9 discusses the angular acceptance. The extraction of the CP-violating observables is described in Chapter 10 and the systematic uncertainties of the measurement are discussed in Chapter 11. Chapter 12 summarizes the results of the analysis and gives an overview of possible improvements and future measurements.

The results presented in this analysis are documented in the LHCb analysis note [2] and the time-integrated and time-dependent analysis of the channel is combined in the paper [3], which I co-authored. For this paper I contributed the measurement of the triple product asymmetries and provided cross-checks for the determination of the decay time acceptance and backgrounds from other b-hadron decays.

Theory

This chapter presents an overview of the theoretical background that is important for this analysis. First, the Standard Model of particle physics is briefly introduced, followed by a summary of the sources of CP violation within this model. After that, the phenomenology of $B_s^0 \rightarrow \phi\phi$ decays is presented and the search for possible beyond Standard Model effects in this channel is discussed.

2.1. The Standard Model of Particle Physics

The Standard Model of Particle Physics is a theory describing matter and interactions at the level of fundamental particles. All known matter is build up from the twelve spin 1/2 particles called fermions. They are grouped into six quarks and six leptons. The interactions are mediated by bosons which are spin-1 particles. The Standard Model is a relativistic and renormalizable quantum field theory describing three of the four fundamental interactions of nature. It combines the description of strong interactions, the quantum chromodynamics (QCD), with the weak and the electromagnetic forces, which are in turn unified to the electroweak force by Glashow [4], Salam [5] and Weinberg [6]. The particle content of the Standard Model is shown in Figure 2.1.

There are three generations of fermions with the same properties and different masses. The first, second and third quark generations consist of the up-type quarks (up, charm and top) which carry electric charge of $+2/3e$ and the corresponding three down-type quarks (down, strange and bottom) which carry electric charge of $-1/3e$. All quarks also carry color charge (red, green or blue) which enables them to take part in the strong interaction that couples to color. The lepton generations consist of three pairs of leptons with unit charge of $-1e$ (e^- , μ^- and τ^-) together with the corresponding neutral neutrinos (ν_e , ν_μ and ν_τ). Every fermion has an anti-particle with the same mass and opposite charge.

The three forces described by the Standard Model are mediated by bosons. A force acting on a particle is represented by the exchange of such a boson. The strong force couples to color and is mediated by the massless gluon g , carrying itself a color charge. The exchange particle of the electromagnetic force, the photon γ , is also massless and electrically neutral. The massive W^\pm and Z^0 bosons mediate the charged and neutral weak interaction. The scalar (spin 0), electrically-neutral and massive Higgs boson H is a consequence of the Higgs mechanism [8], which generates particle masses through

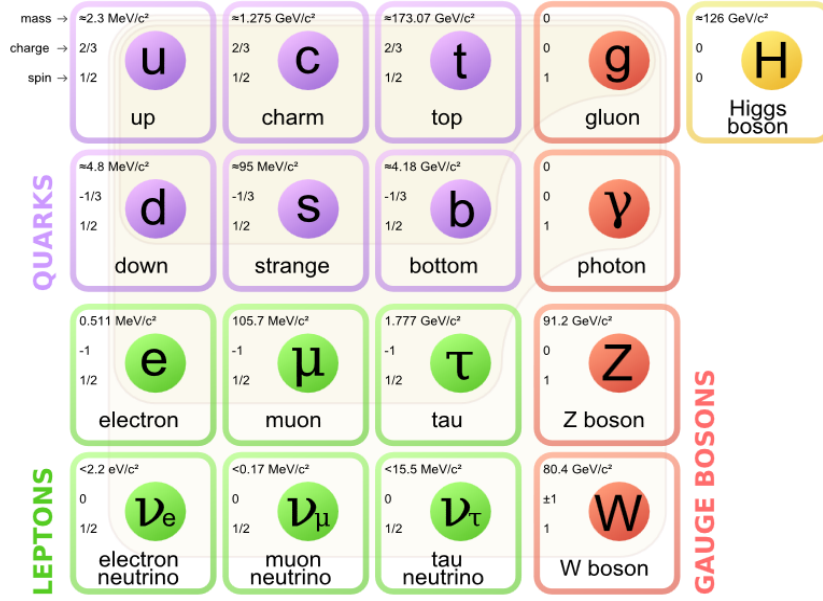


Figure 2.1.: Fundamental particles of the Standard Model. Taken from [7].

its coupling to bosons and fermions. The Higgs boson remained the last undiscovered particle predicted by the Standard Model until in 2012 a Higgs-like particle has been observed by the ATLAS [9] and CMS [10] collaborations.

2.2. Introduction to flavor physics

In the weak interaction, transitions between up- and down-type quarks with the exchange of a W^\pm boson are allowed while flavor-changing neutral currents are forbidden at tree level. The fact that the electroweak quark flavor eigenstates (d', s', b') are not equivalent to the quark mass eigenstates (d, s, b) gives rise to a complex unitary mixing matrix. This matrix is called CKM (Cabibbo-Kobayashi-Maskawa) matrix V_{CKM} [11]:

$$\begin{pmatrix} d' \\ s' \\ b' \end{pmatrix} = \begin{pmatrix} V_{ud} & V_{us} & V_{ub} \\ V_{cd} & V_{cs} & V_{cb} \\ V_{td} & V_{ts} & V_{tb} \end{pmatrix} \cdot \begin{pmatrix} d \\ s \\ b \end{pmatrix}. \quad (2.1)$$

Transitions between quarks are proportional to the corresponding matrix element squared $|V_{ij}|^2$. In general, a complex 3×3 matrix has $[2 \cdot 3 \cdot 3 = 18]$ free parameters. The unitarity relation $V_{CKM} V_{CKM}^\dagger = \mathbb{1}$ reduces the set of free parameters to nine. Five of the remaining parameters can be absorbed into non-observable quark phases. The commonly chosen parameterization of the CKM matrix with the remaining four parameters include

the three Euler angles θ_{12} , θ_{23} and θ_{13} and one complex phase δ :

$$V_{CKM} = \begin{pmatrix} c_{12}c_{13} & s_{12}c_{13} & s_{13}e^{-i\delta} \\ -s_{12}c_{23} - c_{12}s_{23}s_{13}e^{i\delta} & c_{12}c_{23} - s_{12}s_{23}s_{13}e^{i\delta} & s_{23}c_{13} \\ s_{12}c_{23} - c_{12}s_{23}s_{13}e^{i\delta} & -c_{12}s_{23} - s_{12}c_{23}s_{13}e^{i\delta} & c_{23}c_{13} \end{pmatrix}, \quad (2.2)$$

where the coefficients s_{ij} and c_{ij} are abbreviations for $s_{ij} = \sin \theta_{ij}$ and $c_{ij} = \cos \theta_{ij}$, with $i, j \in \{1, 2, 3\}$. In the Standard Model, CP violation is introduced by a non-vanishing value of the phase δ . The diagonal elements of the CKM matrix are experimentally determined to be close to one, while the off-diagonal elements only contribute to a small fraction. Therefore charged current transitions within a quark generation are favored whereas transitions between generations are suppressed. This hierarchy is expressed by the Wolfenstein parameterization of the CKM matrix [12], where $s_{12} = \lambda$, $s_{23} = A\lambda^2$ and $s_{13}e^{-i\delta} = A\lambda^3(\rho + i\eta)$ with the small expansion parameter $\lambda \approx 0.23$:

$$V_{CKM} = \begin{pmatrix} 1 - \frac{\lambda^2}{2} & \lambda & A\lambda^3(\rho - i\eta) \\ -\lambda & 1 - \frac{\lambda^2}{2} & A\lambda^2 \\ A\lambda^3(1 - \rho - i\eta) & -A\lambda^2 & 1 \end{pmatrix} + \mathcal{O}(\lambda^4). \quad (2.3)$$

The nine elements of the CKM matrix are fundamental and no values are predicted by the Standard Model. Therefore, the 4 parameters defining those elements are part of the in total 25 fundamental Standard Model parameters.

For the neutral B_s^0 meson which is a bound flavor eigenstate consisting of an $s-\bar{b}$ quark-antiquark pair, the allowed quark transitions lead to the phenomena of neutral meson mixing. The flavor eigenstates B_s^0 and \bar{B}_s^0 are not equal to the mass eigenstates which are eigenstates of the effective Hamiltonian \mathcal{H} . This allows for oscillations into their respective antiparticle via time evolution of the corresponding Schrödinger equation. The heavy and light mass eigenstates are connected to the flavor eigenstates via:

$$|B_H\rangle = p|B^0\rangle - q|\bar{B}^0\rangle, \quad (2.4)$$

$$|B_L\rangle = p|B^0\rangle + q|\bar{B}^0\rangle, \quad (2.5)$$

with p and q being complex coefficients and $|p|^2 + |q|^2 = 1$. In the Standard Model, the oscillations proceed via box-diagrams as shown in Figure 2.2.

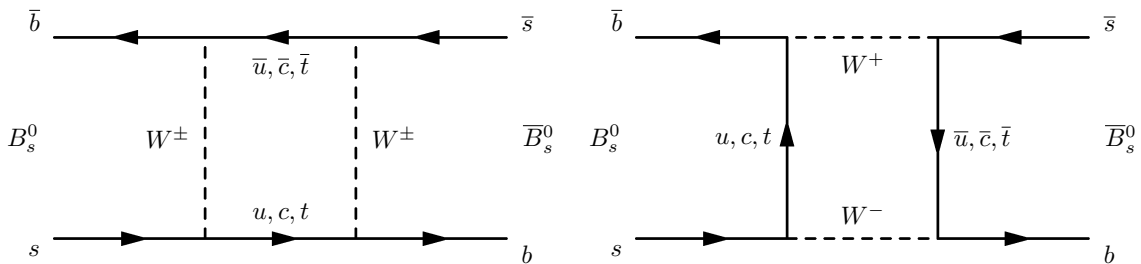


Figure 2.2.: Box diagrams contributing to $B_s^0 - \bar{B}_s^0$ mixing. Taken from [13]

The contributions of intermediate u and c quarks are suppressed by the GIM mechanism [14], which means that the contribution of the t quark is dominant. Thus, the corresponding dominant CKM matrix elements are $|V_{tb}|$ and $|V_{ts}|$. Since $|V_{ts}|$ is an order of magnitude larger than $|V_{td}|$, which would be the corresponding element for the $B^0 - \overline{B}^0$ oscillation, the mixing in the B_s^0 sector is significantly faster than in the B^0 system. This is expressed by the larger mixing frequency $\Delta m_s > \Delta m_d$, which is also the mass difference between the light and heavy eigenstates of the respective mesons.

2.3. CP violation in the Standard Model

The CP transformation is a parity (P) and a charge (C) transformation carried out successively. This is equivalent to replacing a particle with its charge-conjugate, the antiparticle and mirroring the physical system. Considering an eigenstate $|\psi\rangle$ of the P and C operator that describes an arbitrary particle one can express the transformations as

$$P|\psi\rangle = \eta_P|\psi\rangle, \quad (2.6)$$

$$C|\psi\rangle = \eta_C|\psi\rangle, \quad (2.7)$$

$$CP|\psi\rangle = \eta_{CP}|\psi\rangle, \quad (2.8)$$

where η_P , η_C and η_{CP} are the eigenvalues of the P, C and CP operators. Those eigenvalues can take the values ± 1 , where the positive sign is referred to as an *even* and the negative sign is referred to as an *odd* behavior. CP symmetry corresponds to particle-antiparticle symmetry. CP violation causes the particle-antiparticle symmetry to be violated in some physical processes.

One of the necessary conditions for the observed matter excess over anti-matter present in our universe, also called baryon asymmetry, is CP violation [15]. The CKM mechanism described in the previous section is the only source of CP violation within the Standard Model, but the predicted CP violation is several orders of magnitude too small to explain the observed asymmetry between baryonic matter and anti-matter and the resulting baryogenesis in the early universe. It might be described by additional contributions that are not included in the Standard Model. Thus, precise measurements of CP violation in different physical process, e.g. in B mesons systems are crucial. There are three different types of CP violation:

- CP violation in decay
- CP violation in neutral meson mixing
- CP violation in the interference between decay and mixing processes

The first case is referred to as direct CP violation, whereas the other two cases are often called indirect CP violation. The following subsections will give a brief overview over each of the three cases.

2.3.1. CP violation in decay

For direct CP violation, the decay amplitude for a particle X into a final state f , $\mathcal{A}_{X \rightarrow f}$, is not equal to the amplitude of the CP-conjugated process:

$$\left| \frac{\mathcal{A}_{X \rightarrow f}}{\mathcal{A}_{\bar{X} \rightarrow \bar{f}}} \right| \neq 1. \quad (2.9)$$

One way to experimentally access this observable is to measure the decay rate of both processes and to determine the asymmetry

$$A_f = \frac{\Gamma(\bar{X} \rightarrow \bar{f}) - \Gamma(X \rightarrow f)}{\Gamma(X \rightarrow f) + \Gamma(\bar{X} \rightarrow \bar{f})} = \frac{1 - \left| \frac{\mathcal{A}_{X \rightarrow f}}{\mathcal{A}_{\bar{X} \rightarrow \bar{f}}} \right|^2}{1 + \left| \frac{\mathcal{A}_{X \rightarrow f}}{\mathcal{A}_{\bar{X} \rightarrow \bar{f}}} \right|^2}, \quad (2.10)$$

between the yields of the decays $X \rightarrow f$ and $\bar{X} \rightarrow \bar{f}$. $A_f \neq 0$ indicates direct CP violation.

2.3.2. CP violation in mixing

CP violation in neutral meson mixing can be expressed in terms of the coefficients p and q defined in Equation 2.5, which connect the mass and flavor eigenstates of the neutral B meson. CP violation occurs if:

$$\left| \frac{q}{p} \right|^2 \neq 1. \quad (2.11)$$

This corresponds to different transition probabilities $P(B^0 \rightarrow \bar{B}^0)$ and $P(\bar{B}^0 \rightarrow B^0)$. The suitable CP observable in this case is the mixing asymmetry defined as:

$$A_{\text{mixing}} = \frac{\Gamma(\bar{B}^0 \rightarrow B^0 \rightarrow f) - \Gamma(B^0 \rightarrow \bar{B}^0 \rightarrow \bar{f})}{\Gamma(\bar{B}^0 \rightarrow B^0 \rightarrow f) + \Gamma(B^0 \rightarrow \bar{B}^0 \rightarrow \bar{f})}. \quad (2.12)$$

With this definition, $A_{\text{mixing}} = 0$ indicates CP conservation while a non vanishing asymmetry indicates CP violation. Equation 2.12 can also be expressed in terms of the coefficients q and p :

$$A_{\text{mixing}} = \frac{1 - \left| \frac{q}{p} \right|^4}{1 + \left| \frac{q}{p} \right|^4}. \quad (2.13)$$

2.3.3. CP violation in the interference between mixing and decay

The third category is the CP violation in neutral meson decays where the meson can either directly decay into a final CP-eigenstate f_{CP} or can mix first and then decay to the same final state. Figure 2.3 visualizes the two possibilities.

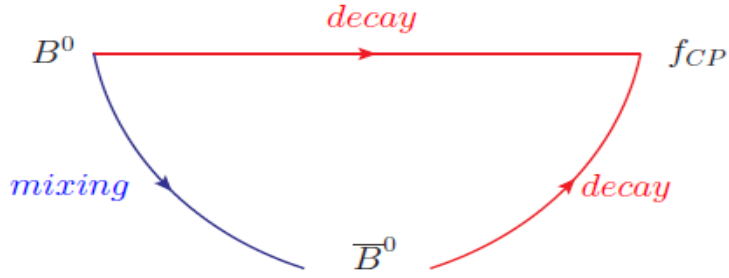


Figure 2.3.: Interference between direct decays of B mesons to f_{CP} and decays of mixed B mesons.

The CP violation for this case can be investigated by comparing the time-dependent decay rates of B^0 and \bar{B}^0 mesons into the same CP final state f_{CP} and calculating the asymmetry:

$$A(t)_{\text{mix\&decay}} = \frac{\Gamma(\bar{B}^0(t) \rightarrow f_{CP}) - \Gamma(B^0(t) \rightarrow f_{CP})}{\Gamma(\bar{B}^0(t) \rightarrow f_{CP}) + \Gamma(B^0(t) \rightarrow f_{CP})}. \quad (2.14)$$

2.4. Phenomenology of the $B_s^0 \rightarrow \phi\phi$ decay

The $B_s^0 \rightarrow \phi\phi$ decay is a flavor-changing neutral current (FCNC) and therefore forbidden at tree level in the Standard Model. It is mediated by a quantum loop involving a $b \rightarrow \bar{s}s$ transition shown in the Feynman graph on the left hand side in Figure 2.4. Decays of this kind are also called electroweak penguins and are interesting to study, because of possible additional contributions entering the quantum loop with new heavy degrees of freedom. To describe the decay topology shown in Figure 2.4(right hand), the helicity basis with the angles θ_1, θ_2 and Φ is defined, where θ_i is the angle between the K_i^+ momentum in the rest frame of the ϕ_i meson with respect to the momentum of the ϕ_i meson in the B_s^0 rest frame. The choice which of the ϕ mesons is assigned the index 1 and 2 is randomized. Φ is the angle between the decay planes spanned by the two $\phi \rightarrow K^+K^-$ decays.

It is important to note that the ϕ meson is a vector particle (V) with spin 1, whereas the B_s^0 is a pseudoscalar (P). Thus, the transition is of the form $P \rightarrow VV$. To conserve the initial spin $J = 0$, there are three different possibilities for the spin configuration of the ϕ mesons relative to each other which are shown in Figure 2.5. Using the relation $\eta_{CP} = (-1)^L$, where L denotes the relative angular momentum, one observes that the transversal configuration corresponds to the $L = 1$ CP-odd polarization A_{\perp} . The other two configurations correspond to the CP-even $L = 0, 2$ polarizations A_0 and A_{\parallel} .

Using the defined helicity angles and the polarization amplitudes, one can express the

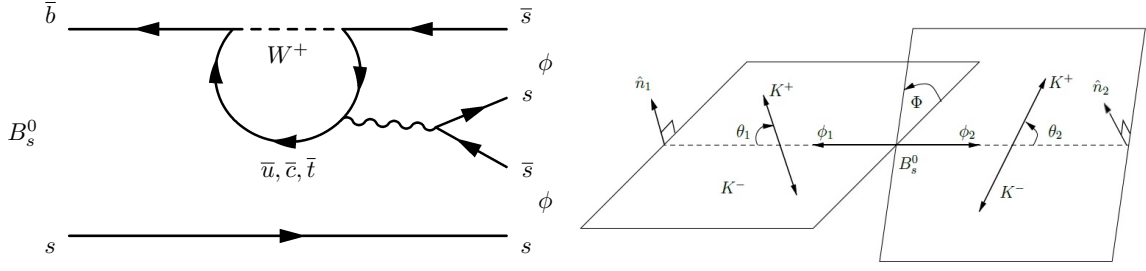


Figure 2.4.: (left) Feynman graph [13] and (right) decay topology [3] of the $B_s^0 \rightarrow \phi\phi$ decay.

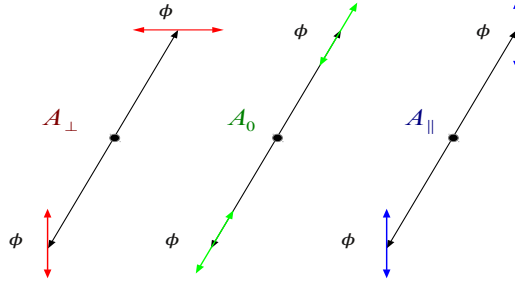


Figure 2.5.: Possible angular polarizations and the corresponding amplitudes for $B_s^0 \rightarrow \phi\phi$ decays.

time-dependent total decay amplitude as [16]:

$$\begin{aligned}
 A(t, \theta_1, \theta_2, \Phi) &= A_0(t) \cos \theta_1 \cos \theta_2 + \frac{A_{\parallel}(t)}{\sqrt{2}} \sin \theta_1 \sin \theta_2 \cos \Phi \\
 &+ i \frac{A_{\perp}(t)}{\sqrt{2}} \sin \theta_1 \sin \theta_2 \sin \Phi.
 \end{aligned}
 \tag{2.15}$$

The differential decay rate is then determined by taking the square of the amplitude:

$$\begin{aligned}
 \frac{d\Gamma}{dt d\theta_1 d\theta_2 d\Phi} &\propto |A(t, \theta_1, \theta_2, \Phi)|^2 \\
 &= |A_0(t)|^2 \cos^2 \theta_1 \cos^2 \theta_2 + \frac{|A_{\parallel}(t)|^2}{2} \sin^2 \theta_1 \sin^2 \theta_2 \cos^2 \Phi \\
 &+ \frac{|A_{\perp}(t)|^2}{2} \sin^2 \theta_1 \sin^2 \theta_2 \sin^2 \Phi + \frac{\text{Re}(A_0(t)A_{\parallel}(t)^*)}{2\sqrt{2}} \sin 2\theta_1 \sin 2\theta_2 \cos \Phi \\
 &- \frac{\text{Im}(A_{\perp}(t)A_0(t)^*)}{2\sqrt{2}} \sin 2\theta_1 \sin 2\theta_2 \sin \Phi - \frac{\text{Im}(A_{\perp}(t)A_{\parallel}(t)^*)}{2} \sin^2 \theta_1 \sin^2 \theta_2 \sin 2\Phi.
 \end{aligned}
 \tag{2.16}$$

2.5. Triple product asymmetries

A triple product is a product of three 3-dimensional vectors. The scalar triple product is defined as the scalar product of one vector with the cross product of the two other vectors [17]. Using arbitrary three dimensional vectors \vec{a} , \vec{b} and \vec{c} , the scalar triple product is of the form

$$\vec{a} \cdot (\vec{b} \times \vec{c}). \quad (2.17)$$

To observe scalar triple products of three momenta in particle physics, a decay with at least four distinguishable particles in the final state is needed. This is due to the fact that the expectation value for a triple product with two identical particles vanishes. As an example, one can consider the decay of a heavy particle B into four final state particles a, b, c and d, where a and b are assumed to be identical and therefore kinematically indistinguishable. One of the four final state momenta is fixed by energy-momentum conservation

$$\mathbf{P}_d = \mathbf{P}_B - \mathbf{P}_a - \mathbf{P}_b - \mathbf{P}_c, \quad (2.18)$$

giving three independent final state momenta in the rest frame of the decaying particle B. The triple product one can form is

$$\epsilon_{ijk} p_a^i p_b^j p_c^k = (\vec{p}_a \times \vec{p}_b) \cdot \vec{p}_c = -(\vec{p}_b \times \vec{p}_a) \cdot \vec{p}_c. \quad (2.19)$$

The antisymmetry of the cross product when exchanging \vec{p}_a and \vec{p}_b causes the expectation value of this triple product to vanish

$$\langle (\vec{p}_a \times \vec{p}_b) \cdot \vec{p}_c \rangle = 0, \quad (2.20)$$

when summing over the indistinguishable momenta of the two identical particles. Scalar triple products of three momenta can be observed in the $B_s^0 \rightarrow \phi\phi$ decay, because the four kaons in the final state are kinematically distinguishable. Considering Figure 2.4, the two unique triple products that can be defined in this channel are [16]

$$\sin \Phi = (\vec{n}_1 \times \vec{n}_2) \cdot \vec{p}_1, \quad (2.21)$$

$$\sin 2\Phi = 2(\vec{n}_1 \cdot \vec{n}_2)(\vec{n}_1 \times \vec{n}_2) \cdot \vec{p}_1, \quad (2.22)$$

where \vec{n}_i is the unit vector perpendicular to the ϕ_i meson decay plane spanned by the related kaons and \vec{p}_1 is the unit vector in the direction of the ϕ_1 meson's momentum.

The triple products are called $U = \sin 2\Phi$ and $V = \pm \sin \Phi$ where the positive sign corresponds to $(\cos\theta_1 \cos\theta_2) > 0$ and the negative sign to $(\cos\theta_1 \cos\theta_2) < 0$. These triple products change sign under time reversal. For any \mathbb{T} -transformation $t \rightarrow -t$, the position of a particle \vec{x} and its three momentum \vec{p} transform like

$$\mathbb{T}\vec{x} = \vec{x}, \quad (2.23)$$

$$\mathbb{T}\vec{p} = \mathbb{T}\left(\gamma m_0 \frac{\partial}{\partial t} \vec{v}\right) = -\left(\gamma m_0 \frac{\partial}{\partial t} \vec{v}\right) = -\vec{p}, \quad (2.24)$$

where m_0 is the invariant mass of the particle. Using Equation 2.24, one can conclude that the triple products U and V transform like

$$\mathbb{T} \sin \Phi = \mathbb{T} \vec{p}_1 \cdot (\mathbb{T} \vec{n}_1 \times \mathbb{T} \vec{n}_2) = -\vec{p}_1 \cdot (\vec{n}_1 \times \vec{n}_2) = -\sin \Phi, \quad (2.25)$$

$$\mathbb{T} \sin 2\Phi = \mathbb{T} \vec{p}_1 \cdot 2(\mathbb{T} \vec{n}_1 \cdot \mathbb{T} \vec{n}_2)(\mathbb{T} \vec{n}_1 \times \mathbb{T} \vec{n}_2) = -\vec{p}_1 \cdot 2(\vec{n}_1 \cdot \vec{n}_2)(\vec{n}_1 \times \vec{n}_2) = -\sin 2\Phi. \quad (2.26)$$

Thus, the triple products U and V exhibit a T-odd behavior.

The asymmetries A_U and A_V are defined as the difference between the decay rate of $B_s^0 \rightarrow \phi\phi$ decays involving positive and negative signs of U or V:

$$A_U = \frac{\Gamma(\sin 2\Phi > 0) - \Gamma(\sin 2\Phi < 0)}{\Gamma(\sin 2\Phi > 0) + \Gamma(\sin 2\Phi < 0)}, \quad (2.27)$$

$$A_V = \frac{\Gamma(\text{sign}(\cos \theta_1 \cos \theta_2) \sin \Phi > 0) - \Gamma(\text{sign}(\cos \theta_1 \cos \theta_2) \sin \Phi < 0)}{\Gamma(\text{sign}(\cos \theta_1 \cos \theta_2) \sin \Phi > 0) + \Gamma(\text{sign}(\cos \theta_1 \cos \theta_2) \sin \Phi < 0)}. \quad (2.28)$$

The triple products U and V correspond to the fifth and sixth term in Equation 2.16 which contribute to a T-odd asymmetry. Non-vanishing asymmetries A_U or A_V indicate T-violation. Assuming CPT-conservation implies that also CP is violated. A_U and A_V may also be expressed in terms of the amplitudes A_0 , A_\perp and A_\parallel by integrating the decay rate defined in Equation 2.16 over θ_1 , θ_2 and t using [16]

$$\int_{-1}^1 \cos^2 \theta d(\cos \theta) = \frac{2}{3}, \quad \int_{-1}^1 \sin^2 \theta d(\cos \theta) = \frac{4}{3}, \quad \int_{-1}^1 \sin 2\theta d(\cos \theta) = 0. \quad (2.29)$$

The resulting integrated decay rate is then

$$\frac{d\Gamma}{d\Phi} = \frac{4}{9} N (|A_0|^2 + 2|A_\perp|^2 \sin^2 \Phi + 2|A_\parallel|^2 \cos^2 \Phi - 2\text{Im}(A_\perp A_\parallel^*) \sin 2\Phi), \quad (2.30)$$

where N is the total number of $B_s^0 \rightarrow \phi\phi$ events. With Equation 2.30 the triple product asymmetry A_U can be rewritten using the defined amplitudes

$$\begin{aligned} A_U &= \frac{\Gamma(\sin 2\Phi > 0) - \Gamma(\sin 2\Phi < 0)}{\Gamma(\sin 2\Phi > 0) + \Gamma(\sin 2\Phi < 0)} \\ &= \frac{[\int_0^{\pi/2} + \int_\pi^{3\pi/2}] (d\Gamma/d\Phi) d\Phi - [\int_{\pi/2}^\pi + \int_{3\pi/2}^{2\pi}] (d\Gamma/d\Phi) d\Phi}{\int_0^{2\pi} (d\Gamma/d\Phi) d\Phi} \\ &= -\frac{4}{\pi} \frac{\text{Im}(A_\perp A_\parallel^*)}{|A_0|^2 + |A_\perp|^2 + |A_\parallel|^2}. \end{aligned} \quad (2.31)$$

Similarly, one can use Equation 2.16 to derive that

$$\begin{aligned} A_V &= \frac{\Gamma(\text{sign}(\cos \theta_1 \cos \theta_2) \sin \Phi > 0) - \Gamma(\text{sign}(\cos \theta_1 \cos \theta_2) \sin \Phi < 0)}{\Gamma(\text{sign}(\cos \theta_1 \cos \theta_2) \sin \Phi > 0) + \Gamma(\text{sign}(\cos \theta_1 \cos \theta_2) \sin \Phi < 0)} \\ &= -\frac{2\sqrt{2}}{\pi} \frac{\text{Im}(A_\perp A_0^*)}{|A_0|^2 + |A_\perp|^2 + |A_\parallel|^2}. \end{aligned} \quad (2.32)$$

A sizable CP-violating triple product asymmetry is expected in the case of weak phases which deviate from Standard Model expectations or a larger than expected B_s^0 mixing frequency [18]. Those would be unambiguous signs for new physic effects. The triple product asymmetries A_U and A_V are determined in this analysis.

The LHCb experiment

This chapter describes the Large Hadron Collider beauty (LHCb) experiment, which is one of the four large experiments located at the Large Hadron Collider (LHC). It is dedicated to perform precision measurements in the flavor sector of the Standard Model. Most prominently, LHCb aims for measurements of CP violation in b - and c -hadron decays [19].

3.1. The Large Hadron Collider

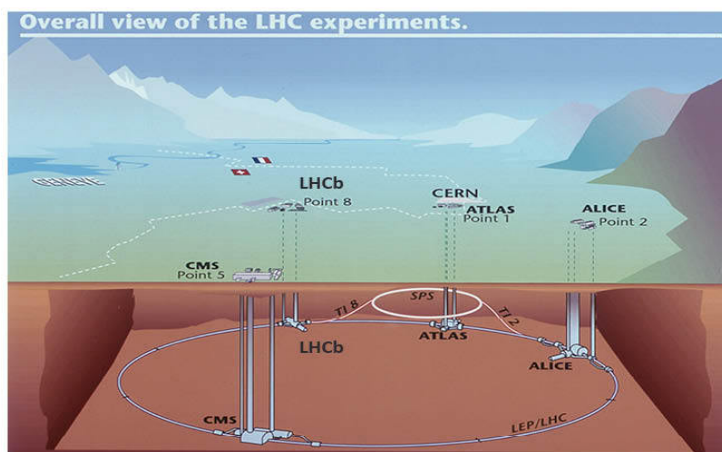


Figure 3.1.: Schematic view of the LHC taken from [20].

The Large Hadron Collider is located at the European Laboratory for Particle Physics CERN in Geneva. It is a proton-proton ring collider with a circumference of approximately 27 km and a designed center of mass energy of up to $\sqrt{s} = 14$ TeV. The LHC is the first machine to reach this energy scale. The four large experiments ATLAS (A Toroidal LHC Apparatus), CMS (Compact Muon Solenoid), ALICE (A Large Ion Col-

lider Experiment) and LHCb are located at the four interaction points where the protons are brought to collision. Figure 3.1 gives a schematic overview of the LHC.

The data used in this analysis were taken during 2011 and 2012. In 2011, the LHC was running at a center of mass energy of $\sqrt{s} = 7$ TeV and the integrated luminosity recorded by LHCb in this year amounts to $\mathcal{L}_{2011} = 1\text{fb}^{-1}$. During 2012, the LHC increased the center of mass energy to $\sqrt{s} = 8$ TeV, and LHCb collected an integrated luminosity of $\mathcal{L}_{2012} = 2\text{fb}^{-1}$. The delivered and collected integrated luminosity for the years 2010-2012 is shown in Figure 3.2.

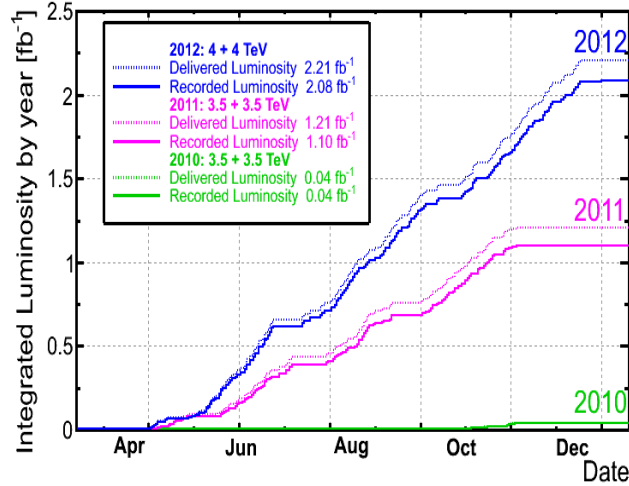


Figure 3.2.: By the LHC delivered and by LHCb recorded integrated luminosity for the years 2010-2012 [20].

3.2. Production of beauty hadrons at the LHC

Beauty quarks are dominantly produced through gluon fusion and quark-anti-quark annihilation at the LHC. The leading order Feynman diagrams for these processes are shown in Figure 3.3 where a) corresponds to the annihilation process and b)-d) to gluon fusion. At the LHC energy scales, the parton density function of the proton is dominated by gluons, which is why diagrams b)-d) contribute dominantly. A produced b quark can hadronize and form a B^\pm , B^0 , B_s^0 meson or a Λ_b^0 baryon.

Due to the low production threshold of a $b\bar{b}$ pair compared to the large center of mass energy, it is possible and likely that gluons with very different momenta form a pair of beauty quarks. This results in the $b\bar{b}$ pairs being boosted in the z -direction along the beam axis. As a consequence, the average flight distance of a b is relatively large, leading to the good time resolution of the LHCb detector. The right hand side of Figure 3.3 shows the simulated polar angle distribution of the b and \bar{b} quarks at $\sqrt{s} = 8$ TeV. The effect of the boost pushing both b and \bar{b} quarks into the forward and backward

direction of the beam axis can be seen. Regarding this fact, the LHCb detector is build as a single-arm forward spectrometer as shown in Figure 3.4. Approximately 25% of the produced $b\bar{b}$ pairs lie inside the LHCb detector acceptance. The b quark pair production

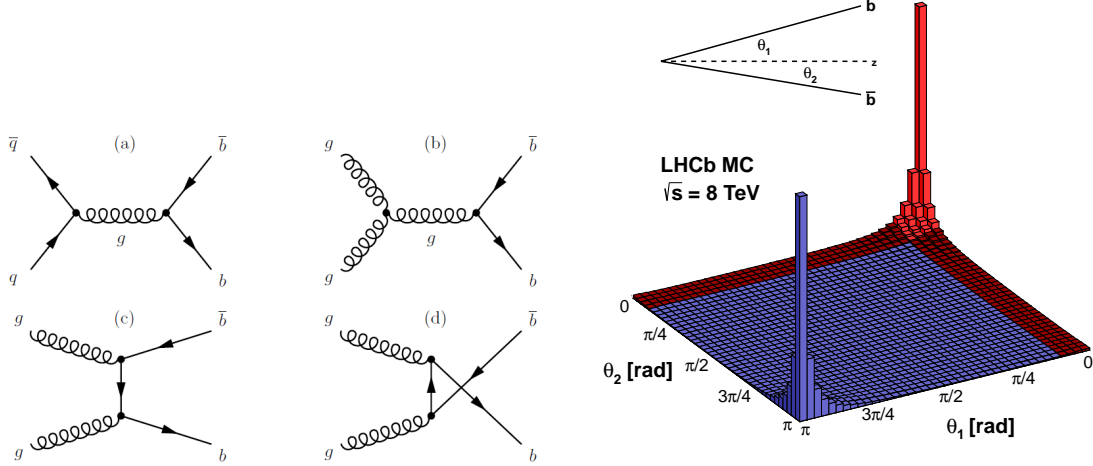


Figure 3.3.: Leading order Feynman diagrams for $b\bar{b}$ production at the LHC [21] and simulated distribution of the polar angles ϑ_1 and ϑ_2 of two b quarks. The LHCb detector acceptance is indicated in red [20].

cross section at the LHC for a center of mass energy of $\sqrt{s} = 7$ TeV was measured to be [22]:

$$\sigma(pp \rightarrow b\bar{b} + X) = (284 \pm 20 \pm 49)\mu b. \quad (3.1)$$

Together with the integrated luminosity of $\mathcal{L}_{2011} = 1fb^{-1}$, one can compute the number of detectable $b\bar{b}$ pairs for 2011:

$$\sigma(pp \rightarrow b\bar{b} + X) \cdot \mathcal{L}_{2011} \cdot 0.25 \approx 7 \cdot 10^{10}. \quad (3.2)$$

3.3. The LHCb Detector

A schematic view of the LHCb Detector is shown in Figure 3.4. This section will summarize the individual detector components [23] that can be divided into components for tracking and for particle identification.

The region of the proton-proton interactions is surrounded by the Vertex Locator (VELO) which provides good spatial resolution of the trajectories of charged particles. There are two more tracking systems to track the signature of charged decay products of the B and D mesons in the detector. One is the Tracker Turicensis (TT) which is located before the dipole magnet and the others are the tracking stations (T1,T2,T3) located behind the magnet. The tracking stations are further divided in the Inner Tracker

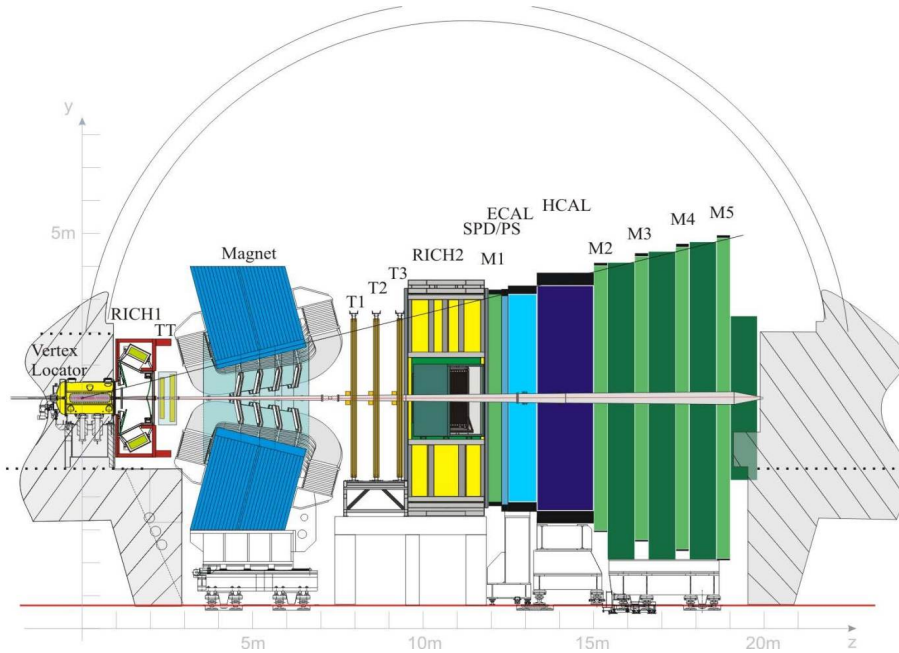


Figure 3.4.: Schematic side view of the LHCb-detector taken from [20]. The proton-proton collision takes place on the left, inside the Vertex Locator(VELO); RICH1 and RICH2 are Cherenkov detectors; TT is the Tracker Turicensis, T1 - T3 the main tracking system, SPD is the Scintillating Pad Detector and PS the Preshower detector; ECAL is the electromagnetic calorimeter, HCAL the hadronic calorimeter and M1 - M5 the muon chambers.

(IT) covering the part of the detector around the beam axis and the Outer Tracker (OT) covering the outer region of the detector. The dipole magnet bends the tracks of charged particle in the x - z plane, where the z -direction is defined by the beam line.

There are two ring-imaging Cherenkov detectors (RICH1,RICH2) installed which are used for particle identification. One is located before and one after the dipole magnet. These detectors are able to distinguish between incoming pions, kaons and protons by the angle under which the particles emit Cherenkov radiation. Located behind RICH2 are the Pre-Shower (PS) and the Scintillating Pad Detector (SPD). They are followed by the electromagnetic and hadronic calorimeters (ECAL and HCAL) in which the final state particles deposit their energy. For muon detection, there are five dedicated chambers at the end of the detector (M1-M5), where M1 is placed in front and M2-M5 are placed behind the calorimeters. Due to the fact that muons interact very little with the detector material, they are the only particles capable of penetrating M2-M5.

3.3.1. Tracking detectors

A charged particle leaves signatures in the VELO, the TT before and in the tracking stations after the dipole magnet. With this information, the trajectory of the particle

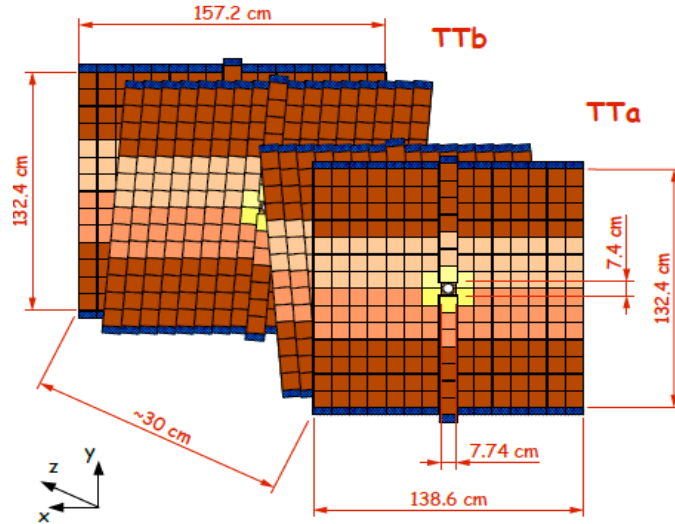


Figure 3.6.: Geometry and length scale of the TT. Figure taken from [24].

The IT consists of silicon strip sensors similar to the TT. Each of the three stations T1-T3 consists of four layers in a (x,u,v,x) scheme, where again the u and v layers are rotated by $\pm 5^\circ$ with respect to the x layers. Figure 3.7 visualizes the geometry and length scale of one IT x layer. The spatial single hit resolution is comparable to the TT with approximately $50\mu\text{m}$.

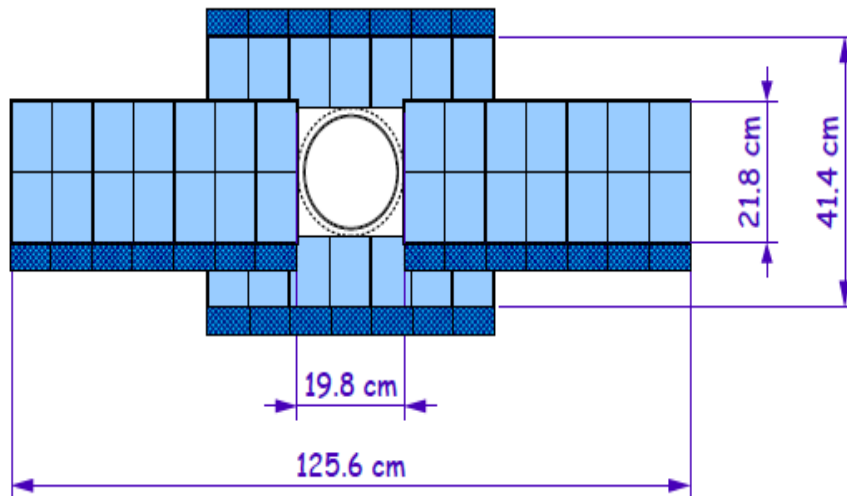


Figure 3.7.: Geometry and length scale of an IT x layer. Figure taken from [24].

The OT is built as a gas detector with straw tubes. It covers the outer detector region. A spatial hit resolution of approximately $200\mu\text{m}$ can be achieved. The layout of the straw tubes inside the OT is shown in Figure 3.8.

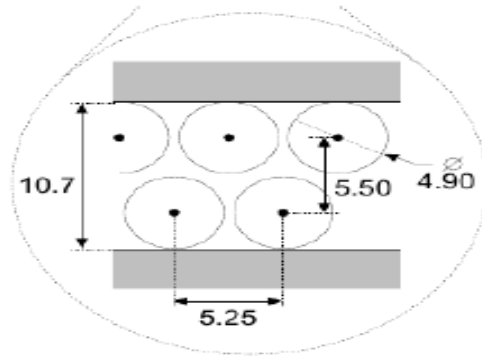


Figure 3.8.: Layout of the straw tubes inside an OT module. Numbers in mm [23].

3.3.2. Particle identification

Once the track of a charged particle has been reconstructed, it is crucial to determine the particle type. This is achieved with the Imaging Cherenkov Detectors RICH 1 and RICH 2, the calorimeter systems and the muon chambers.

Ring Imaging Cherenkov Detectors

The RICH Detectors are used to identify charged particles based on Cherenkov radiation. A particle that traverses a medium faster than the speed of light in this medium, emits photons under an angle ϑ that is directly related to the particles velocity by

$$\cos(\vartheta) = \frac{1}{\beta n}, \quad (3.3)$$

where $\beta = \frac{v}{c}$ is the velocity fraction with respect to the speed of light in vacuum and n is the index of refraction of the medium the particle traverses through. The light is guided through the RICH using mirrors until it reaches the Hybrid Photo Detectors (HPD). Photons emitted by a charged particle form a cone which is then detected as a ring. The radius of the ring is proportional to the cone angle ϑ under which the photons were emitted. Together with the momentum information from the tracking stations, the rest mass of the particle can be computed:

$$m_0 = \frac{p}{\beta\gamma}. \quad (3.4)$$

The knowledge of the rest mass allows the determination of the particle type. For the purpose of LHCb, the charged particles which have to be identified and separated from each other by the RICH detectors are mainly pions, kaons and protons.

RICH1 is located upstream of the dipole magnet and covers a momentum range from approximately 1 to 60 GeV/c . It is filled with aerogel and C_4F_{10} gas. RICH2 is placed behind the main tracking stations and covers the higher momentum range from approx-

imately 15 to 100 GeV/c . Therefore, it is filled with the optical dense CF_4 gas. The geometry of the RICH1 detector is shown in Figure 3.9.

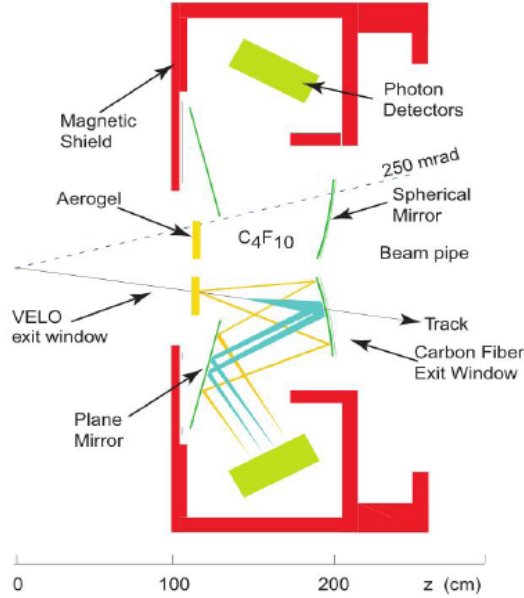


Figure 3.9.: Geometry of the RICH1 detector (side view) taken from [23].

Calorimeters

With the calorimeters photons, electrons and hadrons can be identified and their energy and position can be measured. The calorimeters use the fact that an incoming particle produces a shower of secondary particles in the absorber material and light in the interleaved plastic scintillators. The corresponding scintillation light is then detected using Photo Multiplier Tubes (PMTs). The four components of the calorimeter system in the LHCb detector are the Preshower Detector (PS), the Scintillator Pad Detector (SPD), the Electromagnetic Calorimeter (ECAL) and the Hadronic Calorimeter (HCAL). Their alignment is shown in Figure 3.4.

The SPD consists of scintillating layers which are 15 mm thick. Its main purpose is to distinguish between electrons and photons because only the former ones can be detected with this setup. It is also used to induce electromagnetic showers with a lead plate installed behind the SPD.

The PS is built similar to the SPD. It is used to distinguish between hadronic and electromagnetic showers using the fact that hadrons in general deposit very little energy in this calorimeter.

The ECAL is composed of alternating layers of active material (4 mm thick scintillating pads) and absorbers (2 mm thick lead). This way, the size of the ECAL can be held compact while it is likely that an electron or photon deposits its entire energy in the calorimeter with the material corresponding to 25 radiation lengths. Showers induced

by electrons and photons are detected by PMTs. The obtained energy resolution is

$$\frac{\sigma(E)}{E} = \frac{10\%}{\sqrt{E}} \oplus 1.5\%, \quad (3.5)$$

where the \oplus symbolizes quadratic summation and the energy is measured in GeV.

The HCAL is structured similarly to the ECAL with absorber layers of iron that are 1 cm thick. The total length of absorber and scintillating material corresponds to 5.6 hadronic interaction lengths and ensures that hadronic showers are initiated and can be detected. The energy resolution of the HCAL is:

$$\frac{\sigma(E)}{E} = \frac{80\%}{\sqrt{E}} \oplus 10\%. \quad (3.6)$$

3.3.3. The muon system

The detection of muons is achieved with the five muon stations M1-M5. M1 is located in front of the calorimeter system while M2-M5 are behind the calorimeters at the end of the detector because muons are expected to be the only particles to penetrate the whole LHCb detector due to their minimal ionizing behavior. The muon chambers M2-M5 consist of Multi Wire Proportional Chambers (MWPCs) which use gaseous ionization detection to measure the trajectory of a muon. The M1 chamber is built differently due to the higher particle flux that is expected in its inner part. There it consists of a gas electron multiplier (GEM) detector. The achieved momentum resolution is approximately 20%.

3.3.4. Event reconstruction

The information of all detector components described above is combined and used to fully reconstruct decay signatures, e.g. the decay $B_s^0 \rightarrow \phi\phi$. In natural units, where the Planck constant and the speed of light are $\hbar = c = 1$, the four momentum vector of a particle can be expressed through the energy $E = \sqrt{m^2 + \vec{p}^2}$ and the three-momentum vector \vec{p} . Since the mass of a particle is not directly measured in an event, the PDG (particle data group [25]) value corresponding to the particle hypothesis is assigned as particle mass. The resulting four momentum \mathbf{p} is then given by:

$$\mathbf{p} = (E, \vec{p}) = (\sqrt{m_{PDG}^2 + \vec{p}^2}, \vec{p}). \quad (3.7)$$

For the $B_s^0 \rightarrow \phi\phi$ decay, the tracks of each kaon pair are used to reconstruct the vertex of the ϕ mesons. The four momentum \mathbf{p}_{ϕ_i} of the ϕ_i meson is calculated as the sum of the kaon four momenta

$$\mathbf{p}_{\phi_i} = \mathbf{p}_{K_i^+} + \mathbf{p}_{K_i^-}. \quad (3.8)$$

The information of all four tracks and the two decay vertices of the ϕ mesons is combined to reconstruct the decay vertex of the B_s^0 meson. This vertex is also called secondary vertex (SV). Since the B_s^0 meson is directly produced in the pp collisions, the production

vertex of the B_s^0 is the proton-proton interaction point which is called primary vertex (PV). The four-momentum of the B_s^0 meson is computed using the reconstructed ϕ momenta:

$$\mathbf{p}_{B_s^0} = \mathbf{p}_{\phi_1} + \mathbf{p}_{\phi_2}. \quad (3.9)$$

Figure 3.10 shows the decay signature of $B_s^0 \rightarrow \phi\phi \rightarrow K^+K^-K^+K^-$ decays.

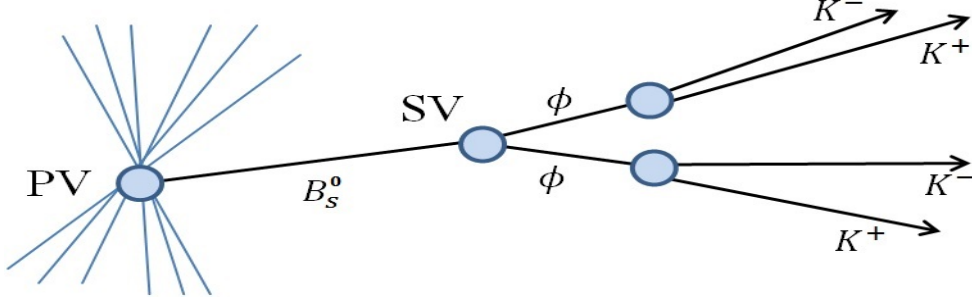


Figure 3.10.: Illustration of the reconstruction of the decay $B_s^0 \rightarrow \phi\phi$. PV is the primary vertex and SV the secondary Vertex.

Once the decay signature is fully reconstructed, the lifetime of the B_s^0 meson can be determined. Denoting $s_{pv}^{\vec{}}$ as the position vector of the primary vertex and $s_{sv}^{\vec{}}$ as the position vector of the secondary vertex, one can express the flight distance s of the B_s^0 meson as $s = |s_{sv}^{\vec{}} - s_{pv}^{\vec{}}|$. Together with the velocity β (using natural units) and $\gamma = 1/\sqrt{1 - \beta^2}$, the decay time t of the B_s^0 meson can be calculated as:

$$t = \frac{s}{\gamma v} = \frac{s}{\gamma \beta} = s \sqrt{\frac{1}{\beta^2} - 1} = s \sqrt{\frac{E^2}{p^2} - 1} = \frac{ms}{p} = \frac{m \vec{s} \cdot \vec{p}}{|\vec{p}|^2} = \frac{m \cdot (s_{sv}^{\vec{}} - s_{pv}^{\vec{}}) \cdot \vec{p}}{|\vec{p}|^2}. \quad (3.10)$$

3.3.5. The LHCb trigger system

Events used in this analysis are required to pass the three different trigger stages of LHCb. They are designed to reduce the event rate from the nominal beam crossing rate of 40 MHz to roughly 5 kHz with which data can be recorded for the physics analysis. Figure 3.11 gives an overview of the trigger scheme.

The first stage is the L0 hardware trigger which reduces the event rate to approximately 1.1 MHz. This is sufficient to enable the electronics to read out the whole LHCb detector. Since the B mesons mass is relatively high, the L0 trigger searches for final state particles with relatively high transverse energies and momenta E_t and p_t using information from the calorimeter system and the muon chambers. At this stage, a particle hypothesis is assigned to tracks accepted by the L0 trigger (L0-Hadron, L0-Photon, L0-Electron, L0-Muon).

The other two stages are the High Level Trigger HLT1 and HLT2. They are based on software applications which are used to filter out unwanted background events.

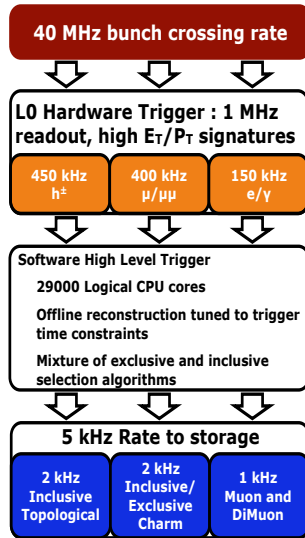


Figure 3.11.: LHCb Trigger scheme taken from [20].

In the HLT1, events are partially reconstructed using the VELO information as well as information from the TT and T1-T3 stations with the purpose of fast track reconstruction. HLT1 further reduces the event rate to roughly 30 kHz.

The HLT2 stage fully reconstructs events using all available information from the tracking and particle identification. Tracks are reconstructed to meet requirements for certain composite particles, for example the combination of two muons to the decay $J/\Psi \rightarrow \mu\mu$. Topological trigger lines in the HLT2 attempt to reconstruct every b-hadron decay with two or more particles in the final state. With this stage, the event rate is reduced to the targeted 5 kHz.

Analysis strategy

The triple product asymmetries A_U and A_V introduced in Section 2.5 present the possibility of a CP violation measurement which is decay-time independent. To extract the triple product asymmetries it is crucial to determine the number of $B_s^0 \rightarrow \phi\phi$ signal events with negative and positive signs of $U = \sin 2\Phi$ and $V = \pm \sin \Phi$. This is achieved by subdividing the selected decays according to the sign of U and V. In order to determine the triple product asymmetries, several issues have to be addressed:

- To obtain the signal candidates, the $B_s^0 \rightarrow \phi\phi$ events have to be fully reconstructed including the two kaon pairs in the final state and the two intermediate ϕ mesons. An efficient selection process is required to discriminate the $B_s^0 \rightarrow \phi\phi$ signal events from physical and combinatorial backgrounds present in the data sample.
- The selection described in Chapter 5 is unable to remove all physical backgrounds. This means that the possible contributions of other decays mimicking the $B_s^0 \rightarrow \phi\phi$ decay have to be identified, accounted for and included in the background part of the fit function used to extract the triple product asymmetries A_U and A_V .
- The measured decay time and angular distributions are distorted by efficiency effects that are introduced by the geometrical coverage of the detector and by trigger and selection requirements. Since this measurement relies on the distribution of $B_s^0 \rightarrow \phi\phi$ events in terms of the helicity angles θ_1 , θ_2 and Φ , the efficiency depending on the angular distributions has to be studied. The angular acceptance correction is determined using simulated $B_s^0 \rightarrow \phi\phi$ candidates. Although the presented analysis is time-integrated, the decay-time efficiency has an influence on the triple products U and V. Decay-time acceptance effects are investigated using the $B_s^0 \rightarrow D_s^+ \pi^-$ decay as a reference channel.
- Simultaneous unbinned maximum likelihood fits are performed to the fully selected distributions of the $B_s^0 \rightarrow \phi\phi$ candidates to extract the number of events with positive and negative signs of U and V.

Selection of $B_s^0 \rightarrow \phi\phi$ candidates

In this Chapter, the selection of $B_s^0 \rightarrow \phi\phi$ signal candidates is described. The different selection steps include the trigger selection which decides whether an event is stored and a rough selection of signal candidates. The last step is analysis-dependent and optimized for the purpose of the presented measurement. The measurement uses the full LHCb 2011 and 2012 data corresponding to an integrated luminosity of $3.1fb^{-1}$.

5.1. Trigger selection

The $B_s^0 \rightarrow \phi\phi$ candidates are required to pass the L0 hadron trigger. The hadron trigger combines the information of the electromagnetic and hadronic calorimeter to detect hadron candidates in an event. The calorimeters are able to measure the transverse energy E_t of a particle as discussed in Section 3.3. In case of a hadronic shower, the energy deposited in the ECAL is added to the energy in the HCAL. The L0 hadron trigger is issued once the transverse energy of resulting hadronic cluster is above $3.5 GeV$ [26]. If only the L0 hadron trigger is used the efficiency for the $B_s^0 \rightarrow \phi\phi$ decay is low due to the rejection of all K^+K^- pairs with a combined transverse energy of $(E_{t_{K^+}} + E_{t_{K^-}}) < 3.5 GeV$. Thus, an event is also kept if any of the other L0 triggers are issued independently of the hadron trigger.

Events which pass the previous stage are required to pass the HLT2 topological trigger¹ or the HLT2 ϕ trigger². The topological trigger searches for the combination of two particle tracks in a wide mass window from 4 to 6 GeV/c^2 [26]. The tracks are required to have a combined transverse momentum of $(p_{t_1} + p_{t_2}) > 2.5 GeV/c$. To provide robustness against inefficiencies, the topological trigger is constructed in such a way that it is issued even if one of the tracks is not fully reconstructable. The HLT2 ϕ trigger [27] is fired if the decay $\phi \rightarrow K^+K^-$ is reconstructed. First, a separated vertex with two particle tracks is preselected. Then, the information from the Cherenkov detectors is used to identify the kaon pair and separate it from the large background of wrongly reconstructed pions.

¹The HLT2Topo2BodyDecision trigger line is used.

²The HLT2IncPhiDecision trigger line is used.

5.2. Pre-Selection of the $B_s^0 \rightarrow \phi\phi$ decay

The reconstruction of $B_s^0 \rightarrow \phi\phi$ decays is based on the selection of two oppositely charged kaon pairs, where the invariant mass of each pair is equal to the mass of a ϕ meson. Since the ϕ mesons decay via the strong interaction, their lifetimes are so short that they seem to decay immediately. Thus, the combined vertices of the four kaons are used to reconstruct the decay vertex of the B_s^0 meson. To ensure that the selected kaons originate from this vertex and are not produced in the proton-proton collision, the impact parameter (IP) of each kaon with respect to the B_s^0 production vertex is used. In Figure 5.1, the B meson originates from the primary vertex (PV) and the kaon

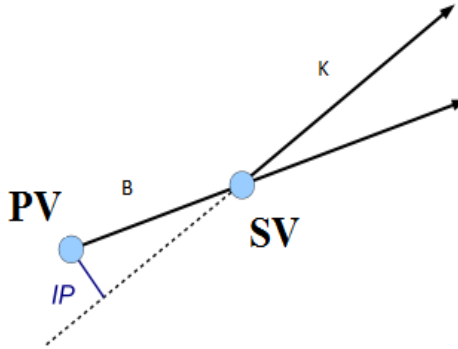


Figure 5.1.: Definition of the impact parameter as reconstruction variable.

is produced at the secondary vertex (SV). The IP is defined as the distance of closest approach of the kaon track and the PV. The IP significance is then defined to be the ratio of the impact parameter to its measured uncertainty:

$$IP_{sig} = \frac{IP}{\sigma_{IP}}. \quad (5.1)$$

Each kaon is required to exhibit a squared impact parameter significance IP_{sig}^2 of larger than 25 in order to suppress kaons originating from the PV that would contribute to background. To further separate signal-like kaons from background contributions, a cut on the transverse momentum $p_t > 400 \text{ MeV}/c$ is imposed. This uses the fact that the transverse momentum of each ϕ meson $p_t(\phi)$ is relatively high, because they originate from the heavy B_s^0 meson. Therefore, also the transverse momenta of the kaon signal candidates $p_t(K)$ are high with respect to background kaons originating from the pp collisions.

The next reconstruction step is to combine two kaons from a ϕ mesons. The invariant mass of each ϕ candidate is required to be within a $25 \text{ MeV}/c^2$ window around its PDG mass. Both ϕ mesons are the direct decay products of the heavy B_s^0 meson. Therefore, the signal ϕ candidates are expected to have relatively high transverse momenta with respect to immediately produced background ϕ 's. A cut on the product of both transverse ϕ momenta $p_t(\phi_1) \times p_t(\phi_2)$ to be greater than $2 \text{ GeV}^2/c^2$ is enforced to reduce

the number of background candidates. To further ensure a good vertex reconstruction quality, the χ^2 per degree of freedom of the fit algorithm that reconstructs the vertex of each ϕ is used. The $\chi^2/nDoF$ of each ϕ meson vertex is required to be less than 15.

The last step is to combine the two signal ϕ candidates to form a B_s^0 meson. Here again, the $\chi^2/nDoF$ of the vertex fit is used and required to be smaller than 15. This enforces a clean B_s^0 production vertex.

A summary of all selection cuts described above can be found in Table 5.1. The invariant mass distributions of $B_s^0 \rightarrow \phi\phi$ candidates after the pre-selection cuts are applied, are shown for 2011 and 2012 in Figure 5.2. A small peak at the nominal B_s^0 mass is visible, but the background remains large. Therefore, an additional, multivariate selection process is applied, which is described in the following.

Variable	Stripping Cut
Kaon IP_{sig}^2	> 25
Kaon p_t	$> 400 MeV/c$
$ M_{KK} - M_{\phi}^{PDG} $	$< 25 MeV/c^2$
$\phi^1 p_t \times \phi^2 p_t$	$> 2 GeV^2/c^2$
B_s vertex χ^2 per NDF	< 15
ϕ vertex χ^2 per NDF	< 15

Table 5.1.: Summary of the pre-selection cuts for $B_s^0 \rightarrow \phi\phi$ candidates.

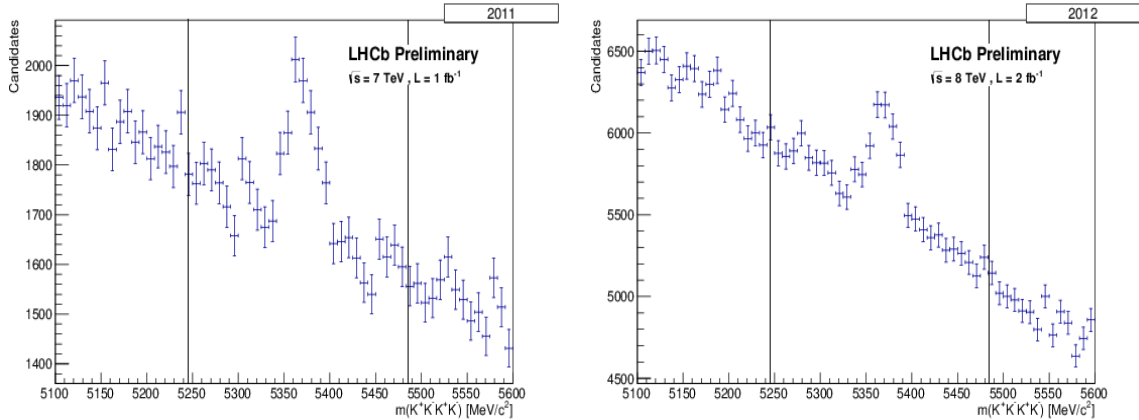


Figure 5.2.: Invariant mass distributions of pre-selected $B_s^0 \rightarrow \phi\phi$ candidates for (left) 2011 and (right) 2012 data. The region further away than $120 MeV/c^2$ from the PDG mass of the B_s^0 meson is located to the left and right of the vertical lines.

5.3. Multivariate selection

To further discriminate the $B_s^0 \rightarrow \phi\phi$ signal decays from background passing the previous selection steps, a multivariate analysis technique with event-dependent selection cuts is used. This tool combines multiple variables with separation power and returns a single dimensionless response for every event. This is done by comparing typical event signatures in signal and background events. The response contains the information from each variable and combines them in an efficient way. The multivariate tool used in this analysis is also called boosted decision tree (BDT) [28]. A decision tree is a binary structured object that repeats yes/no decisions for a single variable at each node of the tree until a stop-criterion is reached. At each node of the tree, the variable with the highest separation power between signal and background is chosen to classify the tested event. Figure 5.3 visualizes the structure of a decision tree.

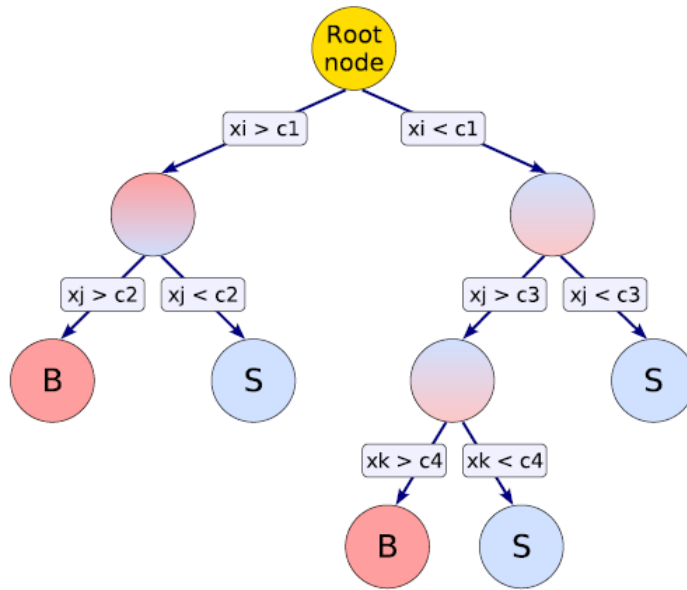


Figure 5.3.: Schematic view of a decision tree taken from [29]. Starting from the "Root Node" a sequence of binary splits is performed using the discriminating variable x_i to separate between signal and background. Each node represents a decision similar to a cut-based selection. The final leaves are labeled signal (S) or background (B) depending on the structure of the events that end up in a certain leaf.

The separation power of one decision tree depends on the statistical fluctuation of the input samples. To increase the robustness of the BDT method, a procedure called *boosting* is applied. In the boosting, the procedure to build a decision tree is repeated and, in each iteration, sample events which are assigned to a wrong leaf, i.e. background events that end up in a signal leaf or vice versa, are given a larger weight [30]. In this way, a large number of decision trees is built, giving rise to the name decision forest.

The final classification of signal or background for each event is obtained by looping over all decision trees and assigning a weight of +1 for every tree in which the event ends up in a signal leaf and -1 for each tree the event ends up in a background leaf. The classification of an event is also called response and is normalized to the number of trees in the decision forest.

The TMVA package [31] is used to implement the BDT method. To *train* the decision trees, samples of signal and background events are required. Training refers to the process that defines the splitting criteria at each node of the tree [29]. The training process starts at the root node, where the initial splitting criterion for the training sample is determined by comparing the variable with the highest separation power between signal and background for the whole sample. This results in two subsets of events that further go through the algorithm of determining the next split criterion. The algorithm continues until the minimal number of 2.5% of all sample events for the next node split is reached. The resulting leaf nodes are classified as signal or background depending on the class of the majority of events they belong to [32]. The binary structure of each decision tree is similar to a purely cut-based selection process. However, the advantage arises from the fact that, while a selection cut is only able to select one hypercube region of the available phase space, the decision tree can select many hypercubes, each of which is identified as a signal-like or a background-like region. The cut sequence for each event is individual as it passes the nodes of the decision tree.

Fully simulated and correctly reconstructed events are used for the signal sample. They are required to pass the same pre-selection steps as the real collision data. The invariant mass distributions of the simulated and pre-selected $B_s^0 \rightarrow \phi\phi$ candidates is shown in Figure 5.4, where signal events are chosen within a region of $120 \text{ MeV}/c^2$ around the PDG mass of the B_s^0 meson, indicated by the dotted line. The background sample is taken from the data sideband region, defined to be more than $120 \text{ MeV}/c^2$ away from the PDG mass of the B_s^0 , as indicated in Figure 5.2. The distributions of the input variables for the 2011 and 2012 BDT training are shown in the Appendix.

The used training variables are:

- The neural network particle identification variable, which quantifies the kaon's probability to indeed be a kaon (ProbNNk). This variable combines information from the RICH 1&2, the PS, SPD, ECAL and the HCAL to determine the probability of the respective particle hypothesis to be assigned correctly. It is built in a way that summing over all probabilities for the different particle hypothesis gives 1.
- The maximum track χ^2 per degree of freedom.
- The B_s^0 vertex χ^2 per degree of freedom.
- Cosine of the angle between the direction of the momentum and the flight direction of the B_s^0 .
- $\ln(p_t)$ of the B_s^0 , the ϕ candidates and the maximum and minimum $\ln(p_t)$ of the kaon tracks.

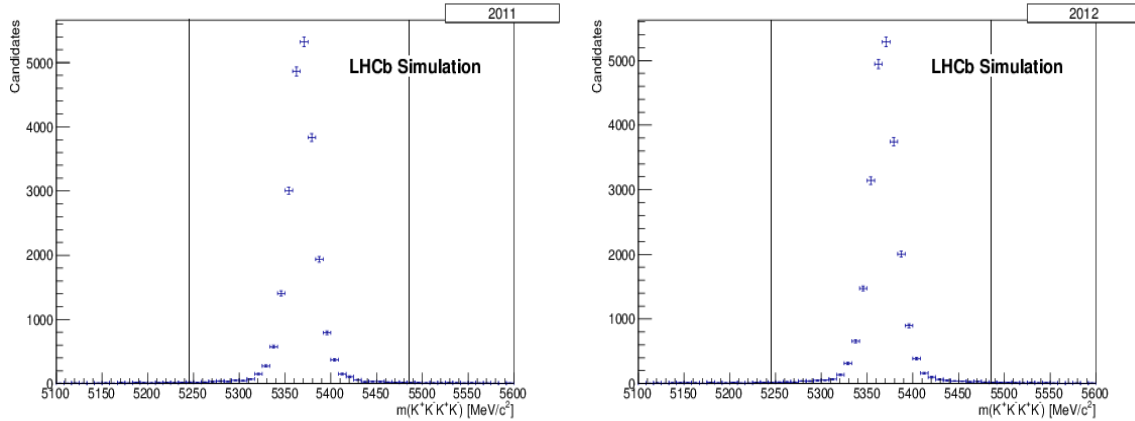


Figure 5.4.: Invariant mass distributions of pre-selected, simulated $B_s^0 \rightarrow \phi\phi$ candidates for (left) 2011 and (right) 2012. The vertical lines indicate the region of $120 \text{ MeV}/c^2$ around the PDG mass of the B_s^0 meson.

- The pseudorapidity $\eta = \frac{1}{2} \ln\left(\frac{E+|\vec{p}|}{E-|\vec{p}|}\right)$ of the B_s^0 , each ϕ and the minimum and maximum of the kaon tracks.
- The cone p_t asymmetry of each track. This variable is defined as the difference between the p_t of the kaon and the sum of all other p_t in a cone of radius $r = \sqrt{(\Delta\Phi)^2 + (\Delta\eta)^2} < 1$ rad around the signal kaon track.

Separate boosted decision trees are trained for 2011 and 2012 data to account for possible differences in the variable distributions, as the center of mass energy of the proton-proton collisions is $\sqrt{s} = 7 \text{ TeV}$ for 2011 and $\sqrt{s} = 8 \text{ TeV}$ for 2012. To test the reliability of a BDT, the input sample is evenly split into the training sample, with which the decision trees are built and the independent test sample. If the BDT method is implemented correctly, the test sample should reproduce the results of the training sample when the decision trees built with the training sample are applied to the test sample. Figure 5.5 shows the signal and background distribution for the test and training sample in dependence of the BDT response cut. Overtraining can occur when too many nodes of a BDT are matched to too few events. This would lead to a seemingly increased performance in the training sample and an effective decrease when measured with an independent test sample. Therefore, both samples are superimposed to detect possible overtraining. Since the distributions of the test and training samples in Figure 5.5 are in good agreement, there is no sign of overtraining.

To determine the optimal cut value on the BDT response, the TMVA package [31] provides a plot showing the signal efficiency, purity and the figure of merit $S/\sqrt{S+B}$ in dependence of the BDT output value. Here, S is the number of signal events and B the number of background events. These plots are shown in Figure 5.6. For the determination of the optimal cut value, an estimation for the expected number of signal events in the data sample is required. This number is approximated by scaling the signal

yield of a previous analysis in the $B_s^0 \rightarrow \phi\phi$ mode [18]. The scale factor accounts for the higher statistics when the full 2011 and 2012 data corresponding to an integrated luminosity of $\mathcal{L} = 3.1\text{fb}^{-1}$ is used. The number of background events is then determined by the difference between the expected signal yield and the complete number of events in the data set passing the previous selection steps. The highest value of $S/\sqrt{S+B}$ is obtained by cutting at 0.1217 for the 2011 data and 0.1081 for the 2012 data. Figure 5.7 shows the invariant mass distributions of fully selected $B_s^0 \rightarrow \phi\phi$ candidates.

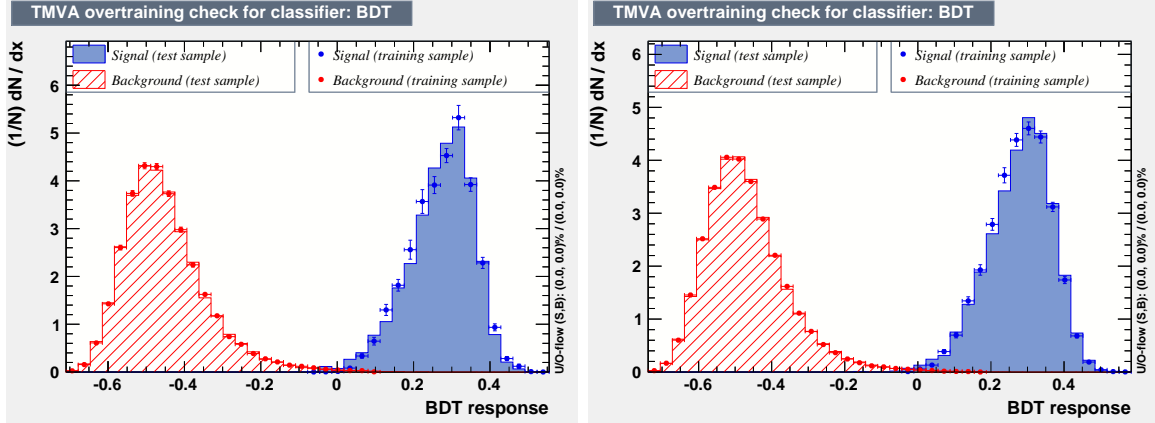


Figure 5.5.: BDT response for (left) 2011 and (right) 2012. The test and training samples are superimposed to check for possible overtraining.

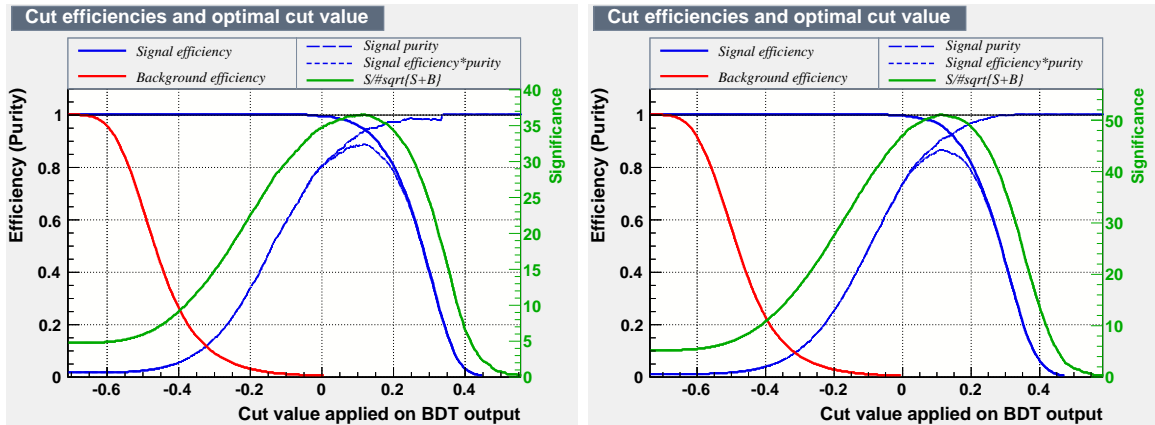


Figure 5.6.: BDT efficiency for (left) 2011 and (right) 2012 in dependence of the cut value applied on the BDT output.

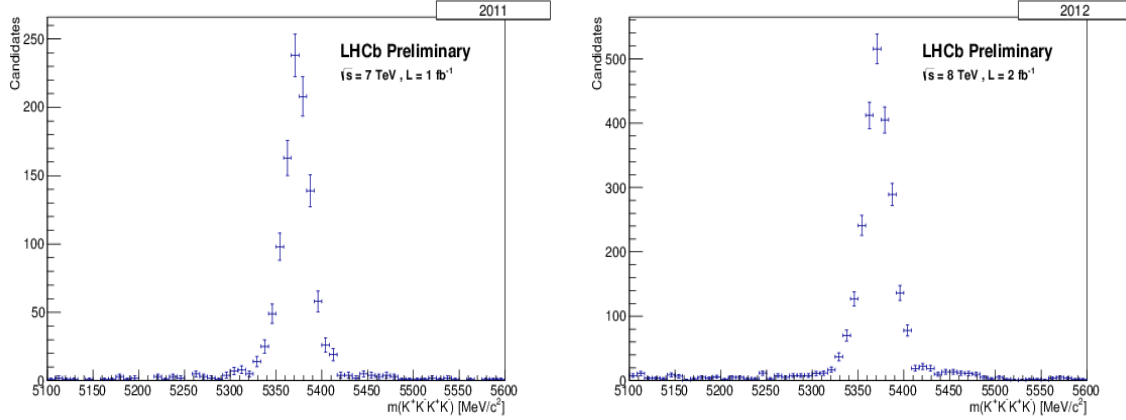


Figure 5.7.: Invariant mass distributions of fully selected $B_s^0 \rightarrow \phi\phi$ candidates for (left) 2011 and (right) 2012 data.

5.4. Comparison of simulation and data

Simulated events are used to train the BDT. Therefore, it is important to ensure good agreement between the simulation and real events. Comparing the distributions of the kaon track $\chi^2/nDoF$ and the neural network PID variable (ProbNNk) in simulation and data, one observes significant differences as can be seen in Figure 5.8. The main reason for the disagreement of the ProbNNk distributions is the difference of the number of silicon pad detector (SPD) hits in simulation and data. Therefore, a two-dimensional re-weighting is performed using the kaon track $\chi^2/nDoF$ and the number of SPD hits to improve the agreement between simulation and data. For the re-weighting, two-dimensional histograms with the number of SPD hits and the kaon track $\chi^2/nDoF$ are generated for data and for simulation separately. The histograms are normalized to one and the data histogram is divided by the simulation histogram. The histogram can be used to assign a weight to a simulated $B_s^0 \rightarrow \phi\phi$ event and ensure closer agreement with the real data. The assigned weight depends on the values of the number of SPD hits and the kaon track $\chi^2/nDoF$ variable in the simulated $B_s^0 \rightarrow \phi\phi$ event, with respect to the distributions in real data. Figure 5.8 shows the effect of the re-weighting procedure. Good agreement can be seen between the data and the re-weighted simulation.

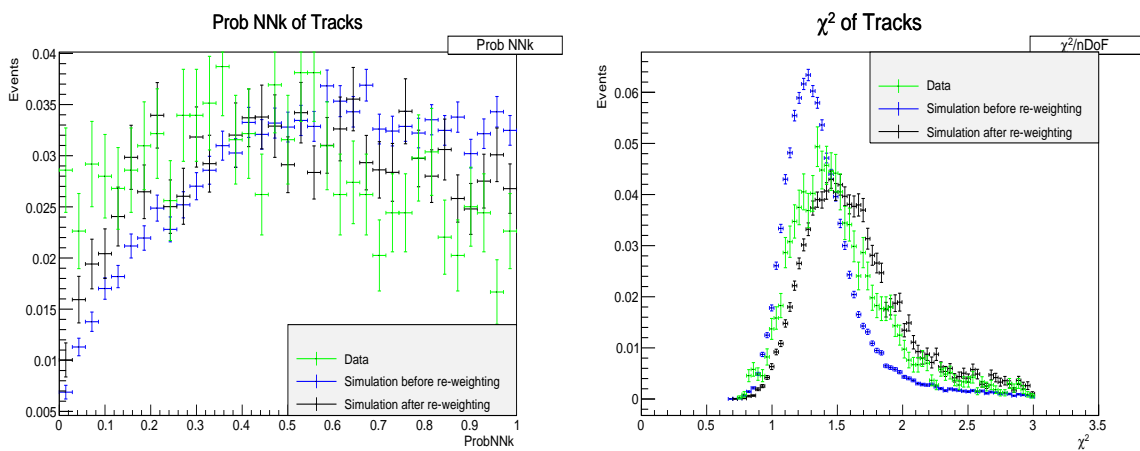


Figure 5.8.: Comparison of the (left) ProbNNk variable and the (right) track χ^2 per degree of freedom in simulation and data. Data in green, simulation in blue before two-dimensional re-weighting of events using the track χ^2 and the number of SPD hits and black after.

Description of fitting procedure

To extract the triple product asymmetries A_U and A_V , a *simultaneous unbinned maximum likelihood fit* is performed to the invariant mass distributions of the separated data sets to estimate the number of events with positive and negative sign of U and V respectively. The maximum likelihood fit algorithm estimates a set of a priori unknown parameters, $\vec{\lambda} = \{\lambda_1, \lambda_2, \dots\}$ of a theoretical distribution, $f(\vec{x}; \vec{\lambda})$, from a set of measured observables, $\vec{x} = \{x_1, x_2, \dots\}$, [33]. In this case, the observables are the masses m_- and m_+ of the $B_s^0 \rightarrow \phi\phi$ candidates with positive and negative sign of U and V, respectively. The probability density function (PDF), $\mathcal{P}(\vec{x}_i; \vec{\lambda})$, describes the probability to measure the data \vec{x} with parameters $\vec{\lambda}$:

$$\mathcal{P}(\vec{x}_i; \vec{\lambda}) = \frac{f(\vec{x}_i; \vec{\lambda})}{\int f(\vec{x}'_i; \vec{\lambda}) d\vec{x}'_i}, \text{ with } \mathcal{P} > 0, \int \mathcal{P} dx = 1. \quad (6.1)$$

The index i denotes the respective event. The product of the single event probabilities of all events N is then defined to be the likelihood function:

$$\mathcal{L}(\vec{x}; \vec{\lambda}) = \prod_i^N \mathcal{P}(\vec{x}_i; \vec{\lambda}). \quad (6.2)$$

Defined in this way, the likelihood function returns the probability of a parameter set $\vec{\lambda}$ to describe the given data \vec{x} . To extract the most likely parameter set, this function is maximized and the related fit method is referred to as **maximum likelihood method**. The term **unbinned** is added because the data sets \vec{x}_i are not combined in bins prior to the fit procedure. The presented analysis uses the Minuit framework [34], where the likelihood function is defined with a negative sign and is therefore minimized. The PDF used for this analysis is composed of a signal part S and a background part B :

$$\mathcal{P}(\vec{m}; \vec{\lambda}) = \sum_{i \in \{+, -\}} \left(f_i^s S(m_i; \vec{\lambda}) + f_i^b B(m_i; \vec{\lambda}) \right), \quad (6.3)$$

where f_i^j stands for the signal and background yield and $\vec{\lambda}$ includes all fit parameters. The summation is performed for all events with positive and negative U and V. For the mass distribution of the signal events, a sum of two Gaussian functions describing the

B_s^0 mass peak is used:

$$S(m; \bar{m}, \sigma_1, \sigma_2, f) = \frac{f}{\sqrt{2\pi}\sigma_1} \cdot e^{-\frac{(m-\bar{m})^2}{2\sigma_1^2}} + \frac{1-f}{\sqrt{2\pi}\sigma_2} \cdot e^{-\frac{(m-\bar{m})^2}{2\sigma_2^2}}, \quad (6.4)$$

where m is the invariant mass, \bar{m} is the mean and σ_i the width of the respective Gaussian. The factor f denotes the fraction of each Gaussian contributing to the double Gaussian. The background part of the PDF will have to include different components describing combinatorial and physical background:

$$B(m; \vec{\lambda}) = f_{\text{comb}} \cdot B(m; \vec{\lambda})_{\text{comb}} + (1 - f_{\text{comb}}) \cdot B(m; \vec{\lambda})_{\text{phys}}, \quad (6.5)$$

where f_{comb} is the fraction of combinatorial background, $(1 - f_{\text{comb}})$ is the fraction of physical background, $B(m; \vec{\lambda})_{\text{comb}}$ is the part of the PDF which describes the shape of the combinatorial background and $B(m; \vec{\lambda})_{\text{phys}}$ describes the physical background. The exact form of this PDF is discussed in Chapter 7 and 10. The fit procedure is described in detail in Chapter 10.

In the following chapters, a Crystal Ball function is used to model invariant mass distributions. The Crystal Ball function is given by a Gaussian core with an exponential tail [35]

$$F_{CB}(m; \bar{m}, n, \alpha, \sigma) = N \cdot \begin{cases} \exp\left(-\frac{(m-\bar{m})^2}{2\sigma^2}\right) & \text{for } \frac{m-\bar{m}}{\sigma} < \alpha \\ A \cdot \left(B - \frac{m-\bar{m}}{\sigma}\right)^{-n} & \text{for } \frac{m-\bar{m}}{\sigma} \geq \alpha \end{cases}, \quad (6.6)$$

where \bar{m} and σ are the usual mean and width of the Gaussian function, n parametrizes the slope of the exponential tail and α determines the cut-off value from which the tail starts. A and B are coefficients determined by n and α .

Backgrounds from other b-hadron decays

Background sources from real physical decays are not distributed flat in the B_s^0 mass spectrum as it is the case for combinatorial background. Instead, some of the physical background contributions can peak in the mass region of the $B_s^0 \rightarrow \phi\phi$ signal where they cannot be distinguished from signal events and introduce a systematic error to the triple product asymmetries. The possible physical background components therefore have to be determined, investigated and accounted for in the simultaneous fits to the $B_s^0 \rightarrow \phi\phi$ mass distribution. The most prominent candidates for physical backgrounds, due to the similar rest mass and kinematics, are decays of B mesons with four body final states that involve kaons and pions. Those two particles are hard to separate with the RICH system and mis-identifications are most probable for them compared to other candidates. Four-body final states, where a proton is mis-identified as a kaon, are also considered. The possible decays that might contribute to the physical backgrounds are:

- $B^+ \rightarrow \phi K^+ \rightarrow K^+ K^- K^+$, where an additional random K^- is added during the event reconstruction.
- $B^0/B_s^0 \rightarrow \phi\pi^+\pi^- \rightarrow K^+ K^- \pi^+ \pi^-$
- $\Lambda_b^0 \rightarrow \phi K^- p \rightarrow K^+ K^- K^- p$
- $B^0/B_s^0 \rightarrow \phi K^*(892) \rightarrow K^+ K^- K^\pm \pi^\mp$

The charge-conjugate processes of the decays listed above are also considered. The possible sources of physical backgrounds, also called peaking backgrounds, are investigated by reconstructing the fully selected $B_s^0 \rightarrow \phi\phi$ candidates of 2011 and 2012 data under each of the four final state particle hypothesis listed above. This is done by changing the original value of the mass assigned to the reconstructed particle (in this case the kaon) to the PDG mass of the particle in the new hypothesis (a pion or a proton). According to Equation 3.7, this changes the four momentum \mathbf{p} of the particle from

$$\mathbf{p}_{kaon} = (E_{kaon}, \vec{p}) = (\sqrt{m_{PDG,kaon}^2 + \vec{p}^2}, \vec{p}), \quad (7.1)$$

to

Parameter	$B^0/B_s^0 \rightarrow \phi\pi^+\pi^-$	$\Lambda_b^0 \rightarrow \phi K^- p$	$B^0/B_s^0 \rightarrow \phi K^*(892)$
Gaussian σ [MeV/c^2]	53.7 ± 4.9	78.4 ± 4.9	60.1 ± 5.6
CB σ [MeV/c^2]	21.53 ± 0.42	36.8 ± 5.9	24.59 ± 0.40
CB to Gauss fraction f	0.97 ± 0.01	0.77 ± 0.08	0.97 ± 0.01
CB α	0.218 ± 0.007	-0.189 ± 0.055	0.375 ± 0.009
mean [MeV/c^2]	5245.45 ± 0.55	5544.9 ± 3.4	5295.81 ± 0.52

Table 7.1.: Results from the fit to the simulated $B_s^0 \rightarrow \phi\phi$ sample under the $\phi\pi^+\pi^-$, $\phi K^- p$ and $\phi K^*(892)$ hypothesis, which is used to determine the reflection shape of the wrongly reconstructed $B_s^0 \rightarrow \phi\phi$ events under the respective new hypothesis. The fits are shown in the respective chapter.

$$\mathbf{p}_{pion/proton} = (E_{pion/proton}, \vec{p}) = (\sqrt{m_{PDG,pion/proton}^2 + \vec{p}^2}, \vec{p}). \quad (7.2)$$

Since the mass is directly related to the four momentum via $\mathbf{p}^2 = E^2 - \vec{p}^2 = m^2$, the invariant mass distributions change. To determine possible physical backgrounds, the new invariant mass distributions are examined for ascertained signal peaks at the known masses of the B^0 , B_s^0 , B^+ meson and the Λ_b^0 baryon. The resulting mass distributions consist of three components:

- Reconstructed peaking background events: The mass distribution is narrow and modeled with a Gaussian function.
- Real $B_s^0 \rightarrow \phi\phi$ signal events which are wrongly reconstructed under the new particle hypothesis: This is the major contribution with a broad reflection shape. The mass distribution is modeled by a Crystal Ball together with a Gaussian function. The mean is shared between both functions.
- Combinatorial background: The mass distribution is described by an exponential function.

The yield of the Gaussian peak gives an estimate for the contribution of Λ_b^0 , B^\pm , B^0 or B_s^0 decays to the peaking background in $B_s^0 \rightarrow \phi\phi$.

The shape of the wrongly reconstructed $B_s^0 \rightarrow \phi\phi$ signal events is constrained by fits to a simulated $B_s^0 \rightarrow \phi\phi$ sample reconstructed under the respective particle hypothesis. The fit results for this simulated samples with the exception of $B^+ \rightarrow \phi K^+$ are shown in Table 7.1.

7.1. $B^+ \rightarrow \phi K^+$

To investigate the contribution of $B^+ \rightarrow \phi K^+$ decays, any three of the four final state kaons of the selected $B_s^0 \rightarrow \phi\phi$ candidates with the highest invariant mass were reconstructed to form the B^\pm meson. Figure 7.1 shows the invariant three-kaon mass

distribution of the selected $B_s^0 \rightarrow \phi\phi$ candidates for data and simulation. It can be observed that no events peak near the PDG B^\pm mass of $m_{B^\pm} = 5279 \text{ MeV}/c^2$. Thus, the contribution from $B^+ \rightarrow \phi K^+$ decays with an additional random kaon in the selected $B_s^0 \rightarrow \phi\phi$ candidates is negligible.

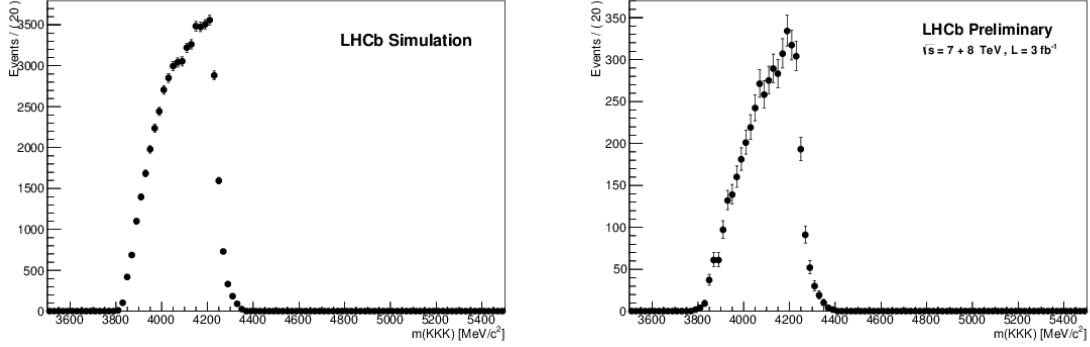


Figure 7.1.: $B_s^0 \rightarrow \phi\phi$ candidates from (left) simulation and (right) data reconstructed as $B^+ \rightarrow \phi K^+$ by choosing the three kaons with the highest invariant mass and ignoring one kaon.

7.2. $B^0/B_s^0 \rightarrow \phi\pi^+\pi^-$

In order to investigate the contribution of $B^0/B_s^0 \rightarrow \phi\pi^+\pi^-$ decays in the selected signal decays, the kaon pair with an invariant mass furthest away from the PDG ϕ meson mass is assigned the pion hypothesis. A double Gaussian is used to model the potential mass peaks of the $B^0/B_s^0 \rightarrow \phi\pi^+\pi^-$ contributions. The shape of the double Gaussian which model the B^0 peak is constrained using a simulated sample of $B^0 \rightarrow \phi\pi\pi$ decays. The wrongly reconstructed $\phi\phi$ signal shape described by the Gaussian and the Crystal Ball function is obtained by a fit to the simulated $B_s^0 \rightarrow \phi\phi$ sample which is reconstructed under the $\phi\pi^+\pi^-$ hypothesis (see Table 7.1). The left-hand side of Figure 7.2 shows this fit.

Since all the shapes are fixed, the normalization of the potential $B^0/B_s^0 \rightarrow \phi\pi^+\pi^-$ contribution is the only free parameter left. The fit yields values compatible with zero. The right-hand side of Figure 7.2 shows that the present background in the data sample can be described by an exponential function which accounts for combinatorial background. There is no peak visible at the known B^0 and B_s^0 masses.

7.3. $\Lambda_b^0 \rightarrow \phi K^- p$

The contribution of $\Lambda_b^0 \rightarrow \phi K^- p$ to the peaking background is investigated by choosing the K^+ candidate of the kaon pair with the invariant mass furthest away from the

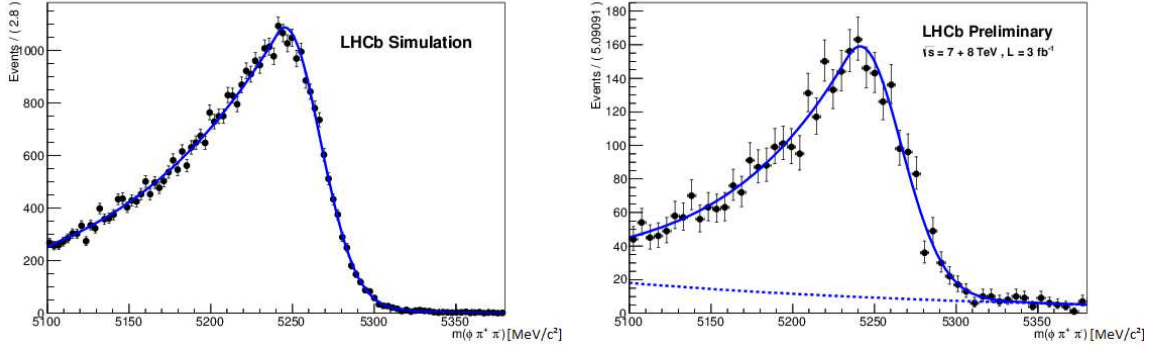


Figure 7.2.: Invariant mass distribution of simulated (left) $B_s^0 \rightarrow \phi\phi$ events and (right) the selected $B_s^0 \rightarrow \phi\phi$ data reconstructed as $\phi\pi\pi$, described by a Crystal Ball together with a Gaussian and an exponential function. The combinatorial background is well described by the exponential function (dashed blue line) with no further contribution from peaking $\phi\pi^+\pi^-$ events.

nominal ϕ mass to be the proton. To decide which kaon is reconstructed as a proton, the neural network particle identification variable¹ is used. The kaon candidate for which the probability of being a proton compared to the probability of being a kaon is the largest (i.e. $\Delta = \ln(\text{ProbNNp}) - \ln(\text{ProbNNk})$ is the largest) is assigned the proton hypothesis. In the top right (2011 data) and bottom left (2012 data) of Figure 7.3 peaks are visible at the nominal Λ_b^0 mass of $m_{\Lambda_b^0} = 5619.4 \text{ MeV}/c^2$.

To model the $\phi K^- p$ contribution, a Gaussian is used with the mean fixed to the nominal Λ_b^0 mass, while the combinatorial background is modeled with an exponential and the $B_s^0 \rightarrow \phi\phi$ signal by a Gaussian and a Crystal Ball. Fitting the 2011 and 2012 data sets separately yields event numbers of 49 ± 20 and 65 ± 30 respectively. The fit to the combined 2011 and 2012 data gives a yield of $N_{\Lambda_b^0} = 114 \pm 36$ events in the $B_s^0 \rightarrow \phi\phi$ sample.

If a cut on the proton probability of the kaon reconstructed under the proton hypothesis ($\text{ProbNNp} > 0.4$) is applied, most of the $B_s^0 \rightarrow \phi\phi$ signal events are removed and the resulting Λ_b^0 peak is visible in the invariant mass spectrum. This distribution is fitted with a Gaussian for the Λ_b^0 peak and a flat line accounting for the remaining background. The fit returns $N_{\Lambda_b^0} = 107 \pm 14$ events, which is compatible with the previous result and validates the applied procedure used to investigate the $\Lambda_b^0 \rightarrow \phi K^- p$ contribution. Figure 7.3 shows the fit to the simulated $B_s^0 \rightarrow \phi\phi$ sample reconstructed under the $\Lambda_b^0 \rightarrow \phi K^- p$ hypothesis as well as the fits to the 2011 and 2012 data samples and the fit to the combined data with the $\text{ProbNNp} > 0.4$ cut applied.

¹The ProbNNp and ProbNNk variables are used to chose which kaon is reconstructed as a proton.

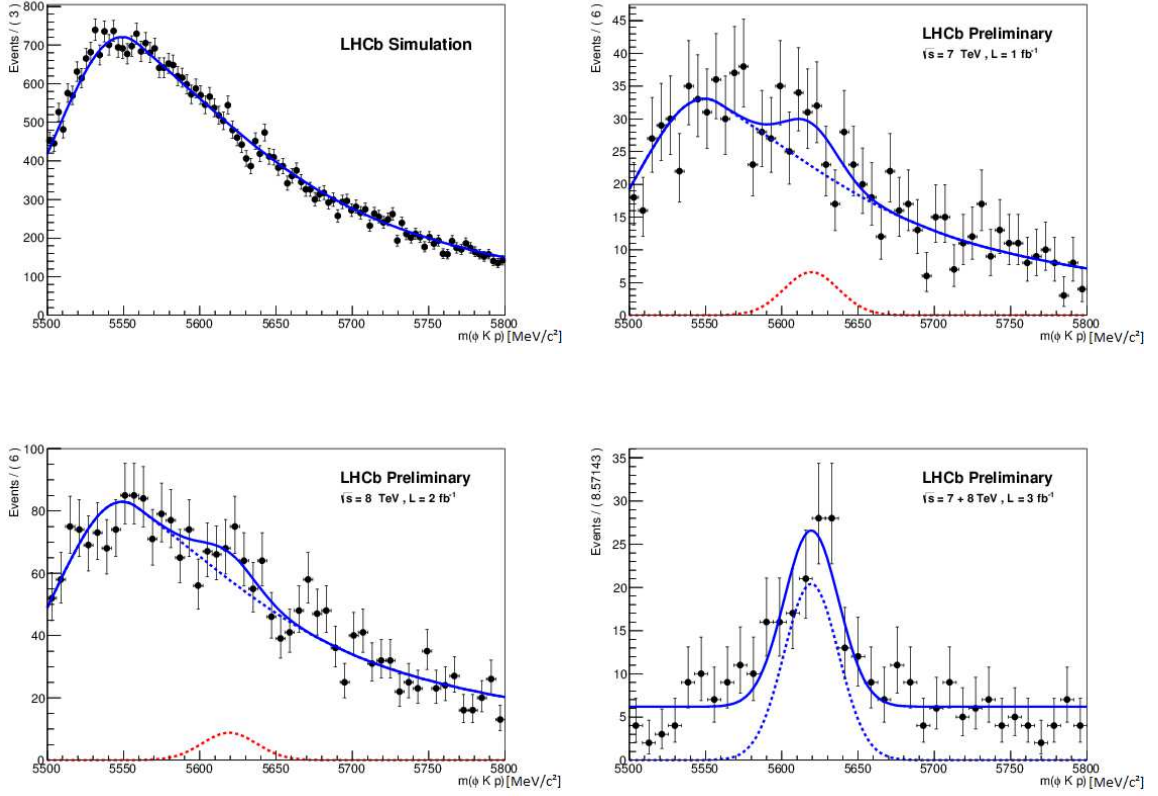


Figure 7.3.: Invariant mass distribution of selected $\phi\phi$ candidates reconstructed under the $\Lambda_b^0 \rightarrow \phi K^- p$ hypothesis. The distribution is described by a Crystal Ball and a Gaussian function together with an exponential function. The Figure shows (top left) Simulation, (top right) 2011 data, (bottom left) 2012 data and (bottom right) combined data set with ProbNNp cut applied. For the 2011 and 2012 data the Gaussian of the possible Λ_b contribution is depicted with a dashed red line.

7.4. $B^0/B_s^0 \rightarrow \phi K^*(892)$

To investigate the contribution of $B^0/B_s^0 \rightarrow \phi K^*(892)$ decays in the selected $B_s^0 \rightarrow \phi\phi$ candidates, the kaon candidate with the smallest kaon likelihood is assigned the pion hypothesis. The possible $B^0 \rightarrow \phi K^*(892)$ contribution is modeled using a Gaussian function. The shape is determined from a fit to the combined 2011 and 2012 mass distribution of $B^0 \rightarrow \phi K^*(892)$ decays. This data set is selected similarly to the $B_s^0 \rightarrow \phi\phi$ sample used in this analysis, with the exception of the usage of the pion probability² to select the final state pion. An exponential is added to account for combinatorial

²The ProbNNpi variable is used.

Parameter	fitted value
N_{sig}	6972 ± 141
N_{bg}	5156 ± 134
$\sigma_1 [MeV/c^2]$	13.10 ± 0.94
$\sigma_2 [MeV/c^2]$	23.4 ± 3.4
f	0.63 ± 0.14
α	0.00061 ± 0.00015
mean $[MeV/c^2]$	5278.58 ± 0.25

Table 7.2.: Fitted parameters from the fit to the $B^0 \rightarrow \phi K^*(892)$ sample with the $B_s^0 \rightarrow \phi\phi$ selection applied.

background. The fit results from the fit to the combined 2011 and 2012 mass distribution of $B^0 \rightarrow \phi K^*(892)$ decays are summarized in Table 7.2 and shown in Figure 7.4 (left).

When the invariant mass distribution of $B_s^0 \rightarrow \phi\phi$ candidates reconstructed under the $\phi K^*(892)$ hypothesis is fitted to extract the yield of the possible $B^0 \rightarrow \phi K^*(892)$ contribution to peaking background in the selected signal sample, the fit does not converge due to the low statistics of this contribution. Since nevertheless a small number of $B^0 \rightarrow \phi K^*(892)$ events are expected to pollute the selected $B_s^0 \rightarrow \phi\phi$ sample, a different method has to be used to extract the $\phi K^*(892)$ yield.

The yield is estimated by applying the $\phi\phi$ and the $\phi K^*(892)$ event selection to the $B^0 \rightarrow \phi K^*(892)$ sample of simulated events assuming the equality of the ratios

$$\frac{\#selected(\text{Data } \phi K^* \text{ in } \phi\phi)}{\#selected(\text{Data } \phi K^* \text{ in } \phi K^*)} = \frac{\#selected(\text{Sim } \phi K^* \text{ in } \phi\phi)}{\#selected(\text{Sim } \phi K^* \text{ in } \phi K^*)}, \quad (7.3)$$

where:

- $\#selected(\text{Data } \phi K^* \text{ in } \phi\phi)$ is the number of $B^0 \rightarrow \phi K^*(892)$ decays in the $\phi\phi$ data sample.
- $\#selected(\text{Data } \phi K^* \text{ in } \phi K^*)$ is the number of $B^0 \rightarrow \phi K^*(892)$ decays in the $\phi K^*(892)$ data sample.
- $\#selected(\text{Sim } \phi K^* \text{ in } \phi\phi)$ is the number of $B^0 \rightarrow \phi K^*(892)$ decays in the $\phi\phi$ simulation.
- $\#selected(\text{Sim } \phi K^* \text{ in } \phi K^*)$ is the number of $B^0 \rightarrow \phi K^*(892)$ decays in the $\phi K^*(892)$ simulation.

This assumption is justified, because the selection process for both modes is mainly based on kinematical variables, which are well described by the simulation. Equation 7.3 can be used to determine the expected number of $B^0 \rightarrow \phi K^*(892)$ decays contributing to

the selected $B_s^0 \rightarrow \phi\phi$ candidates:

$$\#selected(Data \phi K^* \text{ in } \phi\phi) = \frac{\#selected(Sim \phi K^* \text{ in } \phi\phi)}{\#selected(Sim \phi K^* \text{ in } \phi K^*)} \cdot \#selected(Data \phi K^* \text{ in } \phi K^*). \quad (7.4)$$

The ratio of events found in the the ϕK^* simulation with $\phi\phi$ and ϕK^* selection is taken from [3]. The yields are:

$$\begin{aligned} \#selected(Sim \phi K^* \text{ in } \phi\phi) &= 1070 \pm 40, \\ \#selected(Sim \phi K^* \text{ in } \phi K^*) &= 96606 \pm 465. \end{aligned}$$

The number of events in the combined 2011 and 2012 ϕK^* data sample is taken from the fit also used to determine the shape of the B^0 peak shown on the left hand side of Figure 7.4. This fit yields:

$$\#selected(Data \phi K^* \text{ in } \phi K^*) = 6972 \pm 141.$$

Inserting these results in Equation 7.4 gives an expected yield of 38 ± 2 events of $B^0 \rightarrow \phi K^*(892)$ decays contributing to the selected $B_s^0 \rightarrow \phi\phi$ candidates.

Once the number of expected B^0 events is known, the $B_s^0 \rightarrow \phi K^*(892)$ contribution can be calculated with the fragmentation fraction $\frac{f_s}{f_d}$ and the fraction of branching ratios:

$$\#selected(B_s^0 \rightarrow \phi K^*(892)) = \#selected(B^0 \rightarrow \phi K^*(892)) \cdot \frac{f_s}{f_d} \cdot \frac{\text{BR}(B^0 \rightarrow \phi K^*)}{\text{BR}(B_s^0 \rightarrow \phi K^*)}. \quad (7.5)$$

Evaluating Equation 7.5 with input values taken from [36] yields approximately one expected $B_s^0 \rightarrow \phi K^*(892)$ event. This contribution is therefore neglected.

The 2011 and 2012 $B_s^0 \rightarrow \phi\phi$ data set reconstructed under the ϕK^* hypothesis is combined to ensure the visibility of the $B^0 \rightarrow \phi K^*(892)$ contribution. The invariant mass distribution of the combined sample is fitted with the shape of the Gaussian B^0 peak fixed to the values from Table 7.2 and the yield fixed to the 38 events. The fit result is shown on the right hand side of Figure 7.4. Repeating the procedure described in this section for the 2011 and 2012 data samples and simulations separately yields 12 ± 0.6 and 27 ± 1.1 $B^0 \rightarrow \phi K^*(892)$ decays, respectively.

7.5. Summary and $B_s^0 \rightarrow \phi\phi$ mass fit

Of the four decay modes investigated in the previous sections, only the $\Lambda_b^0 \rightarrow \phi K^- p$ and the $B^0 \rightarrow \phi K^*(892)$ channel were found to contribute to peaking backgrounds among the selected $B_s^0 \rightarrow \phi\phi$ candidates. The shapes and yields of the peaking background components are modeled with a Crystal Ball function for each of the two contributions, which is fixed to the values determined in Section 7.3 and 7.4 respectively. They are combined with an exponential function accounting for combinatorial background and a double Gaussian modeling the $B_s^0 \rightarrow \phi\phi$ signal peak. Figure 7.5 shows the fits to the

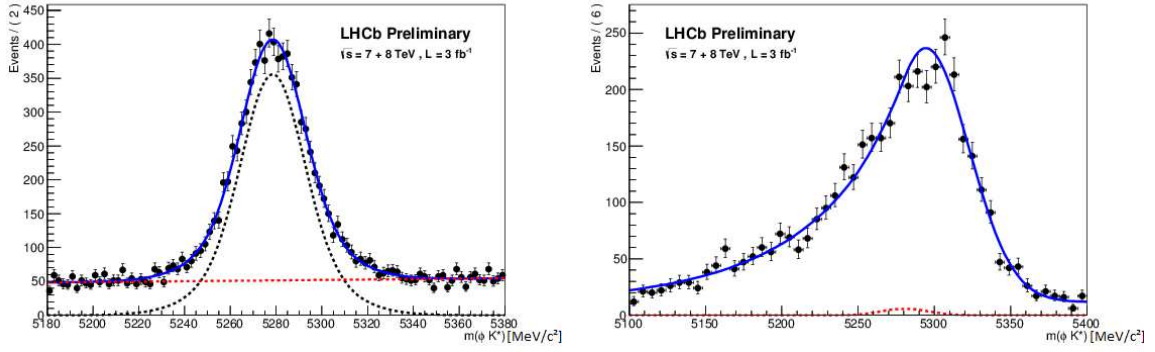


Figure 7.4.: Invariant mass distribution (left) of the combined 2011 and 2012 data sample of selected $B^0 \rightarrow \phi K^*(892)$ candidates, described by a double Gaussian and an exponential function to determine the B^0 peak shape. The invariant mass distribution (right) of the combined $B_s^0 \rightarrow \phi\phi$ candidates reconstructed under the ϕK^* hypothesis is described by a Crystal Ball and a Gaussian function together with a Gaussian function for the $B^0 \rightarrow \phi K^*(892)$ peak and an exponential function for the combinatorial background. The B^0 peak is visualized by the dashed red line.

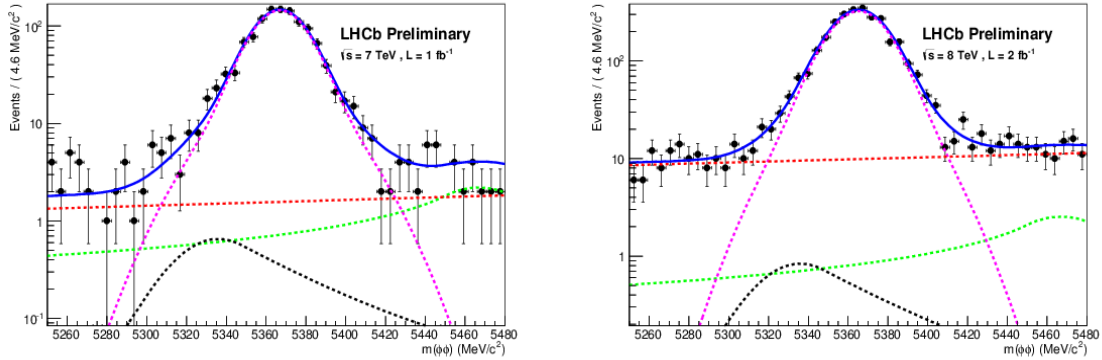


Figure 7.5.: Invariant four-kaon mass distribution of the selected $B_s^0 \rightarrow \phi\phi$ candidates for (left) 2011 and (right) 2012 data. The fit to describe the data has the following components: Two Crystal Ball functions to model the contribution of ϕK^* (black) and ϕKp (green), both dashed; the Gaussian signal peak (magenta) to describe the $B_s^0 \rightarrow \phi\phi$ signal candidates and the exponential function to describe combinatorial background (red), both dashed.

invariant mass distributions of the selected $B_s^0 \rightarrow \phi\phi$ candidates from 2011 and 2012 data. The fits yield 1158 ± 38 and 2713 ± 60 signal candidates for the years 2011 and

2012, respectively. A fit to the combined data set yields 3896 ± 72 signal candidates for the full 3 fb^{-1} of integrated luminosity.

The peaking background components are also included in the background PDF for the fit to the B_s^0 mass distributions which is used to extract the triple product asymmetries. Further details on how the simultaneous maximum likelihood fit is implemented are given in Chapter 10.

Determination of decay-time acceptance correction

The selection cuts and trigger requirements imposed during the selection process described in Chapter 5 introduce a decay-time dependent acceptance which is defined to be the ratio of the number of selected B_s^0 to the total number of produced B_s^0 :

$$\epsilon(t) = \frac{\#\text{selected } B_s^0 \rightarrow \phi\phi(t)}{\#\text{produced } B_s^0 \rightarrow \phi\phi(t)}. \quad (8.1)$$

The exact determination of the decay-time-dependent acceptance is necessary, because the acceptance is observed to introduce a small shift of the values for the triple product asymmetries A_U and A_V [37]. Although the presented measurement is time-integrated, the decay-time acceptance $\epsilon(t)$ in the time-dependent decay rate $d\Gamma(t, \theta_1, \theta_2, \Phi)$ of $B_s^0 \rightarrow \phi\phi$ decays can introduce an effect on the triple product asymmetries, when integrating over t . The determined decay-time acceptance can be used to estimate the systematic uncertainty on the triple product asymmetries, which is introduced by ignoring decay-time acceptance effects.

The results of this chapter are an important input for the time-dependent measurement of CP violation [3], in which the exact knowledge of the time acceptance correction is essential.

The cut that mainly introduces the decay-time-dependent acceptance is the Impact Parameter (IP) cut [38], which requires the secondary vertex to be displaced by some margin from the primary vertex. As a consequence, events with short B_s^0 decay-times, where the B_s^0 decays close to the primary vertex, are rejected. This results in an efficiency drop for low decay-times. In addition, it is known that the efficiency for large lifetimes drops linearly which is an effect introduced by the VELO track reconstruction algorithms [39]. Those algorithms suffer from a drop in reconstruction efficiency for B_s^0 candidates that are displaced by a few centimeters from the z-axis. The efficiency loss increases with the displacement and thus also with the decay-time of the B_s^0 candidate. In this analysis, the $B_s^0 \rightarrow \phi\phi$ decay-time acceptance is determined on data using $B_s^0 \rightarrow D_s^+ \pi^-$ decays as a control channel, avoiding the dependence on simulation which introduces large uncertainties. This channel is chosen because of the higher statistics due to a higher branching fraction with respect to $B_s^0 \rightarrow \phi\phi$ decays and the precisely measured lifetime of the B_s^0 meson in the $B_s^0 \rightarrow D_s^+ \pi^-$ channel [40]. Since the D meson

further decays into two kaons and a pion $D_s^+ \rightarrow K^+K^-\pi^+$, the decay is topologically similar to the $B_s^0 \rightarrow \phi\phi$ decay, assuming that the D_s^+ does not fly far. To ensure this, a decay-time cut of 1 ps is applied to the D_s^+ meson. To investigate the dependence on the ways in which an event has been triggered, the decay-time efficiency is determined for the four trigger possibilities separately. These are:

- The L0 hadron trigger and the HLT2 ϕ trigger are both issued (L0Hadron TOS (**HTOS**) and Hlt2IncPhi TOS (**IP TOS**)).
- The L0 hadron trigger and the HLT2 topological trigger are issued, but the ϕ trigger is not issued (L0Hadron TOS and Hlt2IncPhi non-TOS (**IPnTOS**)).
- The L0 hadron trigger is not issued, but any other L0 trigger and the HLT2 ϕ trigger are issued (L0Hadron non-TOS (**HnTOS**) and Hlt2IncPhi TOS).
- The L0 hadron trigger and the HLT2 ϕ trigger are not issued, but any other L0 trigger and the topological trigger are issued (L0Hadron non-TOS and Hlt2IncPhi non-TOS).

The steps necessary to extract the decay-time efficiency are summarized in the following sections. For each of the four trigger possibilities, an acceptance histogram is generated. This is done by using $B_s^0 \rightarrow D_s^+\pi^-$ data to determine the decay-time distributions that suffer from acceptance effects and dividing them by the theoretical prediction. The results are binned and filled into histograms. These histograms show the decay-time acceptance as a function of the decay-time, where the acceptance is equal to 1 for decay-times where no acceptance effect is observed and unequal to 1 otherwise. The decay-time acceptance histograms are used in Chapter 11 to estimate the systematic uncertainty on the triple product asymmetries A_U and A_V and in the time-dependent analysis of CP violation [3].

8.1. Selection of $B_s^0 \rightarrow D_s^+\pi^-$ candidates

In order to match the decay topology of $B_s^0 \rightarrow D_s^+\pi^-$ and $B_s^0 \rightarrow \phi\phi$ events, the whole selection is kept as close as possible to the one used to select the $B_s^0 \rightarrow \phi\phi$ signal candidates. The multivariate analysis used to select these signal candidates includes the neural network PID variable for kaons. Since there are also pions present in the final state of the $B_s^0 \rightarrow D_s^+\pi^-$ decay, the usage of the exact same boosted decision tree would lead to a low efficiency. Therefore, a second BDT is trained using all variables mentioned in Section 5.3 with the exception of the ProbNNk variable. The second decision tree, in the following noted by BDT2, is trained using the same $B_s^0 \rightarrow \phi\phi$ sideband data as background input and the same simulated signal events as already used for the first BDT. The obtained results for signal purity, the figure of merit ($S/\sqrt{S+B}$) and the optimal cut values for 2011 and 2012 data are in good agreement with the nominal BDT results.

Additional selections have to be applied to remove physical background from the $B_s^0 \rightarrow D_s^+ \pi^-$ data sample and ensure high signal purity. The decays $\Lambda_b \rightarrow \Lambda_c^- (\rightarrow p K^- \pi^-) \pi^+$ and $B^0 \rightarrow D^+ (\rightarrow \pi^- K^+ \pi^+) \pi^-$ are expected to pollute the selected events [3]. This is confirmed by assigning a kaon candidate of the $B_s^0 \rightarrow D_s^+ \pi^-$ candidates to be a proton (for Λ_b) or assigning the pion hypothesis to a kaon candidate (for B^0). The resulting invariant mass of the $p K^- \pi^-$ and the $\pi^- K^+ \pi^+$ candidates of selected $B_s^0 \rightarrow D_s^+ \pi^-$ decays is shown in Figure 8.1. A clear peak can be observed around the known Λ_c^- and D^+ masses. To remove these background components, a mass window of $20 \text{ MeV}/c^2$ around the nominal masses of these particles is vetoed.

To further improve the similarity between the $B_s^0 \rightarrow \phi \phi$ and $B_s^0 \rightarrow D_s^+ \pi^-$ decay modes, a cut on the invariant mass of the $K^+ K^-$ systems of $15 \text{ MeV}/c^2$ around the ϕ mesons mass is applied. After this cut mainly $D_s^+ \rightarrow \phi \pi^+$ events are left contributing to the $B_s^0 \rightarrow D_s^+ \pi^-$ decay.

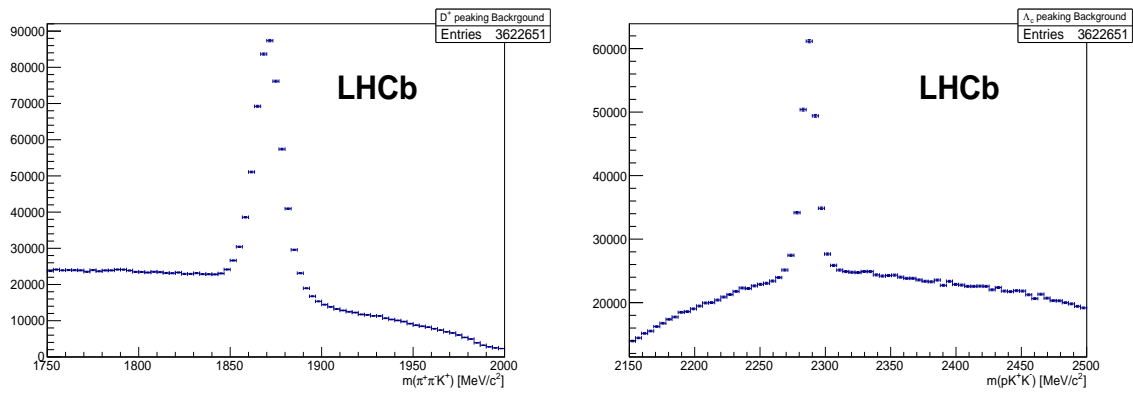


Figure 8.1.: Peaking background contribution to the 2012 $B_s^0 \rightarrow D_s^+ \pi^-$ candidates reconstructed as (left) $B^0 \rightarrow D^+ \pi^-$ and (right) $\Lambda_b \rightarrow \Lambda_c^- \pi^+$ from data. The D^+ contribution is revealed by the invariant mass distribution of the (left) $K^+ \pi^- \pi^+$ candidates and the Λ_c^- contribution is visible in the invariant mass distribution of the (right) $p K^- \pi^+$ candidates.

In the final step, the selection cuts of the $B_s^0 \rightarrow \phi \phi$ selection that cause the time-dependent acceptance are applied to the $B_s^0 \rightarrow D_s^+ \pi^-$ data including the cut on the IP- χ^2 and the cut on the transverse momentum of each final state particle. The selection cuts that are different from the $B_s^0 \rightarrow \phi \phi$ selection are summarized in Table 8.1.

8.2. Comparison of simulated $B_s^0 \rightarrow D_s^+ \pi^-$ and $B_s^0 \rightarrow \phi \phi$ time acceptance

To justify the usage of the $B_s^0 \rightarrow D_s^+ \pi^-$ mode as a control channel for the decay-time acceptance a good agreement between $B_s^0 \rightarrow \phi \phi$ and $B_s^0 \rightarrow D_s^+ \pi^-$ events is crucial. The

Variable	Cut Value
D_s^0 decay-time	$< 1ps$
ϕ meson enforcement $ m_{K^+K^-} - 1019.455 MeV/c^2 $	$< 15.0 MeV/c^2$
D^\pm veto $ m_{\pi^\pm K^\mp \pi^\pm} - 1869.6 MeV/c^2 $	$> 20.0 MeV/c^2$
Λ_c veto $ m_{pK^-\pi^-} - 2286.5 MeV/c^2 $	$> 20.0 MeV/c^2$
D_s^+ range $m_{K^+K^-\pi^+}$	$1908 MeV/c^2 < m_{D_s^+} < 2028 MeV/c^2$
B_s^0 range $m_{K^+K^-\pi^+\pi^-}$	$5250 MeV/c^2 < m_{B_s^0} < 5567 MeV/c^2$

Table 8.1.: Selection cuts to select $B_s^0 \rightarrow D_s^+ \pi^-$ candidates that are different from the $\phi\phi$ selection.

largest source of systematic uncertainty is the difference between simulated $B_s^0 \rightarrow D_s^+ \pi^-$ and $B_s^0 \rightarrow \phi\phi$ events in the kinematic observables. Disagreement in the kinematic observables leads to a different response to the selection steps which introduce the decay-time dependent acceptance. Here, a difference between the normalized distribution of the minimum track p_t between simulated $B_s^0 \rightarrow \phi\phi$ and $B_s^0 \rightarrow D_s^+ \pi^-$ events can be observed, which is shown in Figure 8.2. The $B_s^0 \rightarrow D_s^+ \pi^-$ events are therefore re-weighted according to this observable.

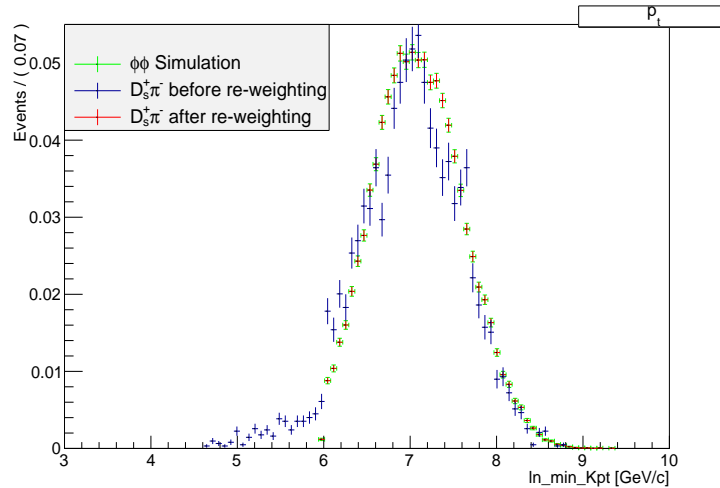


Figure 8.2.: Comparison between the minimum track p_t distributions of simulated $B_s^0 \rightarrow \phi\phi$ events shown in green, $B_s^0 \rightarrow D_s^+ \pi^-$ events before the re-weighting of events shown in blue and in red after. After the re-weighting good agreement is seen.

8.3. Data driven selection of $B_s^0 \rightarrow D_s^+ \pi^-$ signal candidates

In order to obtain the decay-time distribution of $B_s^0 \rightarrow D_s^+ \pi^-$ signal events, the background contributions have to be suppressed. This is done using a weighting technique known as s-weights [41]. The weights are obtained from a fit to the two-dimensional mass distribution of the B_s^0 and D_s^+ candidates, separating signal and background. It should be noted, that the $B_s^0 \rightarrow D_s^+ \pi^-$ data sample is still polluted by mis-reconstructed background from the decay $B_s^0 \rightarrow D_s^{*+} \pi^- \rightarrow D_s^+ \gamma \pi^-$. This background is therefore parametrized by the fit function to describe the invariant mass distributions of the selected candidates. The fit function has the form

$$\mathcal{P}(m_{B_s^0}, m_{D_s^+}; \vec{\lambda}_i) = N_{sig} \cdot S(m_{B_s^0}, m_{D_s^+}; \vec{\lambda}_{sig}) + N_{comb} \cdot B_{comb}(m_{B_s^0}, m_{D_s^+}; \vec{\lambda}_{comb}) + N_{mis-reco} \cdot B_{mis-reco}(m_{B_s^0}, m_{D_s^+}; \vec{\lambda}_{mis-reco}), \quad (8.2)$$

where the three fit components are:

- $S(m_{B_s^0}, m_{D_s^+}; \vec{\lambda}_{sig})$ is the signal PDF. The D_s^+ mass peak is modeled by a double Gaussian and the B_s^0 mass peak is modeled by a double Gaussian and a Crystal Ball function.
- $B_{mis-reco}(m_{B_s^0}, m_{D_s^+}; \vec{\lambda}_{mis-reco})$ is the PDF that takes mis-reconstructed $B_s^0 \rightarrow D_s^{*+} \pi^-$ events into account. Since the reconstructed masses of D_s^{*+} and D_s^+ candidates are similar due to the unreconstructed photon, the D_s^{*+} peak is located directly under the D_s^+ peak in the invariant $K^+ K^- \pi^+$ mass distribution and in the lower sideband of the $K^+ K^- \pi^+ \pi^-$ mass distribution due to the photon which carries away momentum. It is therefore described by a double Gaussian for the $m_{D_s^+}$ distribution and an ARGUS function for the $m_{B_s^0}$ distribution. The ARGUS function describes the peak-like structure of the invariant mass distribution of D_s^{*+} candidates and combines it with the radiative tail due to the missing photon momentum. It is of the form [42]:

$$F_{Arg}(m; \mu, p, c) = m \left(1 - \left(\frac{m}{\mu} \right)^2 \right)^p \cdot \exp \left(c \left(1 - \left(\frac{m}{\mu} \right)^2 \right) \right), \quad (8.3)$$

where μ represents the cutoff at which the function drops to zero, c determines the curvature and p the power of the ARGUS function.

- $B_{comb}(m_{B_s^0}, m_{D_s^+}; \vec{\lambda}_{comb})$ takes the combinatorial background into account. It is modeled by a single exponential function for both mass distributions.

The parameters of the ARGUS function λ_j are constrained to values obtained by simulation. The parameters float within their their statistical uncertainties using Gaussian

constrains. This is done by adding additional terms to the logarithmic likelihood function \mathcal{L}

$$\ln \mathcal{L} = \sum_{i=1}^{N_{events}} \left(\ln \mathcal{P}(m_{B_s^0}, m_{D_s^+}; \vec{\lambda}) + \sum_{j=1}^3 \frac{(\lambda_j - \lambda_{j,measured})^2}{2\sigma_{j,measured}^2} \right), \quad (8.4)$$

where $\lambda_{j,measured}$ is the measured value of the respective parameter of the ARGUS function and $\sigma_{j,measured}$ is the experimental uncertainty. This method ensures that the parameters λ_j take the values of the simulation within their statistical uncertainties.

The two-dimensional invariant mass distribution of selected D_s^+ and B_s^0 candidates is shown in Figure 8.3. The radiative tail, caused by the mis-reconstructed $D_s^{*+} \rightarrow D_s^+ \gamma$ decays can be observed. The projections of the two-dimensional invariant mass distributions, as well as the projections of the fit results on the B_s^0 and D_s^+ mass are shown in Figure 8.4. The fitted parameters are given in Table 8.2.

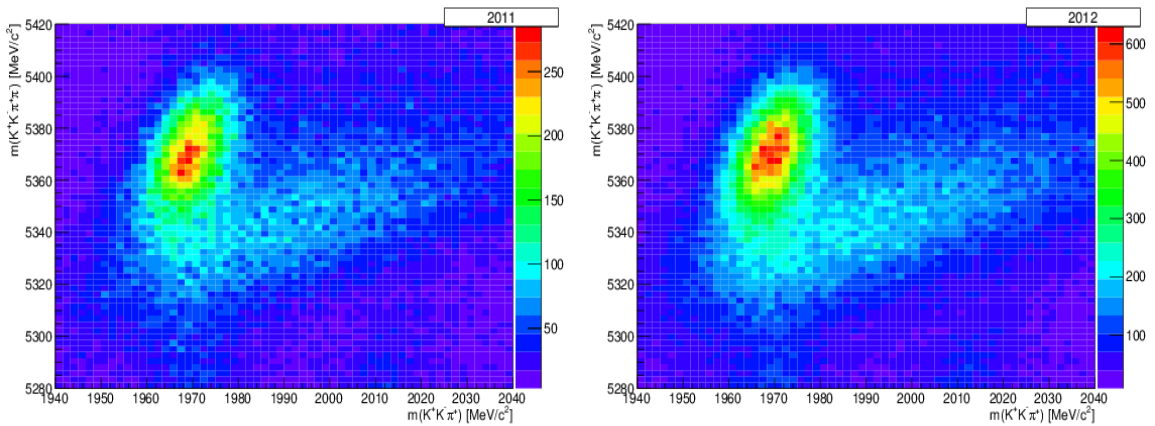


Figure 8.3.: Two-dimensional invariant mass distributions of the selected B_s^0 and D_s^+ candidates for (left) 2011 and (right) 2012 data. The radiative tail of mis-reconstructed $D_s^{*+} \rightarrow D_s^+ \gamma$ decays can be observed.

The two-dimensional PDF is used to assign a weight to each event. $B_s^0 \rightarrow D_s^+ \pi^-$ events, where either the invariant mass of the D_s^0 or the B_s^0 meson lies in the sideband of the distributions shown in Figure 8.4 are likely to be background and are therefore assigned a smaller weight compared to events where both invariant particle masses are close to the PDG value. A unique feature of the s-weight technique is that negative weights are allowed. This ensures that although some weights w_i are larger than 1, the sum of all weights N is $\sum_{i=1}^N w_i = N$. This means summing over all weighted events returns the initial, unweighted event yield, which preserves the normalization of the respective distribution. The fit allows to identify the background part modeled by $B_{comb}(m_{B_s^0}, m_{D_s^+}; \vec{\lambda}_{comb})$ and $B_{mis-reco}(m_{B_s^0}, m_{D_s^+}; \vec{\lambda}_{mis-reco})$ and separates it from the signal part modeled by $S(m_{B_s^0}, m_{D_s^+}; \vec{\lambda}_{sig})$. This is exploited to assign signal and background weights accordingly. The weights can be used to re-weight any given distribution to show either the distribution of signal or background events.

Parameter	fitted value 2011	fitted value 2012
N_{Sig}	13344 ± 272	30181 ± 372
N_{comb}	1888 ± 90	4281 ± 113
$N_{mis-reco}$	2237 ± 242	5414 ± 330
Bs σ_1 [MeV/c^2]	23.32 ± 1.16	13.88 ± 0.40
Bs σ_2 [MeV/c^2]	15.87 ± 0.31	19.75 ± 0.36
Bs f	0.88 ± 0.02	0.86 ± 0.01
CB α	-0.23 ± 0.03	-0.38 ± 0.02
CB σ [MeV/c^2]	51.98 ± 5.08	57.27 ± 3.28
ARG c	-267.58 ± 28.97	-211.560 ± 27.26
ARG μ [MeV/c^2]	5442 ± 12	5458 ± 12
ARG p	18.41 ± 2.31	16.32 ± 2.23
Ds σ_1 [MeV/c^2]	20.55 ± 3.02	24.69 ± 1.24
Ds σ_2 [MeV/c^2]	6.30 ± 0.11	6.29 ± 0.04
Ds f	0.09 ± 0.01	0.08 ± 0.01
α_{comb}	-0.0027 ± 0.0003	-0.0028 ± 0.0002
Bs \bar{m} [MeV/c^2]	5371.1 ± 0.2	5371.1 ± 0.1
Ds \bar{m} [MeV/c^2]	1969.61 ± 0.06	1969.53 ± 0.04

Table 8.2.: Parameters determined in a two-dimensional fit to the B_s^0 and D_s^+ mass distributions for 2011 and 2012 $B_s^0 \rightarrow D_s^+ \pi^-$ data.

8.4. Extraction of the decay-time acceptance correction

To determine the decay-time acceptance, the decay-time distribution of selected $B_s^0 \rightarrow D_s^+ \pi^-$ signal events is used. This distribution corresponds to the number of selected B_s^0 signal candidates in the numerator of Equation 8.1. The denominator is generated from the theoretical decay-time distribution without any selection cuts. The theory distribution is generated using an exponential decay function $e^{-\tau_{true} t}$ with the mean lifetime τ_{true} that is taken from the recent LHCb measurement [40]. Both distributions are normalized. For each of the four possible trigger categories defined at the beginning of this chapter a decay-time-dependent acceptance histogram is obtained. The acceptance histograms for 2011 and 2012 data are shown in Figures 8.5 and 8.6. The binning is chosen such that for lower decay-times, where most of the statistics is available, the bins are smaller. In all histograms one sees how the acceptance drops for very low decay-times and for very large decay-times. The effect for very large decay-times is less pronounced for 2012 data than for 2011 data. This effect is under investigation. It could originate from statistical fluctuations, because of the very low statistics at this high decay-times. The histograms are used to estimate the systematic uncertainty introduced by the decay-time acceptance on the triple product asymmetries A_U and A_V . Given that the statistical uncertainty dominates the measurement of triple product asymmetries in the $B_s^0 \rightarrow \phi \phi$ channel, the assignment of a systematical uncertainty is sufficient to account for the decay-time acceptance. The procedure is described in Chapter 11.

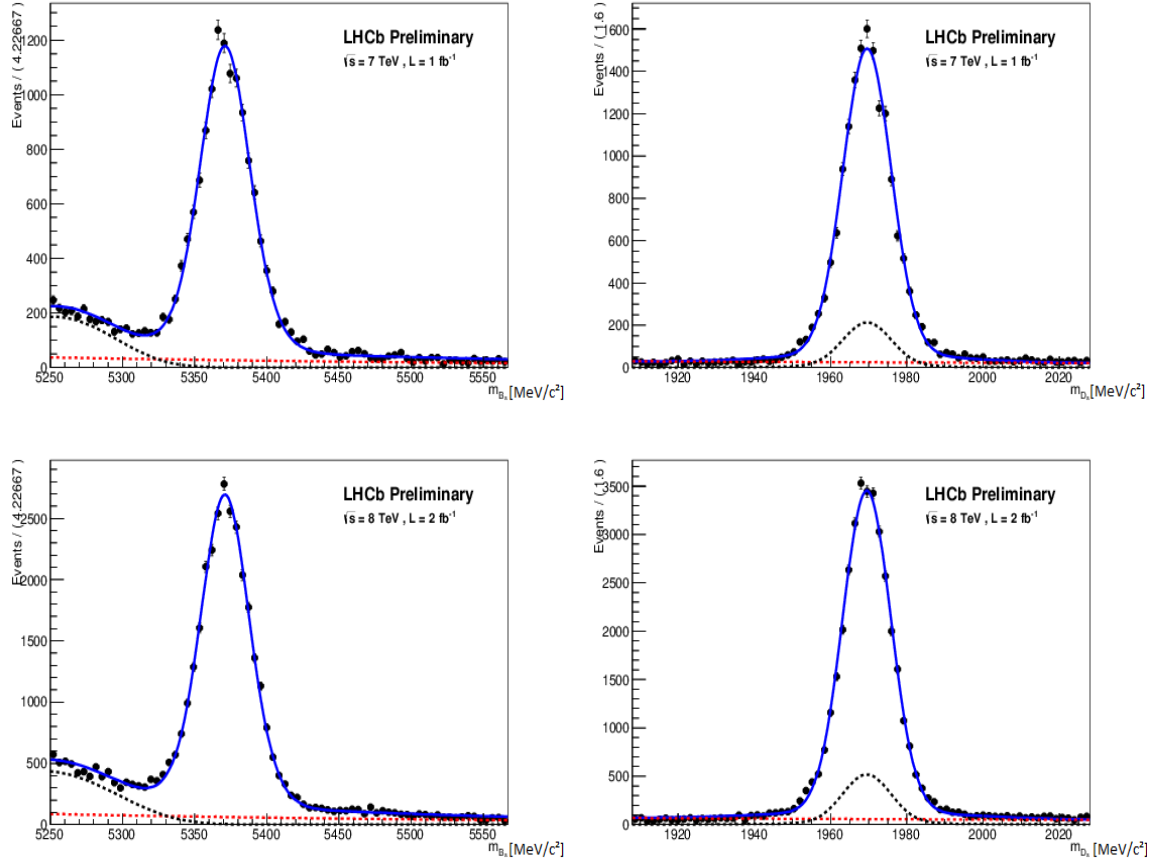


Figure 8.4.: Two-dimensional fit to the invariant $K^+K^-\pi^+\pi^-$ and $K^+K^-\pi^+$ mass distributions of selected $B_s^0 \rightarrow D_s^+\pi^-$ candidates for (top) 2011 data and (bottom) 2012 data. Peaking background components in black are modeled by an ARGUS function in the $m_{K^+K^-\pi^+\pi^-}$ distribution and a Gaussian in the $m_{K^+K^-\pi^+}$ distribution. Combinatorial background is modeled by an exponential in red. The signal is modeled with a double Gaussian ($m_{K^+K^-\pi^+}$) and a Gaussian together with a Crystal Ball ($m_{K^+K^-\pi^+\pi^-}$). The combined fit functions are shown in blue.

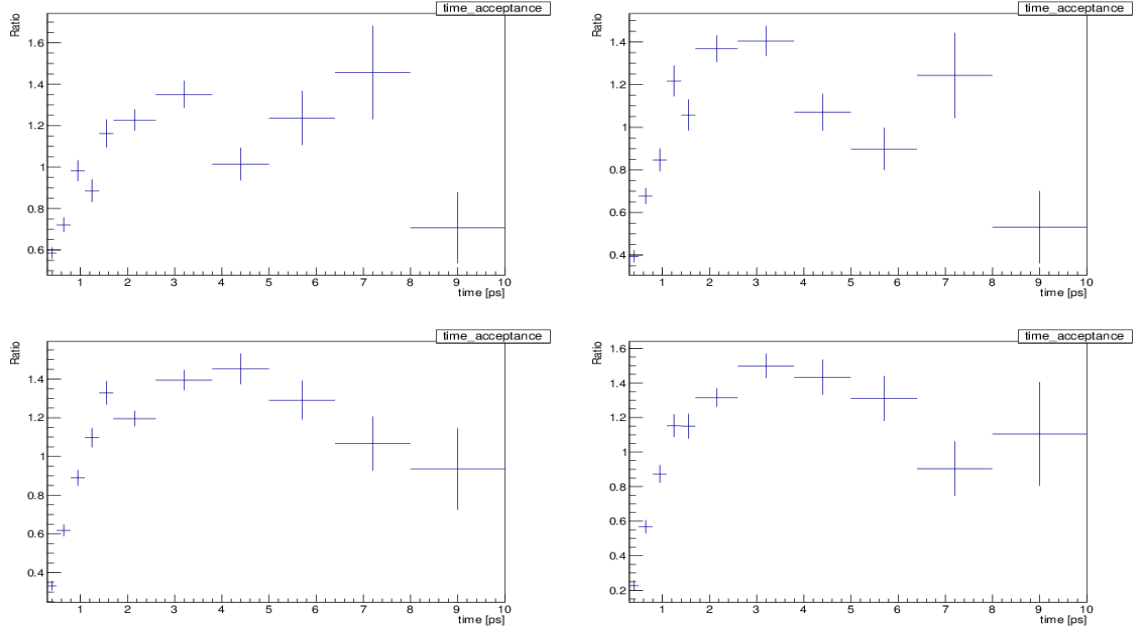


Figure 8.5.: decay-time acceptance distribution from 2011 $B_s^0 \rightarrow D_s^+ \pi^-$ data for events triggered as (top left) HTOS & IPNTOS, (top right) HnTOS & IPTOS, (bottom left) HTOS & IPnTOS or (bottom right) HnTOS & IPnTOS.

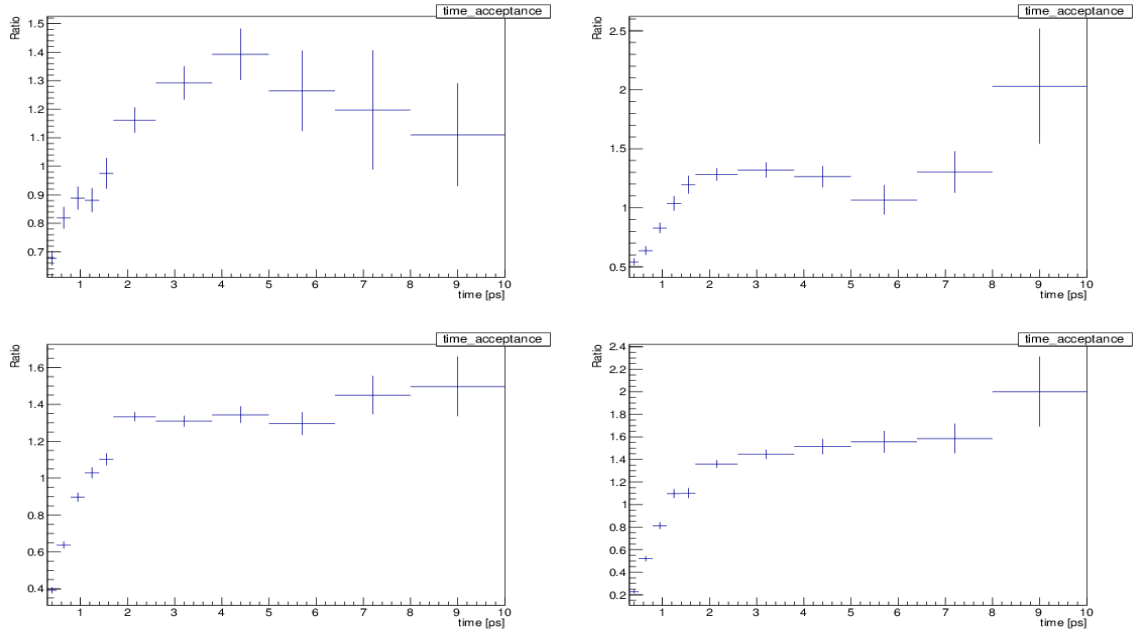


Figure 8.6.: decay-time acceptance distribution from 2012 $B_s^0 \rightarrow D_s^+ \pi^-$ data for events triggered as (top left) HTOS & IPNTOS, (top right) HnTOS & IPTOS, (bottom left) HTOS & IPnTOS or (bottom right) HnTOS & IPnTOS.

Determination of angular acceptance correction

The geometry of the LHCb detector and the requirements on the final state particle kinematics described in Section 5.2 introduce inefficiencies in dependence of the helicity angles θ_1 , θ_2 and Φ . The angular acceptance describes the efficiency of the particle detection and selection as a function of these angles. The angular acceptance is given by the ratio of selected and originally produced B_s^0 candidates

$$\epsilon(\Omega) = \frac{\#\text{selected } B_s^0 \rightarrow \phi\phi(\Omega)}{\#\text{produced } B_s^0 \rightarrow \phi\phi(\Omega)}, \quad (9.1)$$

where the number of B_s^0 decays are measured as a function of $\Omega = (\Phi, \theta_1, \theta_2)$, the helicity angle of the decays. Fully simulated $B_s^0 \rightarrow \phi\phi$ events are used to estimate the angular acceptance effects. The same selection criteria as described in Chapter 5 are applied to the simulated data set. Since the helicity angles are correlated, a three-dimensional correction has to be derived. Figure 9.1 shows the two dimensional correlation plots for the helicity angles used in the $B_s^0 \rightarrow \phi\phi$ decay where clear structures are observable.

To calculate the three-dimensional efficiency depending on Ω , the number of selected events in a given angular bin has to be compared to the number of events in this angular bin, that were produced in total. Since this number is not known for real data, a fully simulated data set is used. For the numerator in Equation 9.1, the simulated $B_s^0 \rightarrow \phi\phi$ events are used with the full signal selection applied to them. For the denominator, events without any detector or selection effects are generated according to the $B_s^0 \rightarrow \phi\phi$ decay rate defined in Equation 2.16. Since those events are not subject to detector effects and no further selection is applied, they correspond to the originally produced B_s^0 candidates relative to the simulated events, which are distorted by angular acceptance effects. The angular distributions of both simulated data sets are normalized to one and divided by each other to calculate the three-dimensional efficiency $\epsilon(\Omega)$. Figure 9.2 visualizes the one-dimensional projections of the relative acceptance for each angle. In the Φ dimension, only small effects can be observed while there is a clear drop in efficiency as $\cos\theta_{1/2}$ approaches ± 1 . This effect is introduced by the p_t cuts on final state kaons and the trigger selection.

A way to apply the angular acceptance correction within the maximum likelihood fit is described in the following. Using the definition of the likelihood function given in

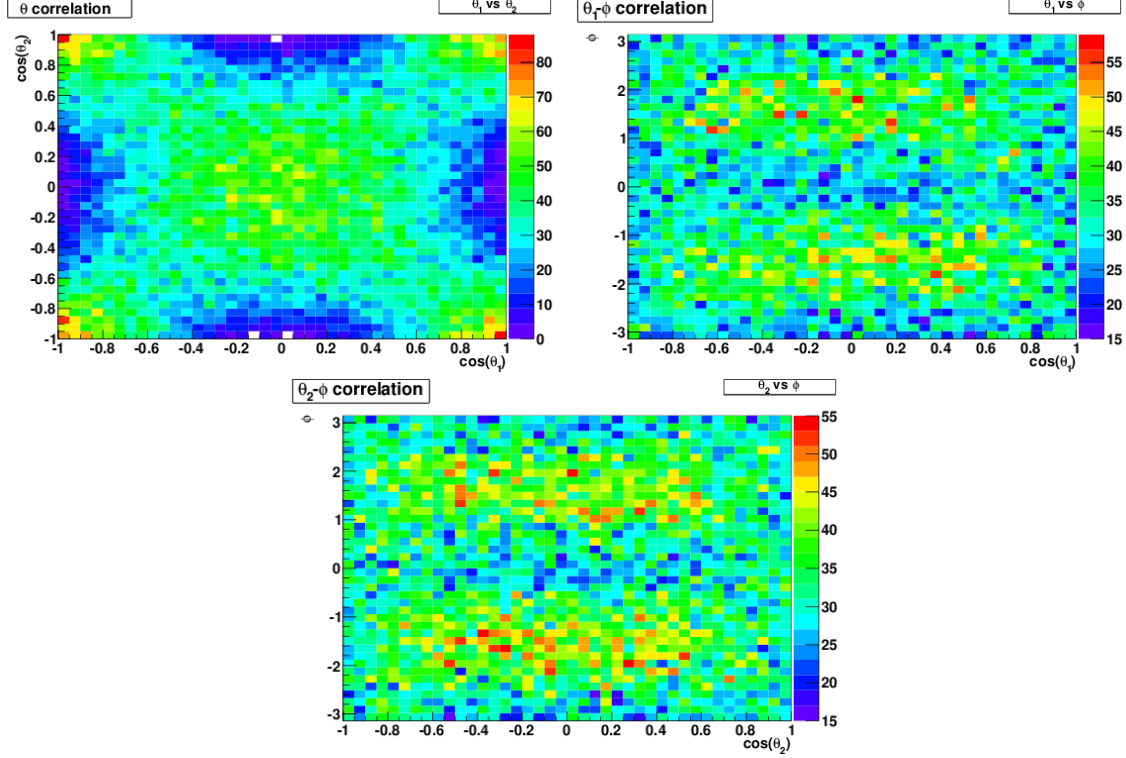


Figure 9.1.: Two-dimensional angular distributions of the helicity angles for simulated $B_s^0 \rightarrow \phi\phi$ events, (top left) $\theta_1 - \theta_2$, (top right) $\theta_1 - \Phi$ and (bottom) $\theta_2 - \Phi$. Clear correlation patterns can be observed.

Equation 6.2, maximizing the logarithmic likelihood is equal to solving the equation

$$\frac{\partial \ln \mathcal{L}}{\partial \lambda_j} = \frac{\partial}{\partial \lambda_j} \sum_{i=1}^N \ln \frac{S(\vec{x}_i; \vec{\lambda})}{\int S(\vec{x}; \vec{\lambda}) d\vec{x}} = 0, \quad (9.2)$$

where S is the unnormalized signal PDF, $\vec{x} = (m, \Omega)$ is the set of observables, $\vec{\lambda}$ is the set of parameters and the index i denotes the summation over all events N . The angular efficiency over the subset $\Omega \in \{\vec{x}\}$ can be included in Equation 9.2 as

$$\frac{\partial \ln \mathcal{L}}{\partial \lambda_j} = \frac{\partial}{\partial \lambda_j} \sum_i \ln \frac{S(\vec{x}_i; \vec{\lambda}) \epsilon(\Omega_i)}{\int \int S(\Omega, m; \vec{\lambda}) \epsilon(\Omega) dm d\Omega} = 0. \quad (9.3)$$

The efficiency $\epsilon(\Omega)$ does not depend on any of the fitted parameters $\vec{\lambda}$, because the invariant mass of a B_s^0 candidate is uncorrelated to the helicity angles. In this case, the logarithmic identity $\ln(AB) = \ln(A) + \ln(B)$ can be used to simplify Equation 9.3

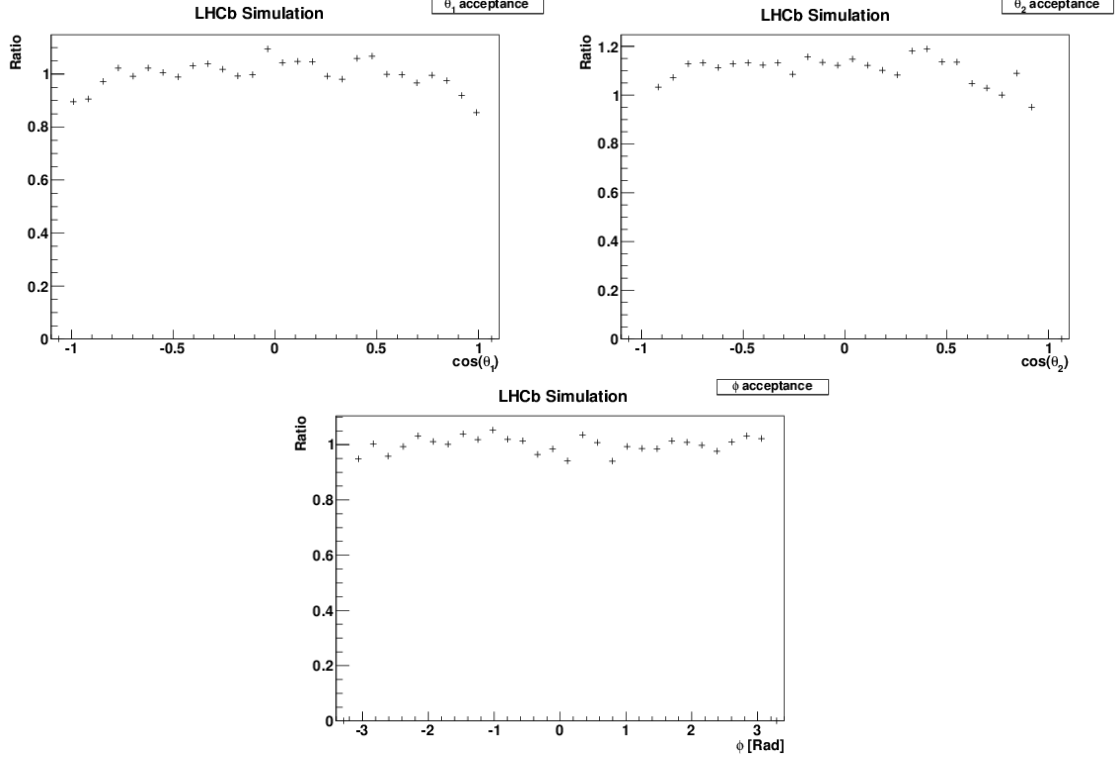


Figure 9.2.: One-dimensional projections of the three dimensional relative angular acceptance for each helicity angle calculated with simulated $B_s^0 \rightarrow \phi\phi$ decays.

further and derive that

$$\begin{aligned} \frac{\partial \ln \mathcal{L}}{\partial \lambda_j} &= \frac{\partial}{\partial \lambda_j} \left(\sum_i \ln \frac{S(\vec{x}_i; \vec{\lambda})}{\int \int S(\Omega, m; \vec{\lambda}) \epsilon(\Omega) dm d\Omega} \right) + \frac{\partial}{\partial \lambda_j} \left(\sum_i \ln \epsilon(\Omega_i) \right) \\ &= \frac{\partial}{\partial \lambda_j} \sum_i \ln \frac{S(\vec{x}_i; \vec{\lambda})}{\int \int S(\Omega, m; \vec{\lambda}) \epsilon(\Omega) dm d\Omega} = 0, \end{aligned} \quad (9.4)$$

since the derivative in the second term vanishes. Assuming that the PDF factorizes into an angular and a mass dependent part $f(\Omega)$ and $M(m)$, the angular efficiency weights may be defined through

$$\zeta(\Omega) = \int f(\Omega) \epsilon(\Omega) d\Omega, \quad (9.5)$$

which occur in the denominator of Equation 9.4

$$\frac{\partial \ln \mathcal{L}}{\partial \lambda_j} = \frac{\partial}{\partial \lambda_j} \sum_i \ln \frac{S(\vec{x}_i; \vec{\lambda})}{\int M(m; \vec{\lambda}) \zeta(\Omega) dm} = 0. \quad (9.6)$$

In this way, the acceptance is absorbed into the normalization of the PDF giving rise to *normalization weights*. Since the measurement presented in this analysis is time- and angular-independent, the angular acceptance is treated as a systematic uncertainty. To

estimate the systematic uncertainty of the angular acceptance, the three-dimensional acceptance is used to generate weighted pseudo-experiments and estimate the effect on the determination of the triple product asymmetries when ignoring angular efficiency effects. This method is summarized in Chapter 11. It is shown that the acceptance effects lead to a small systematic shift for A_U and A_V compared to the current statistical precision. A systematic uncertainty is assigned accordingly.

Determination of the triple product asymmetries

To determine the triple product asymmetries A_U and A_V the sample of selected $B_s^0 \rightarrow \phi\phi$ decays is split in two sub-samples of positive and negative U and V. The B_s^0 -mass distributions of the positive and negative U and V decays are fitted simultaneously with common parameters $\vec{\lambda}_{shared}$ and independent parameters $\vec{\lambda}_{independent}$ to allow for small differences in the shape of the mass peaks in the different sub sets. This means that a certain set of parameters is shared between all PDFs for the different data sets and signs of U(V) while the rest of the parameter set is independent in each mass fit. The complete set of parameters is then given by:

$$\vec{\lambda} = \vec{\lambda}_{shared} + \vec{\lambda}_{independent}. \quad (10.1)$$

For each invariant mass distribution of the B_s^0 candidates, a double Gaussian is used to model the signal peak together with two Crystal Ball functions for the $\Lambda_b \rightarrow \phi K^- p$ and $B^0 \rightarrow \phi K^*$ background components and an exponential function to model the combinatorial background. The PDF is given by Equation 6.3. The shape of the peaking background PDFs is fixed to the values determined in Chapter 7. For the normalization of the PDFs the peaking background yields for 2011 and 2012, also determined in Chapter 7, are used. The full background PDF defined in Equation 6.5 is of the form (for each sub set)

$$B(m; \alpha, \beta, \mu, \varsigma, n) = N_{combinatorial} \cdot \frac{1}{\alpha} e^{-\alpha m} + N_{\phi K^*} \cdot CB_1(m, \beta_1, \mu_1, \varsigma_1, n_1) + N_{\phi K p} \cdot CB_2(m_{B_s^0}, \beta_2, \mu_2, \varsigma_2, n_2), \quad (10.2)$$

while the signal PDF is

$$S(m; \bar{m}, \sigma_1, \sigma_2, f) = N_{sig} \cdot \left(\frac{f}{\sqrt{2\pi}\sigma_1} \cdot e^{-\frac{(m-\bar{m})^2}{2\sigma_1^2}} + \frac{1-f}{\sqrt{2\pi}\sigma_2} \cdot e^{-\frac{(m-\bar{m})^2}{2\sigma_2^2}} \right). \quad (10.3)$$

The parameters that are shared in the PDFs for 2011 and 2012 data with U(V) positive and negative are:

- σ_1 : The core resolution of the double Gaussian peaks.
- \bar{m} : The mean of the double Gaussian peaks.
- α : The slope of the exponential describing the combinatorial background.
- f : The fraction between the two Gaussian functions. It is fixed to $f = 0.75$ to ensure stability of the simultaneous fit. The value has been determined from simulation.
- $CB_{1,2}(m, \beta_{1,2}, \mu_{1,2}, \varsigma_{1,2}, n_{1,2})$: All parameters of the two Crystal Ball functions for the peaking background. This includes the means $\mu_{1,2}$, the widths $\varsigma_{1,2}$, the cutoff for the exponentials $\beta_{1,2}$ as well as the slopes of the exponentials $n_{1,2}$. Those parameters are fixed to the values obtained in Section 7.3 and 7.4.
- A_U and A_V : The triple product asymmetries defined in Equation 2.27 and 2.28.

The parameters allowed to be independent are:

- σ_2 : The second width of the double Gaussian to account for differences in the peak shapes due to a different detector calibration for the data taken in 2011 and 2012.
- N : The yields have to be independent since they differ for 2011 and 2012 data. This includes the signal yield as well as the expected number of peaking background events which is fixed to the yields determined in Chapter 7 and the number of combinatorial background events.

The asymmetries A_U and A_V are directly taken from the fit exploiting the relation

$$f_+^j = \frac{N^j}{2}(A_{U(V)}^j + 1), \quad (10.4)$$

$$f_-^j = \frac{N^j}{2}(1 - A_{U(V)}^j), \quad (10.5)$$

where $j \in \{S, B\}$ labels the signal or background part and N^j refers to the total number of signal or background events. The background asymmetry $A_{U(V)}^B$ quantifies the asymmetry of background events for U and V positive and negative. It has no physical meaning, but is included in the PDF to preserve the normalization. All triple product asymmetries referred to in this analysis are $A_{U(V)}^S$.

The mass distributions and the fitted functions for 2011 and 2012 data with the positive and negative U as well as positive and negative V are shown in Figure 10.1. The triple product asymmetries are found to be

$$A_U = -0.003 \pm 0.017,$$

$$A_V = -0.017 \pm 0.017,$$

where the uncertainty is statistical. All fit results are shown in Table 10.1. The measured triple product asymmetries are compatible with the Standard Model expectation of $A_U = A_V = 0$ within their statistical uncertainties. This corresponds to a conservation of the CP symmetry.

Parameter	distribution	fitted value	
\bar{m} [MeV/c ²]	U	5365.9 ± 0.28	
σ_1 [MeV/c ²]	U	13.41 ± 0.29	
α	U	$(1.38 \pm 0.59) \cdot 10^{-3}$	
σ_1 [MeV/c ²]	V	13.46 ± 0.30	
\bar{m} [MeV/c ²]	V	5365.9 ± 0.28	
α	V	$(1.34 \pm 0.59) \cdot 10^{-3}$	
A_U	U	-0.003 ± 0.017	
A_V	V	-0.017 ± 0.017	
		2011	2012
N_{Sig}	U	1180 ± 36	2765 ± 56
N_{Sig}	V	1178 ± 36	2759 ± 56
$N_{combBkg}$	U	57 ± 12	407 ± 30
$N_{combBkg}$	V	59 ± 12	413 ± 30
$N_{\phi K^*}$	both	12 (fixed)	27 (fixed)
$N_{\phi Kp}$	both	49 (fixed)	65 (fixed)
σ_2 [MeV/c ²]	U_+	25.81 ± 3.10	24.70 ± 2.71
σ_2 [MeV/c ²]	U_-	28.65 ± 5.84	25.13 ± 2.51
σ_2 [MeV/c ²]	V_+	29.60 ± 5.26	22.55 ± 2.69
σ_2 [MeV/c ²]	V_-	24.67 ± 3.01	26.35 ± 2.53

Table 10.1.: Parameters determined in the simultaneous fit to the invariant mass distributions of selected $B_s^0 \rightarrow \phi\phi$ candidates for U and V positive and negative, for 2011 and 2012 data. The horizontal line indicates the parameters which are shared between all PDFs.

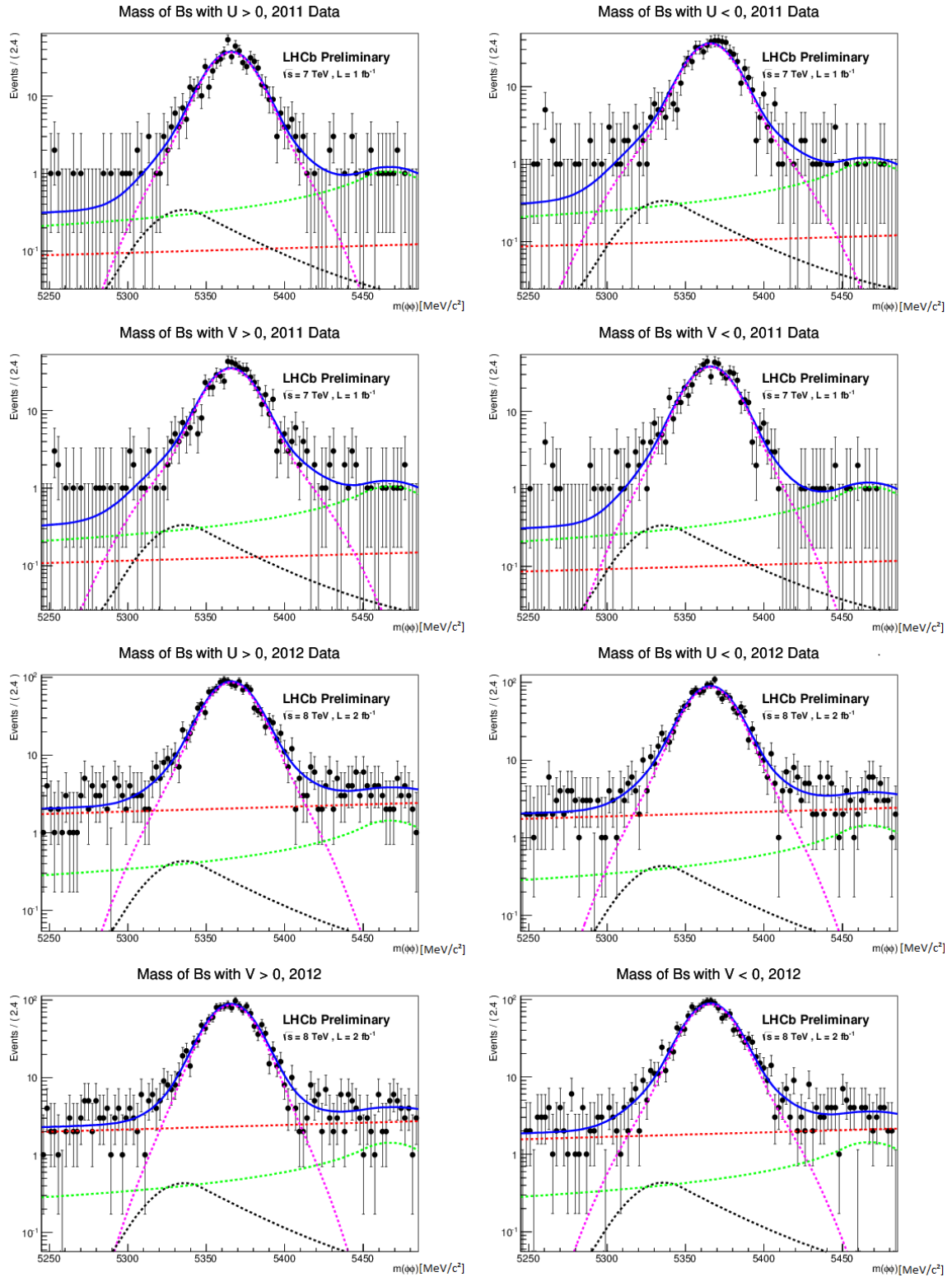


Figure 10.1.: Invariant mass distribution of the selected $B_s^0 \rightarrow \phi\phi$ candidates for 2011 and 2012 data; ϕK^* background in black and $\phi K p$ background in green, both described by a Crystal Ball function; Combinatorial background in red, described by an exponential function and $\phi\phi$ signal peak in magenta, described by a double Gaussian function.

10.1. Validation of the fitting procedure

It is crucial that the PDFs derived in the previous section are implemented correctly and that correlations between floating parameters do not introduce shifts in the values of the physical parameters. Additionally, it has to be validated that the statistical errors and the normalizations of the PDFs are handled correctly. To test the fitting procedure, pseudo-experiments in which decay configurations are generated according to a PDF are performed. To investigate the effect of limited statistics and estimate the expected statistical uncertainty, each pseudo-experiment is generated with the number of events found in real data. These are 1292 and 3292 events for the years 2011 and 2012, respectively. The events are generated according to the PDFs described in this chapter and are fitted the same way as the real data samples are treated to extract the triple product asymmetries. This pseudo-experiment is repeated 3000 times. The values of the fitted parameters should be distributed according to a Gaussian distribution and the mean of those distributions should reproduce the values used to generate the pseudo-experiments, given the fitting procedure works properly. The distributions of the fitted parameters are modeled with a Gaussian function to extract the mean value. If the number of events generated in each pseudo-experiment corresponds to the actual number of events in the real data sample, as it is the case in this analysis, also the statistical error of the fitted values should be reproduced. This is verified by modeling the distributions of the statistical error of each fitted parameter with a Gaussian function and taking the central value of the Gaussian as the mean statistical uncertainty. The results are shown in Table 10.2. All means are compatible with the generated values within their uncertainties and all expected statistical errors are reproduced without significant deviation.

The correct implementation of the fit can be tested using the pull distributions of the fitted observables. The pull p of a parameter A is defined as the difference of the generated and fitted values $A_{measured} - A_{generated}$, divided by the uncertainty σ_A of the fit:

$$p_A = \frac{A_{measured} - A_{generated}}{\sigma_A}, \quad (10.6)$$

With a correct fit implementation, the distributions of the pulls should be Gaussian shaped, with the mean being compatible with 0. The width of the Gaussian shape should be compatible with 1, because the deviation between the generated and fitted value and the statistical uncertainty of the fit are equal on average. Figure 10.2 and 10.3 show the pull distributions of all signal yields, which are used to extract the triple product asymmetries for the years 2011 and 2012. Every distribution is modeled with a Gaussian function to determine the respective mean and width. No significant deviation from the theoretical means and widths are observed, which proves that the normalization and error handling of the PDFs are implemented correctly.

Parameter	generated value \pm statistical error	mean of fitted values
U \bar{m} [MeV/c^2]	5365.9 ± 0.28	5365.8 ± 0.29
V \bar{m} [MeV/c^2]	5365.9 ± 0.28	5365.9 ± 0.31
U σ_1 [MeV/c^2]	13.41 ± 0.29	13.38 ± 0.32
V σ_1 [MeV/c^2]	13.46 ± 0.30	13.49 ± 0.33
U α	$(1.38 \pm 0.59) \cdot 10^{-3}$	$(1.44 \pm 0.62) \cdot 10^{-3}$
V α	$(1.34 \pm 0.59) \cdot 10^{-3}$	$(1.40 \pm 0.60) \cdot 10^{-3}$
<hr/>		
U_+ (2011) σ_2 [MeV/c^2]	25.81 ± 3.10	26.21 ± 3.32
U_- (2011) σ_2 [MeV/c^2]	28.65 ± 5.84	28.49 ± 4.01
V_+ (2011) σ_2 [MeV/c^2]	29.60 ± 5.26	27.94 ± 4.29
V_- (2011) σ_2 [MeV/c^2]	24.67 ± 3.01	24.05 ± 3.15
U_+ (2012) σ_2 [MeV/c^2]	24.70 ± 2.71	24.86 ± 2.42
U_- (2012) σ_2 [MeV/c^2]	25.13 ± 2.51	24.23 ± 2.18
V_+ (2012) σ_2 [MeV/c^2]	22.55 ± 2.69	23.35 ± 2.38
V_- (2012) σ_2 [MeV/c^2]	26.35 ± 2.53	26.87 ± 2.82
U (2011) f_+^S	592 ± 26	600 ± 26
U (2011) f_-^S	582 ± 29	585 ± 27
V (2011) f_+^S	571 ± 28	579 ± 27
V (2011) f_-^S	603 ± 26	601 ± 27
U (2012) f_+^S	1352 ± 43	1368 ± 43
U (2012) f_-^S	1375 ± 43	1370 ± 43
V (2012) f_+^S	1344 ± 43	1344 ± 43
V (2012) f_-^S	1379 ± 43	1378 ± 43

Table 10.2.: Generated and fitted values and errors of the free fit parameters derived from pseudo-experiments. The horizontal line indicates the parameters which are shared between all PDFs.

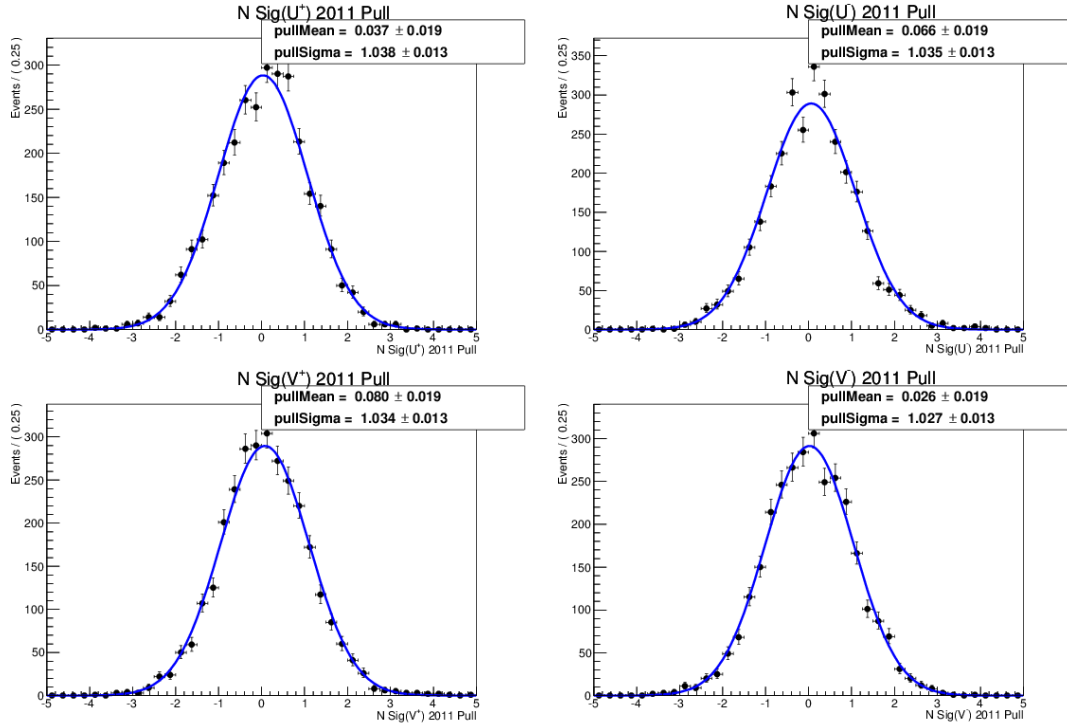


Figure 10.2.: Pull distributions for f_{\pm}^S of 3000 toy studies with 1292 events for 2011.

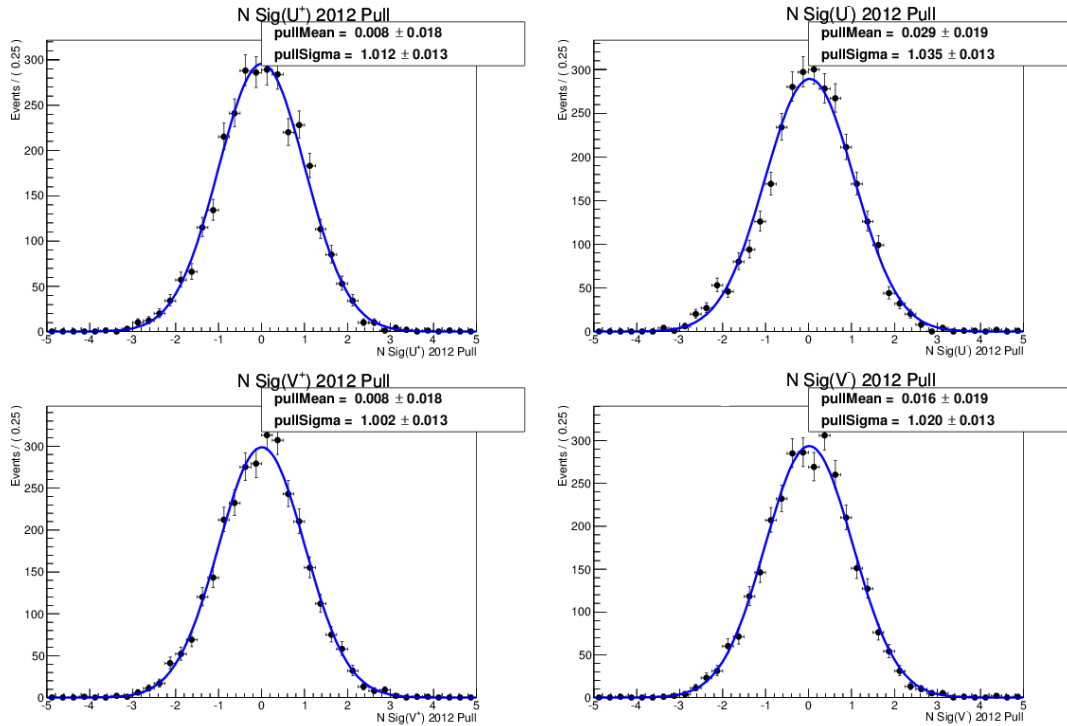


Figure 10.3.: Pull distributions for f_{\pm}^S of 3000 toy studies with 3292 events for 2012.

Estimation of systematic uncertainties

In this chapter the systematic uncertainties of the measurement of the triple product asymmetries are discussed. As pointed out in Chapter 4, the peaking background sources as well as the angular acceptance and decay-time efficiency are contributing to the uncertainties of the triple product asymmetry measurement. Since the measurement builds upon the correct parameterization of the B_s^0 mass distribution for positive and negative values of U and V , the mass model used to fit these distributions is a source of systematic uncertainty and is therefore also considered here.

Pseudo-experiments further referred to as *toys* are used to estimate the effect of the angular and decay-time acceptance. Using the parameterization of both effects discussed in Chapter 8 and 9 it is possible to generate toy sets with and without acceptance effects and estimate their effect on the triple product asymmetries A_U and A_V . The systematic uncertainties arising from the mass model and the exact number of peaking background events are estimated by directly varying the respective fit components and investigating the effect on the triple product asymmetries.

11.1. decay-time acceptance

To investigate the systematic uncertainty related to the decay-time acceptance, an explicitly time-dependent parameterization of the theoretical decay rate for $B_s^0 \rightarrow \phi\phi$ decays is taken from [3]:

$$\frac{d\Gamma}{dt d \cos \theta_1 d \cos \theta_2 d \Phi} \propto 4 |\mathcal{A}(t, \theta_1, \theta_2, \Phi)|^2 = \sum_{i=1}^6 K_i(t) f_i(\theta_1, \theta_2, \Phi), \quad (11.1)$$

where the decay rate factorizes in the time-dependent functions $K_i(t)$ and the angular functions $f_i(\theta_1, \theta_2, \Phi)$. The angular part is equal to the decay rate defined in Equation 2.16 and the time dependent part is given by:

$$K_i(t) = N_i e^{-\Gamma_s t} [c_i \cos(\Delta m_s t) + d_i \sin(\Delta m_s t) + a_i \cosh(\frac{1}{2} \Delta \Gamma_s t) + b_i \sinh(\frac{1}{2} \Delta \Gamma_s t)], \quad (11.2)$$

where Δm_s is the mixing frequency describing the $B_s^0 - \overline{B}_s^0$ oscillation, Γ_s is the decay width and $\Delta \Gamma_s$ is the decay width difference between the light and heavy mass eigenstates

i	N_i	a_i	b_i	c_i	d_i
1	$ A_0 ^2$	1	$-\cos \phi_s$	0	$\sin \phi_s$
2	$ A_{ } ^2$	1	$-\cos \phi_s$	0	$\sin \phi_s$
3	$ A_{\perp} ^2$	1	$\cos \phi_s$	0	$-\sin \phi_s$
4	$ A_{ } A_{\perp} $	0	$-\cos \delta_1 \sin \phi_s$	$\sin \delta_1$	$-\cos \delta_1 \cos \phi_s$
5	$ A_{ } A_0 $	$\cos \delta_{2,1}$	$-\cos \delta_{2,1} \cos \phi_s$	0	$\cos \delta_{2,1} \sin \phi_s$
6	$ A_0 A_{\perp} $	0	$-\cos \delta_2 \sin \phi_s$	$\sin \delta_2$	$-\cos \delta_2 \cos \phi_s$

Table 11.1.: Coefficients of the time dependent part K_i [3].

Parameter	Input Value
Γ_s	0.662 ps^{-1}
$\Delta\Gamma_s$	0.102 ps^{-1}
Δm_s	17.774 ps^{-1}
$ A_0 ^2$	0.365
$ A_{ } ^2$	0.331
$ A_{\perp} ^2$	0.304
δ_1	0.12 rad
δ_2	2.67 rad
ϕ_s	$\in \{-0.5, 0, 0.5\}$ rad

Table 11.2.: Input values for the generation of toy sets. Taken from [3].

of the B_s^0 meson. The factors N , a , b , c and d are given in Table 11.1, where ϕ_s is the CP-violating phase arising from the interference of mixing and decay in $B_s^0 \rightarrow \phi\phi$ and δ_i are the strong phases $\delta_1 = \delta_{\perp} - \delta_{||}$ and $\delta_2 = \delta_{\perp} - \delta_0$.

For the generation of toy sets, input values for all parameters of the time-dependent decay rate 11.1 are needed. The values are taken from [3] and shown in Table 11.2. For the CP-violating phase, different assumptions are made ($\phi_s \in \{-0.5, 0, 0.5\}$ rad) and the results are compared to investigate the effect of the value of ϕ_s on the triple product asymmetries. This procedure accounts for the fact that the statistical error of the ϕ_s determination in the $B_s^0 \rightarrow \phi\phi$ channel is still quite large.

Toy sets are generated using Equation 11.1 with and without the application of the decay-time acceptance correction histograms determined in Chapter 8 and shown in Figure 8.5 and Figure 8.6. 1000 pseudo-experiments with and without decay-time acceptance effects, each with 10000 events are generated for $\phi_s = -0.5$, $\phi_s = 0$ and $\phi_s = 0.5$. As it is done with the actual data, each set is divided into subsets with $U(V) > (<) 0$ and the triple product asymmetries are determined, ignoring possible acceptance effects. For each fit, the difference between the fitted asymmetries from the set with acceptance effects and the set without effects

$$\Delta A_{U/V} = A_{U/V}^{\epsilon t} - A_{U/V}^{w/o \epsilon t}, \quad (11.3)$$

where ϵ_t symbolizes the set with time efficiency effects and $w/o \epsilon_t$ otherwise, is computed. The distributions of ΔA_U and ΔA_V defined in Equation 11.3 are described by a Gaussian function to determine the overall deviation from the generated values of A_U and A_V . The distributions and the fits are shown in Figure 11.1. Three different values for the systematic uncertainty $\Delta A_{U/V}$ are obtained for the three different assumptions on ϕ_s . The values are shown in Table 11.3 where the largest value is conservatively chosen as the systematic uncertainty for both A_U and A_V , because there is no reason for a difference.

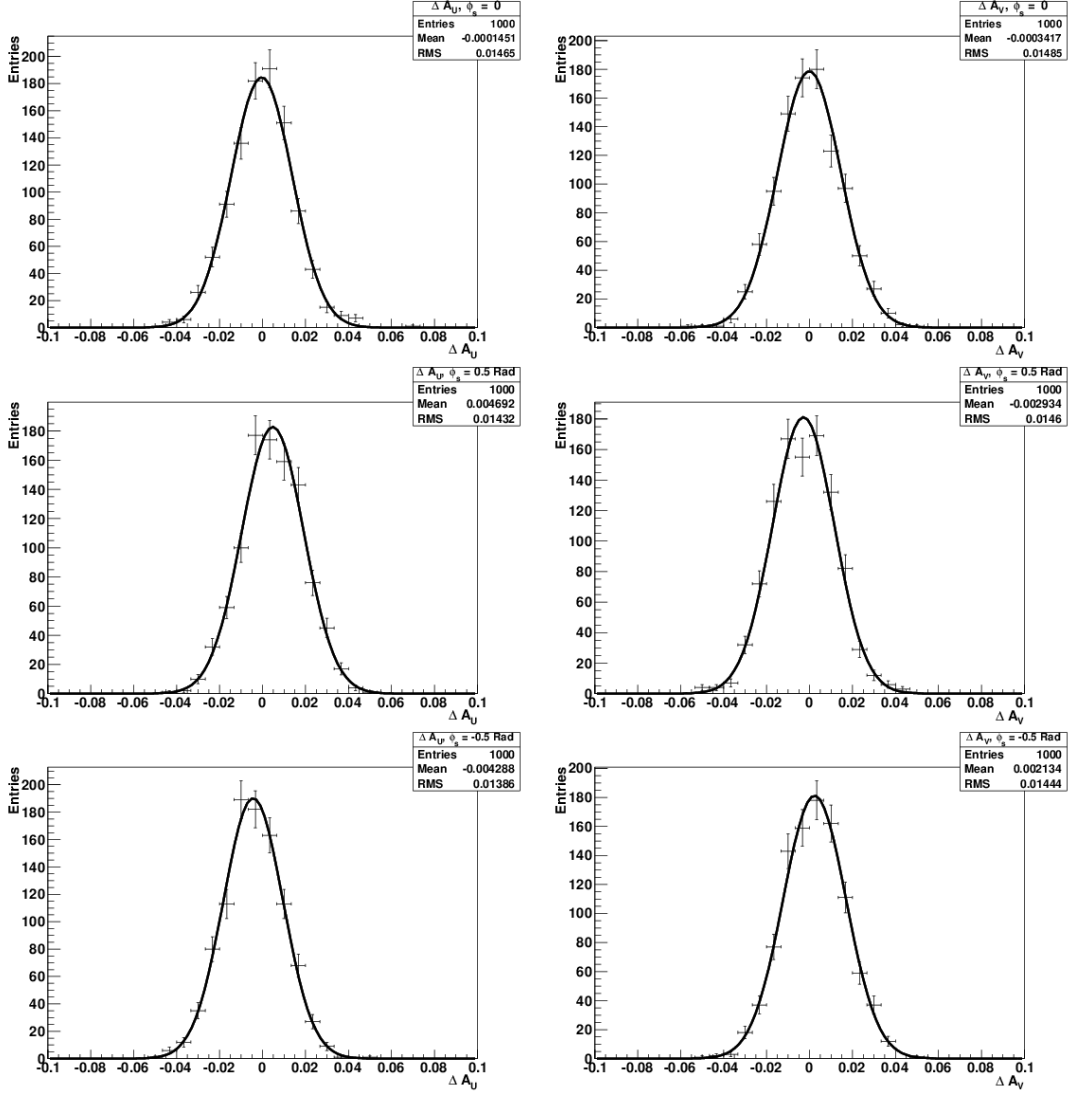


Figure 11.1.: Difference of the fitted triple product asymmetries due to the decay-time efficiency described by a Gaussian function for $\phi_s \in \{-0.5, 0, 0.5\}$ rad.

ϕ_s (rad)	$ \Delta A_U $	$ \Delta A_V $
0	–	–
+0.5	0.005	0.003
-0.5	0.004	0.002

Table 11.3.: Uncertainties due to decay-time acceptance for the triple product asymmetries.

11.2. Angular distribution

The systematic uncertainty due to the angular efficiency is estimated similarly to the one related to the decay-time acceptance described in the previous section. As described in Chapter 9, the angular detector and reconstruction efficiency can be accounted for by the use of normalization weights defined in Equation 9.5 for the angular terms f_i . To investigate the effect of the angular acceptance on the triple product asymmetries, pseudo-experiments are generated according to the time- and angular-dependent decay rate defined in Equation 11.1. The input values for the toy generation are again taken from Table 11.2. The CP-violating phase ϕ_s is varied using three different inputs $\phi_s \in \{-0.5\pi, 0, 0.5\pi\}$. The input values for ϕ_s were chosen in this way to ensure comparability with the previous analysis of triple product asymmetries in the $B_s^0 \rightarrow \phi\phi$ decay [37].

1000 toys with 10000 events are generated with and without acceptance effects. For each set, the resulting mass distributions are again divided into subsets with U and V larger and smaller than zero and are fitted using the PDF given in Equation 6.3. Again, the difference $\Delta A_{U/V}$ is computed according to Equation 11.3. The overall difference is determined by a Gaussian fit to the $\Delta A_{U/V}$ distributions with the mean of the Gaussian being the systematic uncertainty. The uncertainties are shown in Table 11.4, where the largest deviation for the different ϕ_s assumptions is chosen to be the overall systematic uncertainty for A_U and A_V . The distributions of $\Delta A_{U/V}$ and the Gaussian fits are shown in Figure 11.2.

ϕ_s (π)	$ \Delta A_U $	$ \Delta A_V $
0	0.001	0.003
+0.5	0.001	0.002
-0.5	0.001	0.002

Table 11.4.: Uncertainties due to angular acceptance for the triple product asymmetries.

11.3. Peaking background

The analysis of backgrounds from other b-hadron decays described in Chapter 7 concludes that $\Lambda_b^0 \rightarrow \phi K^- p$ and $B^0 \rightarrow \phi K^*$ decays pollute the full 2011+2012 $B_s^0 \rightarrow \phi\phi$

data sample with $N_{\Lambda_b^0} = 114 \pm 36$ and $N_{B^0} = 38 \pm 2$ events, respectively. To estimate the uncertainty arising from the error on the exact number of peaking background events, the simultaneous fits to the mass distributions of the $B_s^0 \rightarrow \phi\phi$ candidates described in Chapter 10 are repeated. The mass spectrum is partitioned into subsets with U and V larger and smaller than zero and the peaking background yields are varied by $\pm 1 \sigma$ of statistical uncertainty.

The observed maximum deviation of the triple product asymmetry A_V from the nominal fit result is $|\Delta A_V| = 0.001$ while no effect is observed for A_U . Thus, the systematic uncertainty arising from the peaking background components is conservatively chosen to be $|\Delta A_{U/V}| = 0.001$ for each asymmetry.

11.4. Mass model

The determination of the triple product asymmetries relies primarily on the correct parameterization of the mass distribution of the B_s^0 candidates to extract the yields of $B_s^0 \rightarrow \phi\phi$ decays with positive and negative signs of $U = \sin(2\Phi)$ and $V = \pm \sin(\Phi)$. However, the chosen parameterization using a double Gaussian model for the signal peak together with an exponential model for the combinatorial background is not unique. It is also possible to model the signal with a single or a triple Gaussian and the combinatorial with a polynomial function instead. A change of the mass model might introduce a shift of the obtained values for A_U and A_V . Since there is no unique description, the possible shift has to be investigated and is accounted for as a systematical uncertainty.

To study the effect of the mass model, the simultaneous fits to the 2011 and 2012 mass distributions of the B_s^0 candidates for positive and negative values of $U(V)$ are repeated using a single Gaussian and a triple Gaussian to model the signal peak. The triple Gaussian is of the form

$$TG(m; \vec{\lambda}_{sig}) = \frac{f_1}{\sqrt{2\pi}\sigma_1} \cdot e^{-\frac{(m-\bar{m})^2}{2\sigma_1^2}} + \frac{f_2}{\sqrt{2\pi}\sigma_2} \cdot e^{-\frac{(m-\bar{m})^2}{2\sigma_2^2}} + \frac{1-f_1-f_2}{\sqrt{2\pi}\sigma_3} \cdot e^{-\frac{(m-\bar{m})^2}{2\sigma_3^2}}, \quad (11.4)$$

where the new parameters f_2 and σ_3 are introduced to account for the fraction of the third Gaussian and its width, respectively. Also the combinatorial background model is exchanged by a linear polynomial of the form

$$Poly(m; \vec{\lambda}_{bg}) = c_0 + c_1 \cdot m, \quad (11.5)$$

together with a double Gaussian function to model the signal. The coefficients c_i determine the offset and the slope of the PDF.

The fits to the 2012 data with $U > 0$ using a single Gaussian, a triple Gaussian and a polynomial background are shown in Figure 11.3. The maximum shift of the triple product asymmetries due to the mass model is found to be $|\Delta A_U| = |\Delta A_V| = 0.002$.

11.5. Summary

In the previous sections, several sources of systematic uncertainties for the measurement of triple product asymmetries have been discussed. It is found that the decay-time efficiency, the angular acceptance as well as the peaking backgrounds and the applied mass model introduce small systematic uncertainties to the analysis. The two largest contributions are the detector-dependent decay-time and angular efficiency effects while the uncertainties on the peaking background components are only a minor contribution. Table 11.5 summarizes the sources for systematic uncertainties and indicates which error is taken for both measured asymmetries. The total systematic error is obtained by adding the components in quadrature. The total systematic uncertainty is almost three times smaller than the statistical uncertainty, which makes the analysis statistically limited.

Source	$ \Delta A_U $	$ \Delta A_V $	Error Taken
Angular acceptance	0.001	0.003	0.003
decay-time acceptance	0.005	0.003	0.005
Mass model	0.002	0.002	0.002
peaking Background	–	0.001	0.001
Total	0.006	0.005	0.006

Table 11.5.: Summary of systematic uncertainties for the triple product asymmetries.

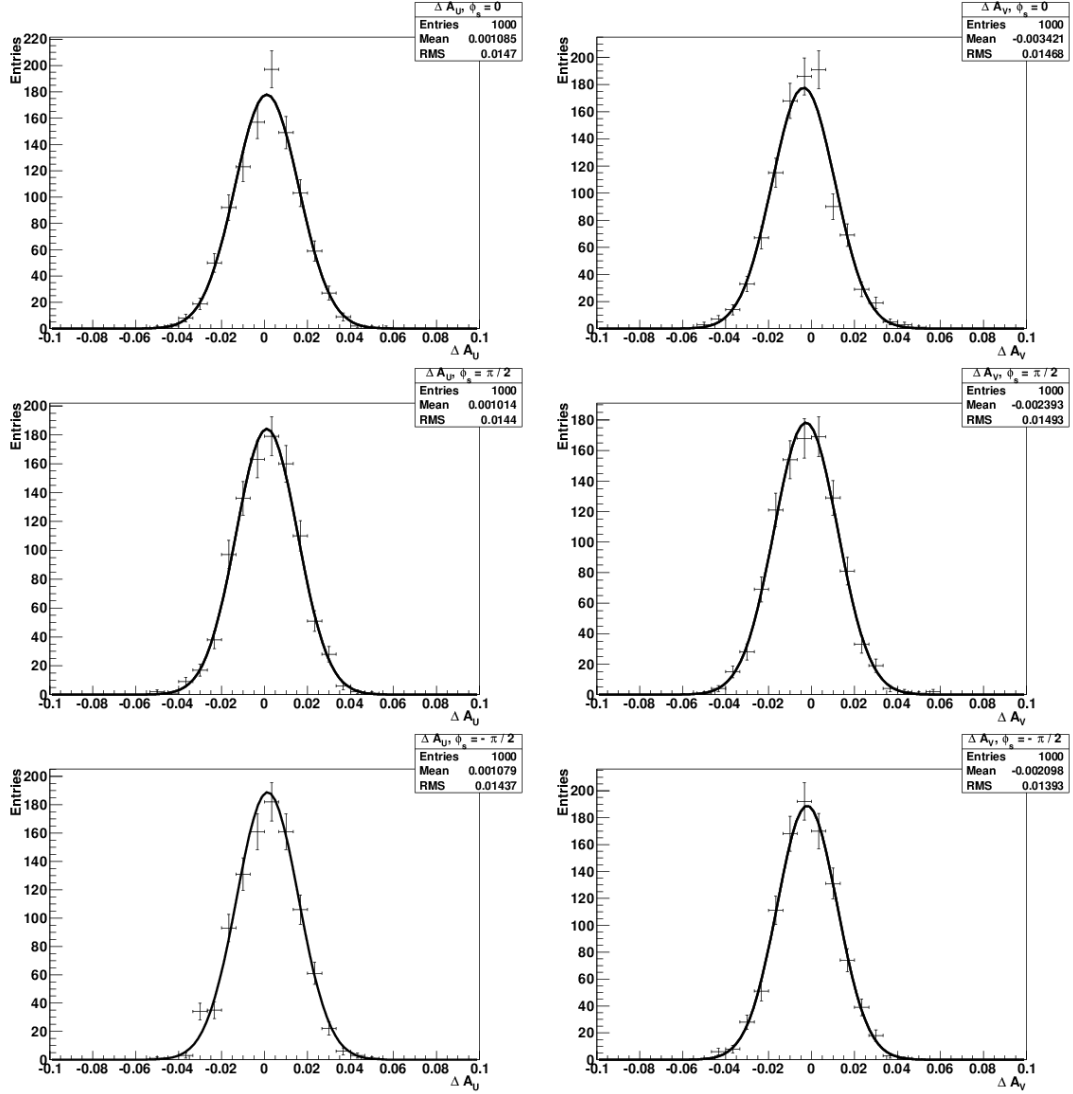


Figure 11.2.: Difference of the fitted triple product asymmetries due to the angular efficiency described by a Gaussian function for $\phi_s \in \{-0.5, 0, 0.5\} \pi$.

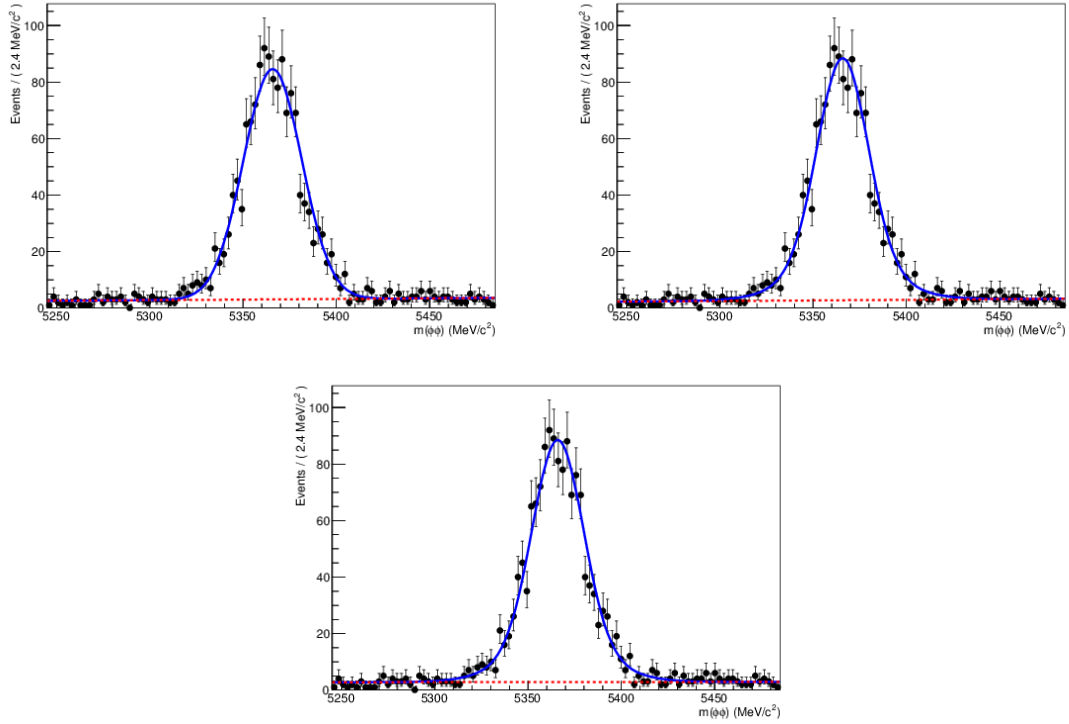


Figure 11.3.: Fit to the mass distribution of B_s^0 candidates using a (top left) single Gaussian, (top right) triple Gaussian and a double Gaussian for the signal together with (bottom) a linear polynomial for the combinatorial background.

Summary and outlook

This thesis presents the time-independent analysis of CP-violating triple product asymmetries A_U and A_V in $B_s^0 \rightarrow \phi\phi$ decays. For the analysis, a data sample corresponding to an integrated luminosity of $\mathcal{L} = 3.1 \text{ fb}^{-1}$ collected at the LHC during the years 2011 and 2012 is analyzed. The center of mass energies are $\sqrt{s} = 7$ and 8 TeV, respectively, and roughly 3900 signal candidates are found. The fitting procedure applied to determine A_U and A_V is a simultaneous unbinned maximum likelihood fit to the invariant mass distributions of the $B_s^0 \rightarrow \phi\phi$ candidates. The distributions are partitioned according to the sign of the triple products $U = \sin 2\Phi$ and $V = \pm \sin \Phi$ in each event and the fit is used to determine the event yield and the asymmetries.

To separate the $B_s^0 \rightarrow \phi\phi$ decays from background events, a selection procedure is applied. The first step includes a cut-based selection that aims to roughly select the $B_s^0 \rightarrow \phi\phi$ signal candidates from the data sample. In the second step, a multivariate analysis tool is used to combine information from different decay observables of the B_s^0 candidates which are capable of separating signal from background events. The background that cannot be removed by the selection steps is found to be composed of combinatorics as well as of the physical decays $B^0 \rightarrow \phi K^*$ and $\Lambda_b^0 \rightarrow \phi K^- p$. Those background components are accounted for in the PDF of the simultaneous fit. Time acceptance effects due to the reconstruction and selection process of $B_s^0 \rightarrow \phi\phi$ events are determined using $B_s^0 \rightarrow D_s^+ \pi^-$ decays. The angular efficiency is estimated using fully simulated events that mimic the detector and selection effects. The two acceptance effects are found to be the dominant contributions to the systematic uncertainties for the presented analysis. The obtained triple product asymmetries are

$$A_U = -0.003 \pm 0.017(stat) \pm 0.006(syst),$$

$$A_V = -0.017 \pm 0.017(stat) \pm 0.006(syst).$$

The results are compatible with the Standard Model prediction of zero corresponding to CP conservation in this decay. The asymmetries were first measured by the CDF Collaboration in 2011 [1], using 295 $B_s^0 \rightarrow \phi\phi$ candidates found in a data sample corresponding to an integrated luminosity of 2.9 fb^{-1} . CDF found $A_U = -0.007 \pm 0.064 \pm 0.018$ and $A_V = -0.120 \pm 0.064 \pm 0.016$, where the first errors is statistical and the second systematical. The presented measurement has improved statistical and systematical precision with respect to the CDF measurement.

The measurement uncertainty of the triple product asymmetries is dominated by the statistical error. Starting in spring of 2015, the LHC aims to run at the design energy of $\sqrt{s} = 14 \text{ TeV}$. During Run 2 the LHCb collaboration expects additional data corresponding to 5-6 fb^{-1} of integrated luminosity [43]. This will decrease the statistical error by at least 40%. However, there is also room for improvement of the systematical uncertainties, as a better understanding of the acceptance effects would decrease the systematical error. Especially the drop of angular efficiency as $\cos \theta_{1/2}$ approaches ± 1 , due to the p_t cut on the final state kaons and the trigger selection, requires further treatment. The mass distribution of selected $B_s^0 \rightarrow \phi\phi$ candidates could be reweighted according to the three-dimensional efficiency $\epsilon(\Omega)$ to account for this angular acceptance effect. On the other hand, new physical background components might get significant with higher statistics and the peaking background studies would have to be expanded.

The presented measurement is the world's most precise determination of triple product asymmetries in the $B_s^0 \rightarrow \phi\phi$ decay.

Distributions of the multivariate analysis variables

Figure A.1-A.6 show the distributions for the variables used in the multivariate analysis presented in Section 5.3 for 2011 and 2012 data. The signal sample is taken from fully simulated events and the background sample is taken from the sidebands of the invariant mass distributions of $B_s^0 \rightarrow \phi\phi$ candidates. The sidebands are defined as the mass region which is at least $120 \text{ MeV}/c^2$ larger or smaller than the B_s^0 PDG mass.

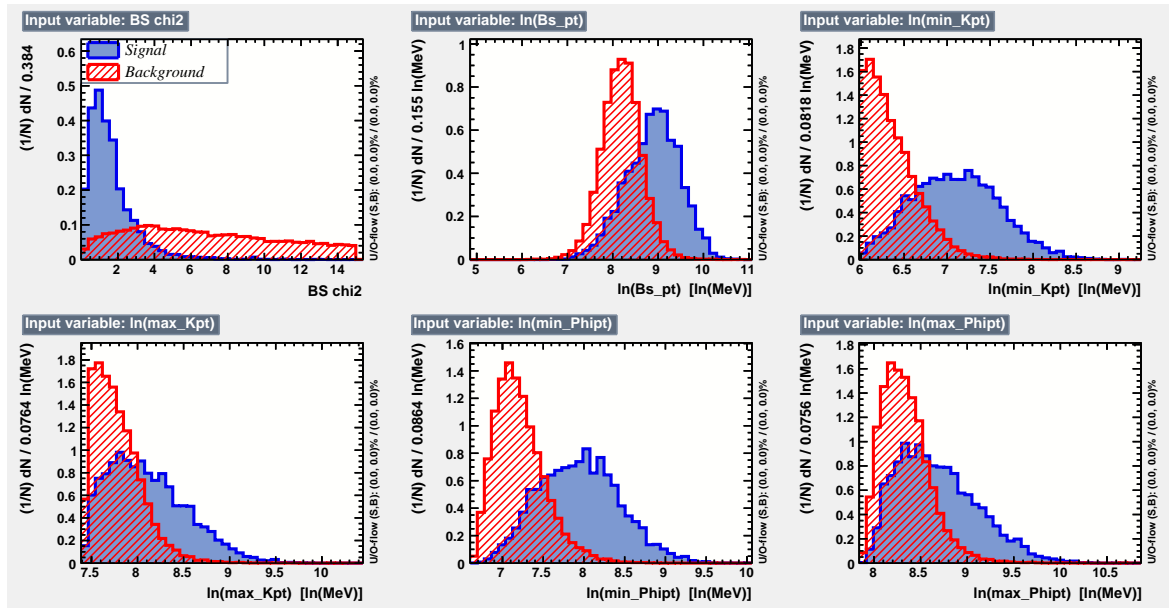


Figure A.1.: Input variables to the 2011 BDT (part 1 of 3).

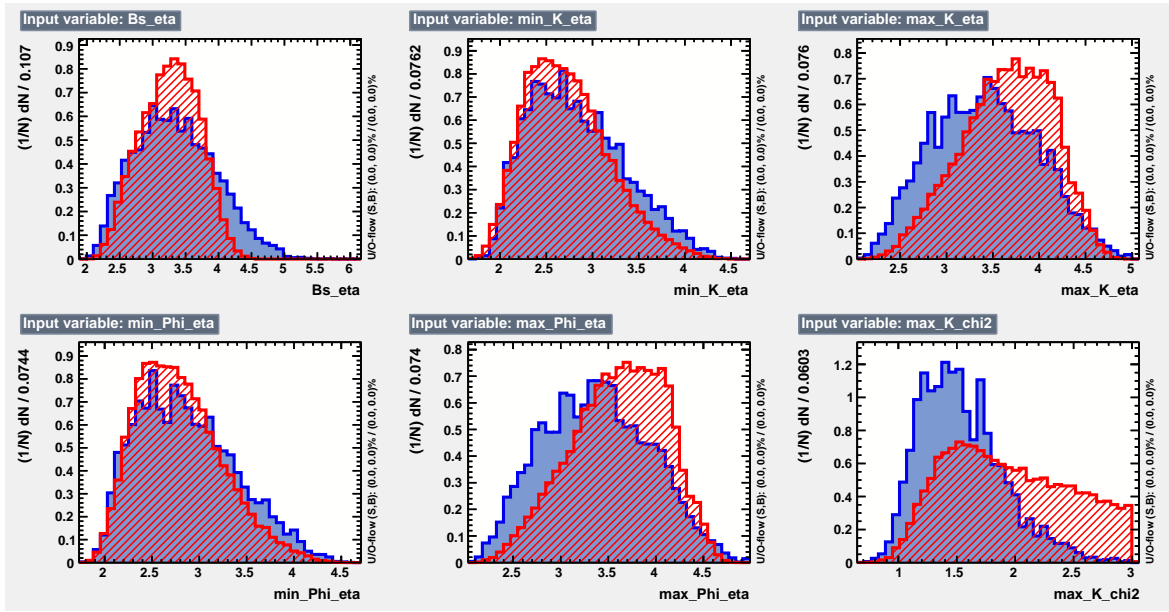


Figure A.2.: Input variables to the 2011 BDT (part 2 of 3).

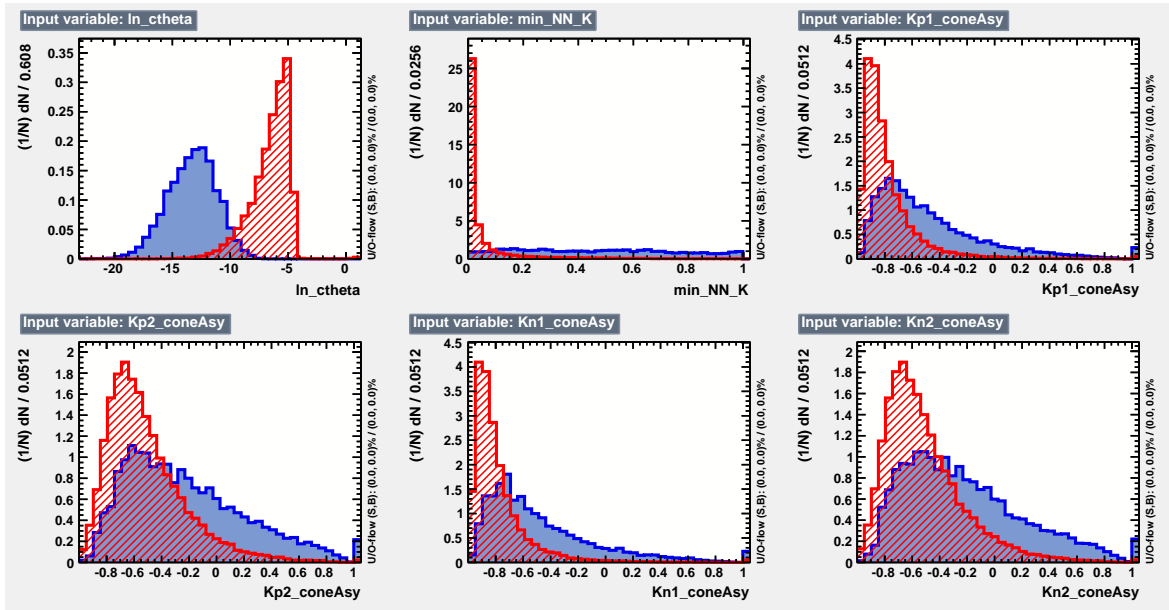


Figure A.3.: Input variables to the 2011 BDT (part 3 of 3).

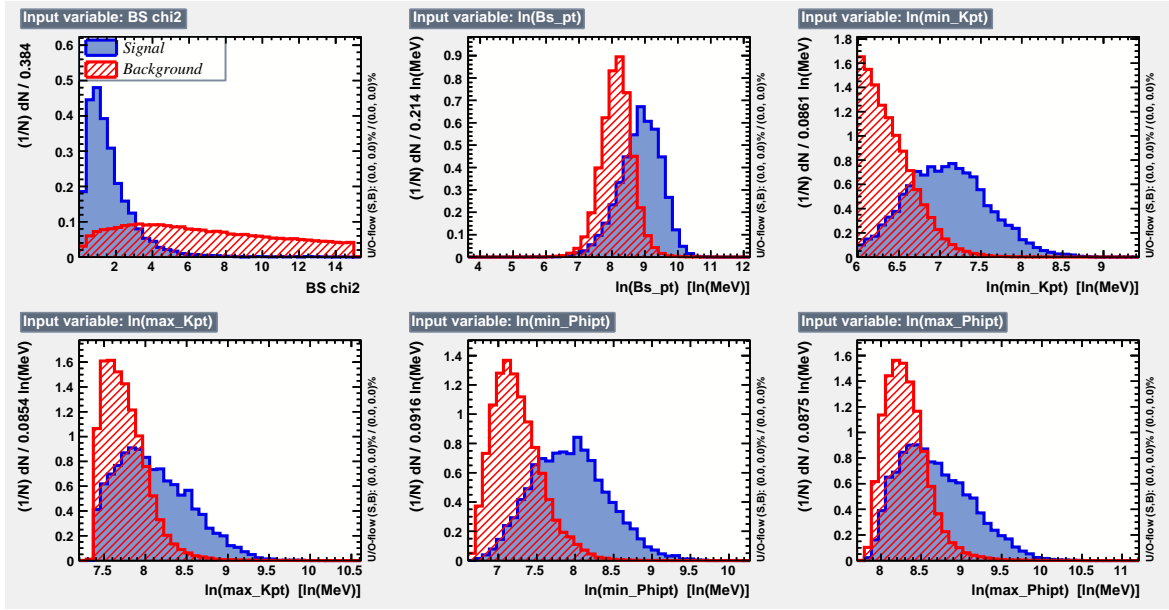


Figure A.4.: Input variables to the 2012 BDT (part 1 of 3).

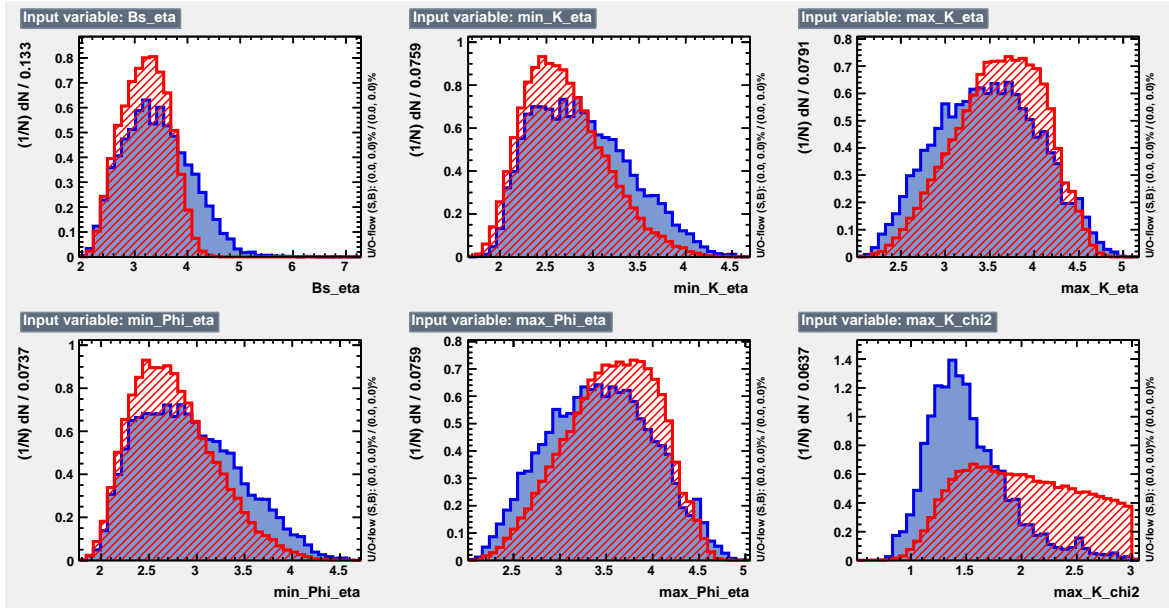


Figure A.5.: Input variables to the 2012 BDT (part 2 of 3).

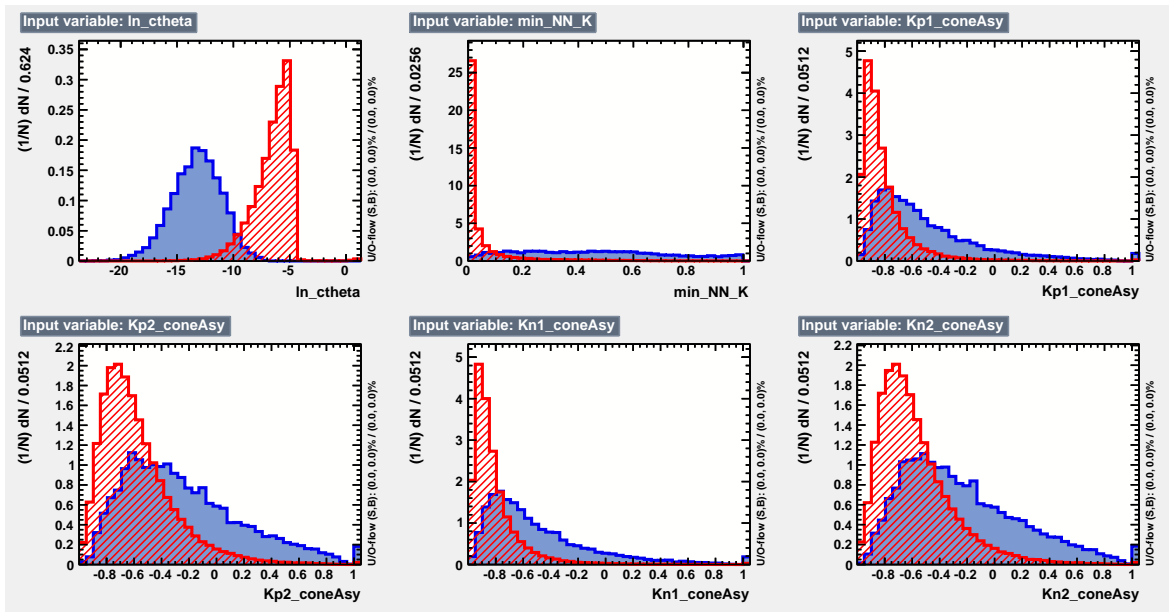


Figure A.6.: Input variables to the 2012 BDT (part 3 of 3).

Acknowledgments

Many people contributed to the presented analysis and helped me to complete this thesis. First, I would like to thank my supervisor Ulrich Uwer who gave me the opportunity to be a part of the Heidelberg LHCb group and provided a lot of helpful comments and advice to improve this thesis. Also, I would like to thank Hans-Christian Schultz-Coulon who agreed to be the second referee for my thesis and Stephanie Hansmann-Menzemer for the useful advice during our weekly group seminar.

I would like to express my gratitude to the whole LHCb group at the PI Heidelberg for providing such a pleasant, friendly working atmosphere throughout the year. In particular, I am thankful to Max Neuner for the countless times he explained details of a certain part of the analysis to me and sharpened my physical understanding. He also provided many comments for this thesis and reviewed it several times. The next person I would like to thank is Francesca Dordei who introduced me to ROOT and Roofit during my Bachelor thesis in 2012. Without the advice she gave me on many technical issues, as well as the physics behind them, this analysis would not have been possible. Thanks are also due to Sascha Stahl who reviewed the latest version of this thesis and showed me some features of LaTeX which I had no idea about. Within the LHCb group at the Physikalisches Institut there are friends I have known since the first Bachelor semester back in 2009. David, Dominik, Philippe, it is nice that we went this way together. Also thanks to my office mates Nikolai and Peter for the friendly atmosphere.

Next I would like to thank my friends in- and outside of physics. All of them contributed in different ways to my personal life and/or the work I have done.

Finally and above all, I would like to express my gratitude to my parents who supported me in everything I did my whole life. Without your help and trust non if this would have happened.

Bibliography

- [1] CDF Collaboration, T. Aaltonen *et al.*, *Measurement of Polarization and Search for CP-Violation in $B_s^0 \rightarrow \phi\phi$ Decays*, Phys. Rev. Lett. **107** (2011) 261802, [arXiv:1107.4999](#).
- [2] LHCb, S. Benson *et al.*, *Search for CP Violation in the $B_s^0 \rightarrow \phi\phi$ Decay with the Full LHCb Run I Dataset*, LHCb-ANA-2014-035.
- [3] LHCb collaboration, R. Aaij *et al.*, *Measurement of CP violation in $B_s^0 \rightarrow \phi\phi$ decays*, [arXiv:1407.2222](#), Submitted to Phys. Rev. D.
- [4] S. L. Glashow, *Partial-symmetries of weak interactions*, Nuclear Physics **22** (1961), no. 4 579 .
- [5] A. Salam and J. Ward, *Weak and electromagnetic interactions*, Il Nuovo Cimento Series 10 **11** (1959), no. 4 568.
- [6] S. Weinberg, *A model of leptons*, Phys. Rev. Lett. **19** (1967) 1264.
- [7] http://upload.wikimedia.org/wikipedia/commons/0/00/Standard_Model_of_Elementary_Particles.svg.
- [8] P. W. Higgs, *Broken symmetries and the masses of gauge bosons*, Phys. Rev. Lett. **13** (1964) 508.
- [9] G. A. et al., *Observation of a new particle in the search for the standard model higgs boson with the atlas detector at the lhc*, Physics Letters B **716** (2012), no. 1 1 .
- [10] S. C. et al., *Observation of a new boson at a mass of 125 gev with the cms experiment at the lhc*, Physics Letters B **716** (2012), no. 1 30 .
- [11] M. Kobayashi and T. Maskawa, *Cp-violation in the renormalizable theory of weak interaction*, Progress of Theoretical Physics **49** (1973), no. 2 652, [arXiv:http://ptp.oxfordjournals.org/content/49/2/652.full.pdf+html](#).
- [12] L. Wolfenstein, *Parametrization of the Kobayashi-Maskawa Matrix*, Phys. Rev. Lett. **51** (1983) 1945.

- [13] <http://www.physik.uzh.ch/~che/FeynDiag/Details.php?code=52200101>.
- [14] S. L. Glashow, J. Iliopoulos, and L. Maiani, *Weak interactions with lepton-hadron symmetry*, Phys. Rev. D **2** (1970) 1285.
- [15] A. D. Sakharov, *Violation of cp in variance, c asymmetry, and baryon asymmetry of the universe*, Soviet Physics Uspekhi **34** (1991), no. 5 392.
- [16] M. Gronau and J. L. Rosner, *Triple-product asymmetries in k , $D_{(s)}$, and $B_{(s)}$ decays*, Phys. Rev. D **84** (2011) 096013.
- [17] C. W. Wong, *Introduction to Mathematical Physics*, Oxford University Press, 2013.
- [18] LHCb collaboration, R. Aaij *et al.*, *First measurement of the CP-violating phase in $B_s^0 \rightarrow \phi\phi$ decays*, Phys. Rev. Lett. **110** (2013) 241802, [arXiv:1303.7125](https://arxiv.org/abs/1303.7125).
- [19] LHCb Collaboration, B. Adeva *et al.*, *Roadmap for selected key measurements of LHCb*, [arXiv:0912.4179](https://arxiv.org/abs/0912.4179).
- [20] http://lhcb.web.cern.ch/lhcb/speakersbureau/html/Material_for_Presentations.html.
- [21] J. Nardulli, *Reconstruction of two-body B decays in LHCb*, PhD thesis, NIKHEF, Amsterdam, 2007, Presented on 04 Oct 2007.
- [22] LHCb collaboration, R. Aaij *et al.*, *Measurement of $\sigma(pp \rightarrow b\bar{b}X)$ at $\sqrt{s} = 7\text{TeV}$ in the forward region*, Phys. Lett. **B694** (2010) 209, [arXiv:1009.2731](https://arxiv.org/abs/1009.2731).
- [23] LHCb collaboration, A. A. Alves Jr. *et al.*, *The LHCb detector at the LHC*, JINST **3** (2008) S08005.
- [24] <http://lhcb.physik.uzh.ch/ST/public/material/index.php>.
- [25] Particle Data Group, J. Beringer *et al.*, *Review of particle physics*, Phys. Rev. **D86** (2012) 010001.
- [26] J. Albrecht, *Fast Track Reconstruction for the High Level Trigger of the LHCb Experiment*, PhD thesis, Physikalisches Institut, Heidelberg, 2009.
- [27] M. Lieng, *An inclusive ϕ stream for the lhcb high level trigger*, CERN-LHCb-2009-010.
- [28] B. P. Roe *et al.*, *Boosted decision trees as an alternative to artificial neural networks for particle identification*, Nucl. Instrum. Meth. **A543** (2005) 577, [arXiv:physics/0408124](https://arxiv.org/abs/physics/0408124).
- [29] A. Höcker *et al.*, *TMVA - Toolkit for Multivariate Data Analysis with ROOT: Users guide*, Tech. Rep. CERN-OPEN-2007-007, CERN, Geneva, Mar, 2007.
- [30] R. E. Schapire, *The Strength of Weak Learnability*, Machine Learning **5** (1990) 197.

- [31] J. Therhaag, *TMVA Toolkit for multivariate data analysis in ROOT*, PoS **ICHEP2010** (2010) 510.
- [32] L. Breiman, J. H. Friedman, R. A. Olshen, and C. J. Stone, *Classification and regression trees*, Wadsworth international group, Belmont, California, USA, 1984.
- [33] V. Blobel and E. Lohrmann, *Statistische und numerische Methoden der Datenanalyse*, Teubner-Studienbücher : Physik, Vieweg+Teubner Verlag, 1998.
- [34] F. James and M. Roos, *Minuit - a system for function minimization and analysis of the parameter errors and correlations*, Computer Physics Communications **10** (1975), no. 6 343 .
- [35] T. Skwarnicki, *A study of the radiative cascade transitions between the Upsilon-prime and Upsilon resonances*, PhD thesis, Institute of Nuclear Physics, Krakow, 1986, DESY-F31-86-02.
- [36] LHCb collaboration, R. Aaij *et al.*, *Measurement of the fragmentation fraction ratio f_s/f_d and its dependence on B meson kinematics*, JHEP **04** (2013) 1, [arXiv:1301.5286](#).
- [37] LHCb collaboration, R. Aaij *et al.*, *Measurement of the polarization amplitudes and triple product asymmetries in the $B_s^0 \rightarrow \phi\phi$ decay*, Phys. Lett. **B713** (2012) 369, [arXiv:1204.2813](#).
- [38] LHCb collaboration, R. Aaij *et al.*, *Measurement of the effective $B_s^0 \rightarrow K^+K^-$ lifetime*, Phys. Lett. **B707** (2012) 349, [arXiv:1111.0521](#).
- [39] LHCb collaboration, R. Aaij *et al.*, *Effective lifetime measurements in the $B_s^0 \rightarrow K^+K^-$, $B^0 \rightarrow K^+\pi^-$ and $B_s^0 \rightarrow \pi^+K^-$ decays*, tech. rep., CERN, Geneva, Jun, 2014. Comments: 12 pages, 2 Figures.
- [40] LHCb collaboration, R. Aaij *et al.*, *Measurement of the \overline{B}_s^0 meson lifetime in $B_s^0 \rightarrow D_s^+\pi^-$ decays*, LHCb-PAPER-2014-037, in preparation.
- [41] M. Pivk and F. R. Le Diberder, *sPlot: a statistical tool to unfold data distributions*, Nucl. Instrum. Meth. **A555** (2005) 356, [arXiv:physics/0402083](#).
- [42] H. A. e. a. the ARGUS Collaboration, *Search for hadronic $b \rightarrow u$ decays*, Physics Letters B **241** (1990), no. 2 278 .
- [43] Jacobsson, Richard, *The lhcb upgrade*, EPJ Web of Conferences **60** (2013) 10004.

Erklärung:

Ich versichere, dass ich diese Arbeit selbstständig verfasst und keine anderen als die angegebenen Quellen und Hilfsmittel benutzt habe.

Heidelberg, den 10. September 2014